CrossMark

Smart NIR linear and nonlinear optical nanomaterials for cancer theranostics: Prospects in photomedicine

Tzu-Ming Liu [a,b,c,*], João Conde [d,e,*], Tomasz Lipiński [f,g], Artur Bednarkiewicz [g,h], Chih-Chia Huang [i,*]

[a] Faculty of Health Sciences, University of Macau, Macao
[b] Institute of Biomedical Engineering, National Taiwan University, Taiwan
[c] Molecular Imaging Center, National Taiwan University, Taiwan
[d] Massachusetts Institute of Technology, Institute for Medical Engineering and Science, Harvard-MIT Division for Health Sciences and Technology, Cambridge, MA, USA
[e] School of Engineering and Materials Science, Queen Mary University of London, London, UK
[f] Institute of Immunology and Experimental Therapy, PAS, Wrocław, Poland
[g] Wrocław Research Centre EIT+, Wrocław, Poland
[h] Institute of Low Temp & Structure Research, PAS, Wrocław, Poland
[i] Department of Photonics, Center for Micro/Nano Science and Technology, Advanced Optoelectronic Technology Center, National Cheng Kung University, Taiwan

ARTICLE INFO

ABSTRACT

Light-based diagnostics and therapy have become indispensable tools in the field of cancer nanomedicine. Various optical imaging modalities with tomographic capability have been developed to visualize cellular and organismic distributions of molecules. Microscopic pharmacokinetics and the tumor-targeting efficacy of nanoscale effectors can now be precisely evaluated. Moreover, phototherapy using intense laser light has been widely used for treating cancers. Using light-active nanoscale effectors, photothermal and photodynamic therapies on superficial tumors can be achieved with low-illumination lasers. Consequently, for the next generation of photo-medical techniques, the use of near infrared (NIR) excitation sources on NIR-activatable nanoparticles may offer deeper light penetration owing to less extensive scattering and absorption by endogenous chromophores in the NIR spectral region. Therefore, treatments and biodetection within higher tissue volumes and with less side effects (e.g. overheating) may be successfully implemented. This comprehensive review covers the state-of-the-art technologies on (a) advanced laser light sources appropriate for deep tissue theranostics, (b) types of laser interactions with pure-NIR and NIR-upconverting nanomaterials, (c) current development of NIR and multiphoton nanoparticles, (d) application fields of NIR nanomaterials in cancer theranostics, and (e) nanotoxicology of NIR nanoscale effectors for cancer treatment.

© 2017 Elsevier Ltd. All rights reserved.

* Corresponding authors at: Faculty of Health Sciences, University of Macau, Macao (T.-M. Liu). Massachusetts Institute of Technology, Institute for Medical Engineering and Science, Harvard-MIT Division for Health Sciences and Technology, Cambridge, MA, USA (J. Conde). Department of Photonics, National Cheng Kung University, Taiwan (C.-C. Huang).

E-mail addresses: tmliu@umac.mo (T.-M. Liu), jdconde@mit.edu, conde.bio@gmail.com (J. Conde), c2huang@mail.ncku.edu.tw, huang.chihchia@gmail.com (C.-C. Huang).

Contents

1. Introduction

With the advance of cancer biology, the scientific community is gradually obtaining a better understanding of the heterogeneity of tumors, the pathophysiology of their growth, and the establishment and seeding of metastasis. New strategies using targeting therapies have been developed for personalized and effective treatment of tumors [1,2]. In recent years, with advances in nanotechnology, nanoparticles have been considered as effective vehicles for targeted drug delivery. With appropriate designed [3] size, surface chemistry or coating polymers, and conjugated antibodies, these "nanomedicines" can be engineered to circulate longer in blood, passively overcome biological barriers, actively target cancer cells, and penetrate into tumor tissues with high specificity. After targeting, cancer tomographic visualization (single or combined luminescence/magnetic resonance imaging (MRI)/positron emission tomography (PET) contrast agents) can be employed as well, and the release and penetration of drugs into tumors can be further triggered by the tumor chemical microenvironment (e.g., lower pH in tumors) or photon activation (e.g., photodynamic effects) of nanomaterials [4,5]. Moreover, photon- or magnetic field-activated hyperthermia is of great interest for cancer theranostics [6–8]. Therefore, the application of nanomedicines has become one of the clinically important and promising fields in cancer diagnosis and therapy. The *National Cancer Institute* at the *National Institute of Health* have recognized this and thus documented that nanotechnology offers an amazing, paradigm-shift opportunity to make significant advances in cancer diagnostics and therapy [9–11].

To evaluate the targeting efficacy, pharmacokinetics, and pharmacodynamics of nanomedicines *in vivo*, nanomaterials are usually designed to provide contrasts in various modalities of molecular imaging [12,13], so that they can be visualized and their time-course dynamics can be tracked on different scales. The location of multiple tumors can be identified and the treatment response can thus be followed up. PET uses gamma photons emitted from tagged radioactive tracers to map

nano-agents [14]. This whole body imaging modality has the best sensitivity and precision for mapping the bio-distribution of nanomaterials. However, PET-based imaging does not yield information on the structure of tissues and organs. Besides, the centimeter-scale spatial resolution is not sufficient for satisfactorily resolving sizes and precise locations. To put tumor imaging in a meaningful context, PET is usually combined with X-ray computed tomography (CT) which provides millimeter-scale resolution. Metallic nanoparticles can be used to enhance the contrast in CT imaging [15–17]. Using MRI, the resolution can be further improved to 100 μm, which enables detecting earlier stage tumors. Nanomaterials with chelated metallic ions [18], Gd^{3+} doped nanoparticles or superparamagnetic iron oxides [19] can enhance the T1 and T2 contrasts in MRI. Different modalities of images can be registered and combined together by using the same contrast agents with multiple detection mechanisms. One such proof of concept example is hexamodal porphyrin-phospholipid (PoP)-coated upconversion nanoparticles (UCNPs), which demonstrate NIR fluorescence; can be used for up-conversion imaging, photoacoustic imaging, PET and Cherenkov luminescence imaging with ^{64}Cu isotopes; and provide possibilities of CT and MRI contrast [20].

For understanding the whole-body distribution and metabolism of nanomedicines, cellular level imaging is required to monitor their pharmacokinetics and pharmacodynamics in detail. Compared with other molecular imaging modalities, optical imaging has the unique advantages of sub-cellular spatial resolution, high temporal resolution, the ability to employ versatile labeling tools, and sensitive detection of molecules at low concentration levels. Researchers have used various optical microscopy techniques to resolve the vascular permeation, diffusion, docking, and cellular internalization of nanomedicines *in vivo*. Except for the targeting function, the temporal progression of treatment-induced changes in the tumor microenvironment, recruitment of immune cells, and removal of cancer cells can also be evaluated. Under this observation scheme, nanomaterials need to be optically contrasting for being able to visualize their dynamics and cellular responses. Interestingly, as the size of these nanomaterials decreases down to several nanometers, their unique physical properties can yield prominent optical contrasting in a variety of optical microscopy modalities. Examples of these are surface plasmon resonance (SPR) absorption in metal nanoparticles [21], quantum confined effects of exciton fluorescence in semiconducting quantum dots [22], conductor to fluorescent semiconductor transition in gold nanodots [23–26], defect fluorescence in nanodiamonds [27,28], long living and anti-Stokes efficient up-converting nanoparticles, and surface-state luminescence of iron oxides [29]. These sensitive optical contrasts can also depend on the chemical microenvironment to reflect the cell physiological conditions such as pH values [30] and oxygen partial pressure pO_2 [31–35]. Besides, strong SPR absorption of metal nanoparticles can effectively convert light energy into heat and reactive oxygen species through photo-thermal and photodynamic effects, respectively [36]. These photo-physical or photo-chemical functions of nanomaterials can be excited on demand to damage cellular membranes or to locally increase the oxidative stress. The release and spread of therapeutic agents can thus be controlled and intentionally promoted. As a result, except for the role of a drug carrier, nanomaterials themselves can both serve as contrast agents in diagnostic molecular imaging and therapeutic means in photo-medicines [37]. Such integrated function of nanomaterials, often termed theranostics [38], can be used to optimize the efficacy of therapy to address patient-specific characteristics of cancer.

To achieve these merits of photo-nanomedicine for deep tissue diagnosis and treatment, NIR excitation sources for NIR-to-NIR-activated nanomaterials are being actively studied; this technique allows excitation in the NIR spectral range where light absorption and scattering from biological tissues are minimized, as well as an increased light penetration combined with locally induced laser hyperthermia. Illuminated at the so-called "biological window" or "water window" (~700–950 nm, 1000–1300 nm, and ~1600–1850 nm, corresponding to the 1st, 2nd, and 3rd optical windows, respectively), the NIR light minimally interacts with physiological constituents (i.e., pigments, proteins, coenzymes, water) and thus negligently affects the wavefront propagation. Such synergy of laser engineering and material sciences has broadened the horizon for the *in vivo* exploration of cancer biology, enabling deep tissue treatment of tumors. To achieve this goal, in the last decade many research efforts have been devoted to obtain nanomaterials capable of absorbing in the NIR range, with numerous biological applications. Nevertheless, longer excitation wavelengths degrade the spatial resolution of *in vivo* imaging. Higher excitation intensity may reshape the nanoparticles and degrade the NIR response properties [39]. Besides, for several functional nanomaterials the efficient excitation bands are in the visible range only [21–28]. To expand the advantages of NIR excitation of nanomaterials, these challenges need to be overcome with new chemical designs and chemical architectures in combination with new excitation schemes and detection/treatment platforms.

With advances in nonlinear optics and introduction of new imaging methods, NIR light can now be used to excite various optical contrasts of nano-agents to probe biological specimen both functionally and structurally with increasing spatial and temporal resolution. The nonlinear optical contrasts can be generated at a least invasive wavelength and power level. Simultaneously, significant interest driven by the field of nano-toxicology has recently emerged to understand how biological specimens respond to nano-engineered materials of various size and composition and with different surface properties. Besides, the visible absorption band of most functional nanomaterials becomes NIR-excitable through multiphoton processes allowing *in vitro* and *in vivo* multifunctional imaging and combined therapy using noble and magnetic nanoparticles [29,40]. The multiphoton yield of NIR excitation can be enhanced through the structural plasmon resonance [40] or surface modification [29]. Different NIR contrast mechanisms can thus be realized on single-type nanomaterials (e.g., gold, quantum dots, Fe_3O_4, polymers, carbon-based nanoparticles) to produce multiphoton emission, photoacoustic responses, and local hyperthermia. For example, NIR absorption and fluorescence were recently demonstrated for Fe_3O_4 nanoparticles [29], making these a versatile platform for photo-thermal therapy and two-photon fluorescent bio-imaging. The development of fluorescent Fe_3O_4 nanoparticles enables whole-scale cancer theranostics, combining optical microscopy with well-established MRI. Therefore, understanding the current development of these NIR-active nanoparticles combined with laser systems will
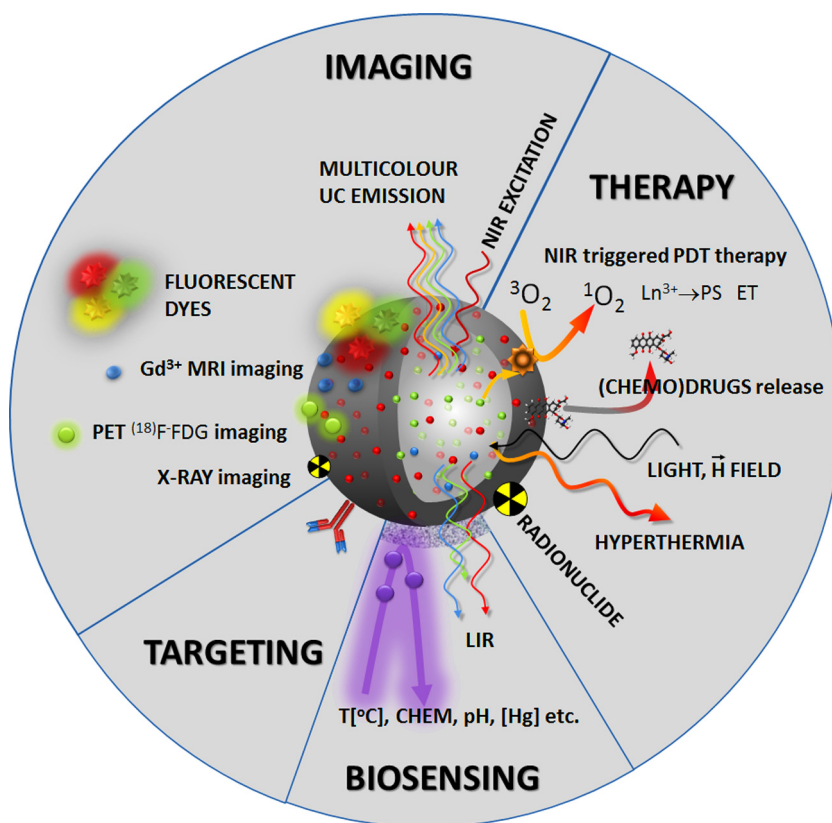
Fig. 1. Overview of NIR nanomaterials' applications for IMAGING- as contrast agents for X-ray, PET, MRI, fluorescence, multicolor visible-to-NIR luminescence, THERAPY by NIR-activated PDT therapy, chemo(drugs) release, hyperthermia combined with radionucleotide action, BIOSENSING, where different factors (temperature, chemicals, pH, metal ions) modulate the lifetime and intensity ratio of luminescence, and TARGETING on desired tissue sites.

inspire researchers to exploit "linear and nonlinear optical nanomaterials" beyond the conventional lanthanide-based up-converting nanoparticles.

Indeed, development of NIR photo-functional nanoparticles has promised new strategies to visualize tumor microenvironments *in vivo* as well as the improvement of a remote triggering of photodynamic or photo-thermal therapy and photo-induced chemical bond dissociation. For *in vivo* pre-clinical studies, these NIR multiphoton contrast agents provide a better anatomical resolution and detection sensitivity than conventional clinical MRI or X-ray CT.

Consequently, the core focus of this review article is to provide a concise overview of newly developed NIR-to-NIR nanomaterials and their potential applications in cancer targeting and deep-tissue imaging. This review goes well beyond the state-of-the-art technologies, by unifying the latest advances in designing smart NIR-to-NIR multiphoton nanotechnology for cancer theranostics. These newly developed multifunctional NIR-to-NIR nanomaterials and unique optical imaging methods will certainly enhance the capabilities of tumor targeted imaging and hold promise in cancer diagnostics and therapeutics, tackling crucial biomedical questions (Fig. 1).

2. Contrast mechanisms of NIR nanomaterials

Depending on the light-matter interaction pathways, the contrast characteristics of NIR optical imaging may arise from linear or nonlinear optical processes. Linear optical processes include absorption, scattering, interference, fluorescence, phosphorescence, and Raman scattering (Fig. 2). Absorbed light may be further converted into heat or ballistic acoustic waves.

Nonlinear optical processes are important contrast mechanisms for realizing NIR imaging. These processes are excited/activated by intense laser pulses and include multiphoton absorption and fluorescence, second harmonic generation (SHG), third harmonic generation (THG), coherent anti-Stokes Raman scattering (CARS), stimulated Raman scattering (SRS), and multiphoton up-conversion luminescence (Fig. 3). These contrasts either can yield morphological information or report the molecular distribution to reveal the cancer biology and pharmacokinetics of nanomedicines *in vivo*. Different contrasts have their own *pros* and *cons* in different contexts. In the following sections, we will introduce the major types of linear and nonlinear optical contrasts of nanomaterials, and their corresponding imaging modalities.
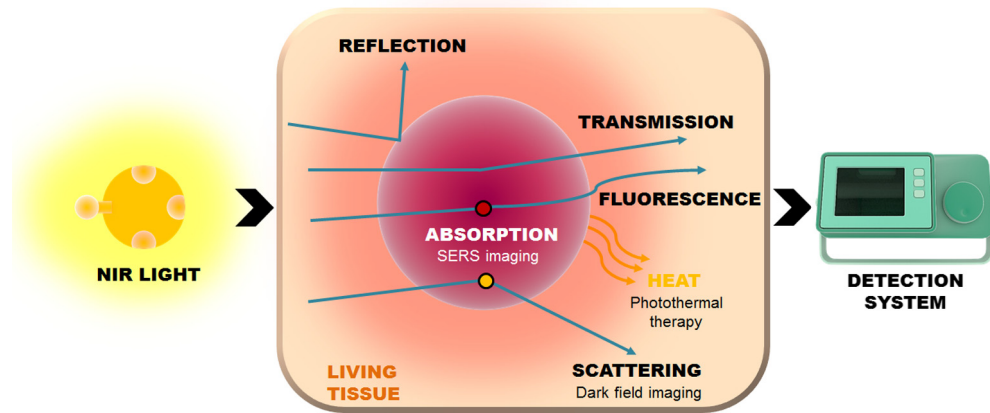
Fig. 2. Types of single-photon contrast mechanisms.
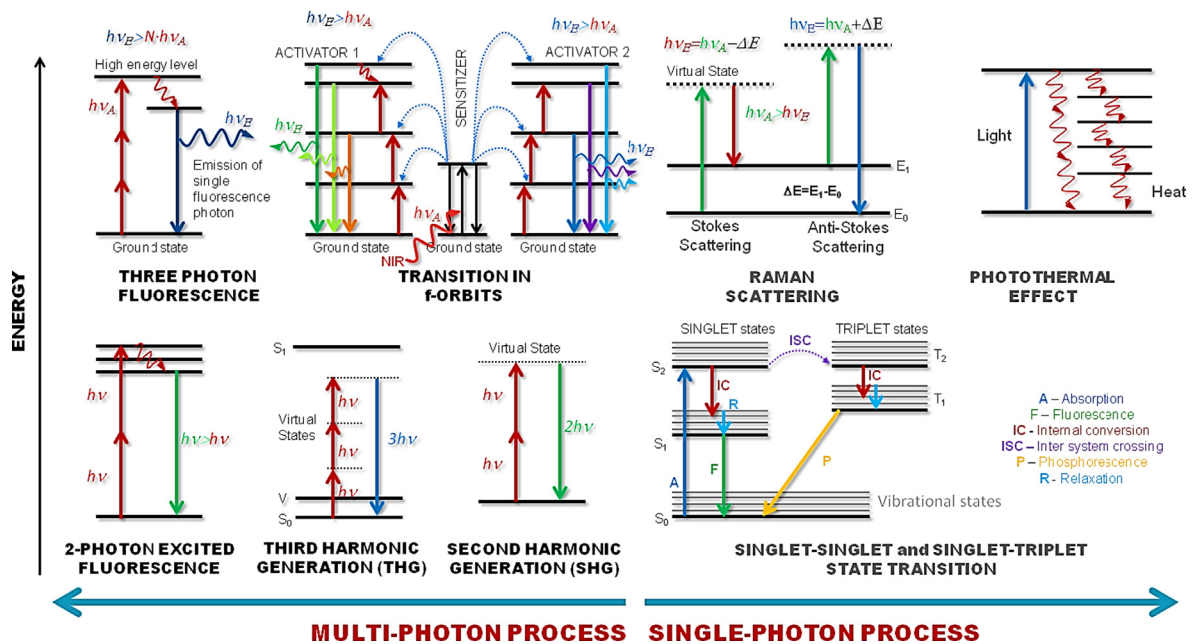
Fig. 3. Schematic of the energy diagram of the absorption and emission features of nanomaterials based on the single-photon and multiphoton transitions.

2.1. Single-photon transition for fluorescence contrast agents

Fluorescence processes involve only transitions of electrons within molecules, and their excitation and emission bands are determined by molecular composition and structures. They can be single-photon excited at low intensities (Fig. 2). Light excitation of the absorption band of fluorophores results in the excitation of ground-state electrons. Through a fast (∼300 fs) internal conversion or vibrational relaxation [41], thermalized electrons accumulate in *quasi*-steady states and then relax back to their ground states by releasing photons. Typically, this fluorescence relaxation process occurs on the nanosecond (singlet-singlet fluorescence) or micro to millisecond (triplet-singlet phosphorescence) scale. The red-shift of the emission wavelength allows the suppression of excitation photons with filters and the enhancement of detection sensitivity with photomultiplier tubes. Therefore, among all optical contrast processes, fluorescence is the most sensitive and specific one (Fig. 3) for biomedical imaging. To achieve NIR fluorescence in nanomaterials, a straightforward strategy is to cross-link or anchor NIR dyes such as cyanine molecules with or to the surface of nanoparticles. To reduce the complexity of synthesis and to avoid the concern of extra toxicity, inherent fluorescent contrast characteristics of nanoparticles may be exploited. For crystalized nanoparticles, direct-bandgap NIR fluorescence of semiconductor quantum dots (e.g., CdSe [22], Ag_2S [42], $CuInS_2$ [43]) or carbon nanotubes [44–46] has been developed. Exploiting type-II band-alignment between core-shell semiconduc-

tors, NIR fluorescence can be further tuned to longer wavelengths [47]. For indirect bandgap materials such as silicon, their nanometer sizes increase the momentum uncertainties of electrons and assists in the indirect relaxation of electrons. Silicon nanocrystals exploit these properties to obtain more efficient NIR fluorescence [48,49]. Most of other luminescent nanomaterials rely on defect states or localized states to yield less efficient and relatively broad NIR emission bands. This luminescence becomes prominent for nanomaterials with large surface-to-volume ratio, such as carbon nanodots [50–54], nanodiamonds [27,28], and gold clusters [55]. Using these fluorescence labels, injected nanomedicines can be visualized and tracked using a bright-field fluorescence imaging system. Nanomaterials may be illuminated at a specific excitation wavelength and the diffused fluorescent photons collected and form a whole body image on a sensitive charge-coupled device (CCD) camera. Such an *in vivo* imaging system can be used for evaluating the whole body circulation and the targeting of nanomedicines. Just like a conventional camera system, the angular resolution of this imaging modality is typically determined by the emission color of labels, the aperture of cameras, and the pixel densities of CCD CMOS chips.

To take a closer look at microscopic scales *in vivo*, the use of laser scanned confocal microscopy techniques is required. At each excitation point, the out-of-focus fluorescence will be rejected by a confocal pinhole before photomultiplier tubes and the tomographic distribution of nanomedicines *in vivo* can be revealed in a three-dimensional (3D) image stack with submicron resolution. In this case, the imaging depth will be limited by the scattering properties of tissues, and is typically 100–150 μm for turbid tissues such as skin.

In addition to the fluorescence intensity, the fluorescence lifetime is another contrast mechanism of fluorescence that is often highly sensitive to the molecular microenvironment. Related imaging modalities include fluorescence resonant energy transfer (FRET) microscopy, fluorescence lifetime imaging microscopy (FLIM), and time-gated fluorescence microscopy. The FRET and FLIM modalities can be used to evaluate microscopic drug release from theranostic nanoparticles. Before drug release, FRET events occur between the donor (nanoparticles) and acceptor (fluorescent drug). After release, the acceptor diffuses away and only the donor fluorescence can be detected. This evaluation scheme has been realized for quantum dots [56,57], polymer-based micelles [58], and mesoporous silica nanoparticles [59]. Differences in the fluorescence lifetimes across molecules can be used to differentiate the targeted molecules from other molecules [60,61] (e.g., bound and unbound reduced nicotinamide adenine dinucleotide (NADH) fluorescence) or from a non-specific background [62]. For instance, the auto-fluorescence lifetime of endogenous chromophores is typically ~1 ns. By employing nanomaterials with fluorescence lifetimes on the order of several tens of nanoseconds (e.g., quantum dots (QDs) and nanodiamonds) or luminescence lifetimes on the order of micro- to milliseconds (lanthanide doped nanoparticles), and by performing time-delayed and gated integration of photons after the excitation pulse, it is possible to realize a background-free and thus possibly ultrasensitive detection and fluorescence imaging of nanomaterials. This concept has been recently applied to fluorescent diamond nanoparticles for tracking diamond labeled cells in an environment with large auto-fluorescence [62].

2.2. Single photon phosphorescence

For some photosensitizing molecules, such as porphyrins, photo-excited electrons can couple to triplet states through intersystem crossing. Photon emission of phosphorescence occurs when triplet-state electrons relax back to singlet ground states, whose wavelengths typically range from red to NIR (Fig. 3). In contrast to fluorescence, this forbidden transition process of electrons results in a microsecond to millisecond lifetime after excitation. The lifetime is so long that phosphorescence could be quenched by collisions of triplet oxygens in water. This quenching is typically responsible for dimming the phosphorescence intensity and shortening the phosphorescence lifetime. Exploiting this property, the pO_2 levels in vasculature and tissue can be quantitatively evaluated based on changes in the phosphorescence intensities or lifetimes. However, these photosensitizers are toxic to cells and not stable in biological environment. Nanomaterials, in this case, can host these phosphorescent dyes and make them useful probes for measuring the level of pO_2 [31–35]. Researchers have used such phosphorescence probes to study pO_2 in the eye retinae [63], in the cerebral vasculature and tissue [64], and in the niche of hematopoietic stem cells [65]. Microscopic pO_2 imaging can be performed with three-dimensional (3D) sub-micron resolution, which is useful for investigating hypoxic microenvironments in wound healing, tumor growth, and stem cell niches.

2.3. Single photon Raman scattering

Different from elastic scattering (Fig. 2), in the Raman scattering process, the incident light (photons) interacts with the vibrations (phonons) of the target molecules and the scattered photons may have lower (the Stokes line) or higher (the anti-Stokes line) energy. Each molecule, owing to its characteristic bonding structure and vibrational modes, has its own spontaneous Raman spectrum. Depending on the size of molecules and the strength of bonds, the vibration frequency of interest can range from very low (5 cm^{-1}) to 4000 cm^{-1}. Strong Raman peaks can serve as contrasts for microscopic molecular imaging. For biological samples, NIR-excited Raman spectra can reduce the interference from auto-fluorescence. However, the Raman scattering intensity is proportional to $1/\lambda^4$, which means that the signal is weakened by an order of magnitude for wavelengths in the NIR range. Therefore, there is a trade-off on selecting a proper wavelength for excitations associated with Raman scattering.

2.4. Photoacoustic contrast

Traditionally, staining dyes have been used in bright-field microscopy for absorption contrast of cells. Cells with intrinsic pigments, such as red blood cells, can be easily observed *in vivo* without any staining [66]. Using photoacoustic imaging, the light absorption characteristics of materials can be exploited to convert light energy into acoustic waves for background-free and deep-tissue tomography. The main advantage of the photoacoustic contrast method is its flexibility: it can either use optical excitation or acoustic detection as the aperture function for determining the imaging resolution [67]. In the ballistic excitation regime, where the imaging depth is smaller than the inverse of the photon scattering constant, a focused Gaussian beam can still maintain a point spread function (PSF) of sufficient quality for the microscopic scale. Beyond the ballistic regime, the optical wavefront gradually loses its coherence and the PSF can easily increase beyond 100 μm. In this case, less divergent acoustic waves have better resolution using phase-array detection. This flexibility of photo-acoustic imaging extends the microscopic scale imaging to a depth much deeper than what can be achieved using optical coherence tomography (OCT). A widely exploited photo-acoustic contrast is the absorption of hemoglobin in red blood cells. Fine blood vasculature can be mapped in a larger field of view at a deeper imaging depth [67]. A functional photoacoustic microscope was developed, which provides multi-wavelength imaging of optical absorption and allows high spatial resolution beyond this depth limit with a ratio of maximal imaging depth to depth resolution greater than 100. This capability is useful for studying angiogenesis in tumor microenvironments.

Among many nanomaterial systems, noble metal nanoparticles are ideal NIR photoacoustic contrast agents for *in vivo* nanoscale molecular imaging. Recently, Bao et al. reported the use of gold nanoprisms as novel contrast agents for the hybrid technique of optoacoustic imaging in mice gastrointestinal tumors [68,69]. They have demonstrated a huge absorption cross-section of such nanoparticles owing to their free electrons. The SPR effect plays a major role in increasing the absorption cross-section and manipulating peak absorption wavelengths.

2.5. Surface plasmon resonance effect

Surface plasmons are dipolar excitations related to the density waves of free electrons in metals. For isolated nanoparticles, surface plasmon modes are standing waves with zero momentum and can thus easily interact with photons [21,70]. According to *Mie* theory, this dipolar absorption makes the dielectric constants of a metal negative in a certain range of wavelengths, which can locally enhance the electric field on a spatial scale much smaller than that of the excitation wavelength [71]. Typically, for spherical solid metal nanoparticles, the SPR wavelengths are in the visible range. To achieve SPR in the NIR wavelength range, the geometry of metal nanoparticles needs to be tailored into nanorods, nano-shells, or triangular nanoplates. Another strategy is to employ materials with lower free-carrier densities, such as conducting metal oxides or doped semiconducting nanocrystals [72]. This SPR-enhanced electric field can significantly increase the yield of originally weak signals such as those in Raman scattering [73], harmonic generation [40,74–76], and multiphoton fluorescence [40]. This signal enhancement feature of SPR can be employed for detecting trace amounts of molecules. The SPR effects can also enhance the Raman scattering in nanomaterials, especially for the enhancement of NIR excited ones. For example, using micro-Raman spectroscopy, the detection of individual molecular vibration signals became possible once the surface-enhanced Raman scattering (SERS) (Fig. 2) was involved after combining long-range electromagnetic and short-range chemical enhancements [73,77]. Currently, molecular tags on Au nanomaterials have become a powerful tool for developing successful *in vivo* disease site tracking methods [78], sensing the intracellular pH environment [79], and screening circulating tumor cells [80] by using NIR lasers.

2.6. Quantum confinement effects

In quantum mechanics, the particle-in-a-box model explains how free particles can occupy certain positive energy levels when they are confined to a low-dimensional potential well. In a nanometer-scale semiconductor quantum well, there are quantized eigenstates of electron wave functions in the conduction and valence bands. For narrower well widths, the transition bandgap is larger, yielding a fluorescence blue-shift. For low-dimensional nanomaterials, 3D confinement of electron or exciton wave functions yields similar effects. For instance, smaller sizes of CdSe semiconductor quantum dots have shorter exciton absorption peaks and emission wavelengths [81], which can be tuned from blue (~480 nm) to red (~650 nm). This color tunability can be used for multiplexed optical coding of biomolecules [82]. For indirect-bandgap silicon nanocrystals, this confinement will also increase the transition gaps of free excitons and localized states [83]. The tuning range is wider from 400 nm to the NIR 750 nm wavelength. Another type of quantum confinement is defect-related localized states. Depending on the domain environment and size, different transition sites may have different excitation and emission peaks. Fluorescent carbon nanodots have this feature, and the emission wavelength can be tuned via excitation ranging from 400 nm to the 700-nm wavelength of NIR [50–54].

2.7. Rare-earth dopant based single photon up-converting process

Up-conversion of photons is a sequential absorption of two or more photons (typically NIR photons) by materials that leads to the emission of light at a shorter wavelength than the excitation one (the so-called anti-Stokes emission) [84]. This

phenomenon usually occurs in solid-state materials doped with d-block and f-block elements. The interaction between doping ions and lattices forms ladder-like arrangement of energy levels with similar spacing, and allows sequential excitation of electrons to an even higher excited state. The up-conversion processes can roughly be divided into three categories: excited state absorption (ESA), energy transfer up-conversion (ETU), and photo avalanche (PA). For example, Yb^{3+} sensitized Er^{3+} or Tm^{3+} systems are usually co-doped in $NaYF_4$ and yield an efficient ETU [85]. The Yb^{3+} sensitized Ho^{3+} co-doped oxyfluoride glass ceramics yield a serial ESA and PA up-conversion [86]. These nonlinear optical processes should be distinguished from coherent up-conversion processes such as multi-photon absorption and harmonic generation. The major difference is that the photon up-conversion can be realized at low excitation intensities, while the coherent up-conversion cannot, which is owing to the engagement of real or virtual energy levels, respectively. For biomedical imaging, this unique optical contrasting mechanism has been used in rare-earth ion doped nanoparticles [85,87]. Multicolor and narrowband absorption/emission are achieved as well as color tunability [88] at the synthesis stage, perfect photo-stability of luminescence and both NIR-to-vis and NIR-to-NIR emission can be obtained with these materials. However, for nanomaterials with a high surface-to-volume ratio, the excited electron clouds may easily couple with surface states and severely quench the up-conversion process. In this situation, an undoped shell coating on the up-converting core is required to keep the excited electrons away from fast multiphotons and non-radiative quenching by the surface ligands and water molecules [87].

Compared with organic dyes and quantum dots, up-conversion luminescence of rare-earth doped nanoparticles allows the up-conversion processes based on Yb^{3+} sensitized Er^{3+} or Tm^{3+} systems [85]. Owing to the common excitation at 980 nm, a $NaYF_4$ host combined with $Yb^{3+}/Er^{3+}/Tm^{3+}$ guests permits deep-tissue excitation and avoids the excitation of auto-fluorescence owing to the tissue background, which is a severe drawback of most *in vitro* or *in vivo* optical Stokes ($\lambda_{exc} < \lambda_{emi}$) microscopy systems. However, the up-conversion process decays in typically several tens of microseconds to a millisecond [89], which sets a lower limit on the pixel dwell time and thus slows down the imaging speed of laser-scanned confocal microscopy. For example, for a 512×512 pixels image, a pixel dwell time of 10 μs will result in the frame time of 2.62 s, which is too slow for imaging some kinetic phenomena and characteristic of biological systems. Therefore, in most cases, up-conversion contrast labels are applied to whole body wide field imaging and bright-field fluorescence microscopy [90].

2.8. Multiphoton nonlinear optical processes

According to the electromagnetism theory, the polarization density P of a material can be induced by light illumination. For low-intensity illuminations, the amplitude of P is linear in the applied electric field E. With the invention of ultrafast lasers, coherent light energy can be instantaneously delivered using picosecond (10^{-12} s) or femtosecond (10^{-15} s) pulses; as a result, the instantaneous intensity can reach unprecedented levels of 10^{12} W/cm^2 even for low power. Such strong coherent electric fields can drive electrons in materials away from atomic harmonic potentials, and anharmonic vibrations induce nonlinear polarization in materials. From the viewpoint of light-matter interaction, this nonlinear polarization involves multiphoton processes in which new photons with shorter wavelengths are generated. Because the signal yield depends nonlinearly on the intensity of light excitation, detectable nonlinear optical signals can only be generated within the confocal range around the focus. This feature of nonlinear optical signals defines a sectioning plane of images. Therefore, without using confocal pinholes, these modalities have intrinsic capability of sectioning microscopy *in vivo*. Besides, the effective PSF will be improved by $1/\sqrt{N}$, where N is the order of nonlinearity [91].

The SHG is an energy-conserved coherent generation of photons with doubled light frequency. The generation of nonlinear polarization does not require real electronic states. Therefore, NIR femtosecond lasers can generate SHG without any limitation on the excitation wavelength. Nonlinear polarization occurs in materials with non-central symmetry. Typically, homogeneous tissues or cells would not generate SHG signals. These signals can be generated by structured proteins such as collagens and muscles [92–96], spindle fibers [92–95], micro-tubulins [92–95], fibrous astroglial filaments around axons [97–99] and *zona pellucida* of mammalian oocytes [100]. The strong SHG of collagen has been used in optical virtual skin biopsy [101,102], in the context of dermatitis [103], aging [104], and tumor diagnosis [105]. Since most nanoparticles have a non-central symmetric crystal structure, they more or less carry permanent dipoles that can assist in the generation of SHG. Even for central symmetric metal nanoparticles, quadrupolar SHG can still be generated at the surface where symmetry breaks [106]. As the surface-to-volume ratio increases, non-symmetric shapes may also induce dipolar SHG [107]. Exploiting the SPR effects or resonance enhancement effects, weak SHG in nanoparticles can further be enhanced [40]. These SHG nanoprobes can be used as non-bleachable and non-blinking contrast agents for long-term cell tracking [108,109].

The frequency tripled THG process does not have symmetry restrictions. However, owing to the *Gouy* phase shift of focused Gaussian beams, the generation of THG before focusing will be cancelled by the one that is generated after focusing. This implies that homogeneous samples cannot generate THG. THG generation only occurs at interfaces between media with significantly different refractive indices [110] or on nanoparticles with sizes much smaller than the focal volume [74,75]. Similar to the differential interference contrast microscopy, the THG contrast can yield the *in vivo* morphology with a 3D submicron resolution. This contrast has been used for imaging cellular membranes, lipids [111,112], elastic fibers [113], hemoglobin [114], melanin [105], and granules in leukocytes [115,116]. To obtain strong THG signals in the visible wavelength (390–700 nm), where the microscope is designed to have high transmission, the excitation source must be an NIR laser with the wavelength longer than 1170 nm [117]. This will require special gain media and design of laser sources. For nanoparticles, the THG intensity will be proportional to their volumes [118,119]. Higher refractive index contrasts, such

as Si nanowires [120], would result in a larger THG yield. Similar to SHG, the yield of THG can also be enhanced by SPR effects [40,74–76].

Different from harmonic generation microscopy, Raman scattering-based CARS and SRS microscopy achieve contrast through molecular vibrations and thus, have more molecular specificity. In CARS microscopy, two photons from a picosecond pump (∼850 nm) and one from the Stokes field (1.12–1.17 μm) in the infrared range can coherently generate the anti-Stokes field in the red region (650–700 nm) [121,122]. This three-photon process involves a third-order nonlinear optical effect. To remove the non-resonant background associated with four-wave mixing and to improve the spectral resolution, SRS microscopy was developed [123]. Originally, only the C-H stretching mode and water were considered to exhibit sufficiently strong CARS or SRS responses for quick imaging frame rates. At present, video-rate SRS microscopy has been realized by improving the collection efficiency [124]. The commonly employed vibration modes of nanoparticles in CARS or SRS microscopy are the C-H stretching modes of polystyrene beads [121,122]. Other vibrational modes and corresponding contrast agents include the G mode vibration of carbon-nanotubes [125] and the C-C sp3 vibration of nanodiamonds [126]. These CARS contrasts of nanoparticles allow label-free long-term cell tracking for *in vitro* or *in vivo* studies [127].

Among all nonlinear optical contrasts, multiphoton fluorescence is based on intra-molecular electronic transitions and has the best molecular specificity. The CARS or SRS contrasts may yield information on molecular vibrations, but many vibration modes are commonly shared by different proteins or lipids. The theory of two photon fluorescence (TPF) was first proposed by *Maria Göppert-Mayer* in 1931. After the invention of femtosecond lasers, the laser scanned TPF microscopy was realized by Webb's group in 1990 [128]. In the TPF process, the electrons can be excited with photon energy slightly above half of the bandgap. Visible fluorescence can thus be instantaneously generated with infrared light sources. Just like SHG and THG microscopies, the TPF microscopy has depth discrimination owing to the nonlinear dependence of yields on the excitation intensity. Compared with single-photon fluorescence microscopy, this fluorescence excitation scheme has the benefit of reduced out-of-focus photo-bleaching on dyes, deep tissue NIR excitation, resolution improvement through nonlinear optical processes, and selective excitation of the dyes of interest. With the invention of genetic labeling with fluorescence proteins, TPF microscopy has become widely used in longitudinal studies in molecular cell biology *in vivo* [129]. The TPF efficiency of molecules or nanomaterials is evaluated by the two-photon action cross-section, which is the product of fluorescent quantum yield φ_F and the absolute two photon absorption cross-section σ_{2p} (GM). The TPF action cross-sections of endogenous fluorophores such as NADH are fairly low (<10^{-4} GM) [129]. Most commonly used dyes and fluorescence proteins have 1–300 GM action cross-sections [129]. Using CdSe-ZnS quantum dots, this action cross-section can be increased to 50,000 GM [129], which allows a lower excitation dosage of light or greater imaging depth.

3. Choice of light source and wavelength for NIR deep tissue theranostics

Considering *in vivo* deep tissue imaging, visible light excitation has poor PSF performance owing to severe Rayleigh and Mie scattering from pigments and randomly oriented collagen networks. The absorption of melanin and hemoglobin (Hb) by the vasculature can further attenuate the contrasts in the 400–800 nm range of wavelengths, and strong excitation may induce photo-thermal damage. Two-photon excitation at wavelengths around or below 800 nm can also excite endogenous photosensitizers, such as porphyrins, and can generate reactive oxygen species (ROS) [130]. On the other hand, for wavelengths longer than 1300 nm, water absorption becomes the major limiting factor. High illumination intensity for deep-tissue imaging also induces photo-thermal damage. Therefore, for most biological tissues, the penetration window for optical imaging is 800–1300 nm (Fig. 4A) [131,132]. The range of 1000–1300 nm would yield a better performance of imaging depth and less photo-damage associated with measurements. For tissues with weaker presence of pigments and collagen (e.g., brains), wavelengths in the 1600–1850 nm range can also be considered [133].

Considering the 1000–1300 nm penetration window of biological tissues, lanthanide ion doped up-conversion nanomaterials have become popular for use in NIR deep-tissue theranostics. The optical properties of lanthanide ions have been known for many years, and lanthanide doped crystals, glasses, and fibers have been used as optically active materials for compact solid state laser crystals [134–136], fiber lasers [137], TV/lamp phosphors [138], and IR quantum cutters [139]. The interest in lanthanide up-conversion has resulted in new discoveries, i.e., many up-conversion mechanisms have been discovered in lanthanide ions, such as ESA, co-operative energy transfer (CET), PA, or most ETU [140]. These discoveries opened up a new field for applications in volumetric displays [141], remote temperature fiber sensors [142], and up-conversion lasers [143]. Recently, owing to chemical engineering of active-core-active-shell nanoparticles, novel routes of ETU have been designed such as energy migration mediated energy up-conversion [144–146], which are of special importance for biomedical applications.

There are three types of transitions in lanthanides (Fig. 4B), which are of some importance for biomedical applications:

(i) **Stokes visible emission under ultraviolet (UV) excitation** (typically <400 nm excitation for Eu^{3+} (∼630 nm), Tb^{3+} (540 nm), Sm^{3+} (650 nm), and Dy^{3+} (570 nm) complexes). The complexes of Eu^{3+} and Tb^{3+} ions have been often used in bioassays or for bio-imaging, but require short-wavelength excitation. The spectral overlap of excitation bands or emission bands of these compounds with respective absorption or emission of endogenous chromophores decreases the sensitivity of bioassays or decreases the contrast of *in vivo* imaging. However, owing to the very long luminescence lifetimes of Tb^{3+} and Eu^{3+} (millisecond scale), time-gated techniques are efficient in removing background signals as well as for studying biochemical processes using the FRET technique [147].
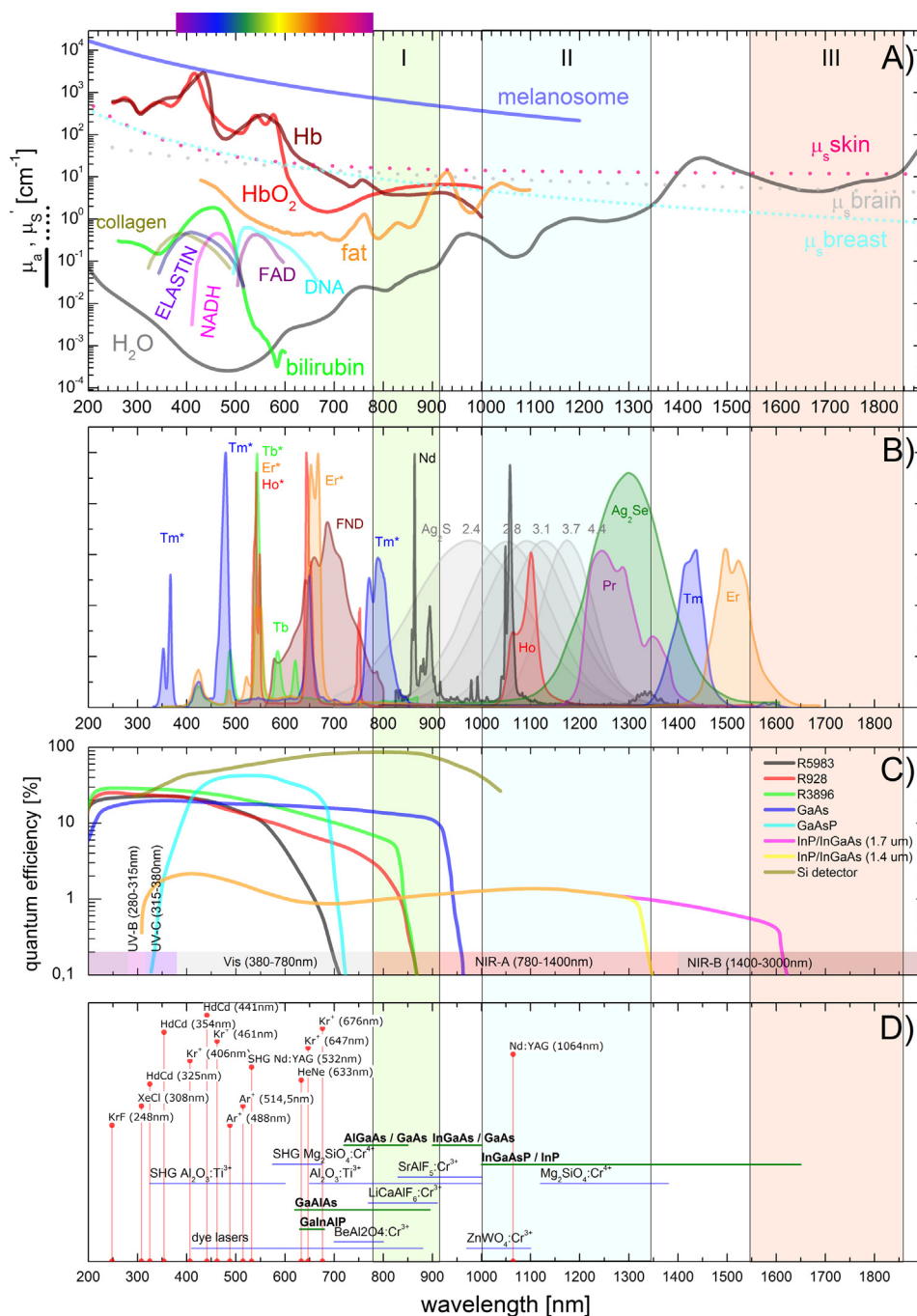
Fig. 4. (A) Absorption (μa) and reduced scattering (μs') coefficients of major tissue components and representative tissues, Fluorescence spectra of major tissue components [NADH, DNA, elastin, collagen, flavin adenine dinucleotide (FAD)] combined with representative fluorescence spectra of commercial quantum dots and organic fluorophores, and reduced scattering coefficient of skin, brain and breast tissues (B), (stokes and anti-Stokes) luminescence spectra of lanthanide doped nanoparticles (C), sensitivity of available photo-detectors (D) and available discreet (horizontal red lines) and tunable (vertical lines indicate tuning range) state-of-the-art lasers. R5983, R928, and R3896 are part numbers of the Hamamatsu photomultiplier tubes.

(ii) **Stokes emission in NIR (λ > 1 μm).** Most lanthanides demonstrate Stokes emission with obviously higher quantum efficiency than the up-conversion processes. Some of these ions can generate emission in the NIR I or NIR II optical windows. The most prominent rare-earth ions for *in vivo* NIR imaging are Nd^{3+} (emission at 860 nm, 1060 nm, and 1330 nm), Er^{3+} (emission at 1530 nm) or Ho^{3+} (emission at 1450 nm) [148]. Most of the existing studies concentrated on LaF_3 [149,150], NdF_3 [151], and Y_2O_3:Yb/Er [152], but the most promising material is $NaYF_4$, e.g., $NaGdF_4$:Nd^{3+}@

NaGdF$_4$ and NaYF$_4$:Yb/Er/Ho/Tm/Pr@NaYF$_4$ core-shell down-converting nanoparticles [153,154]. Unlike LaF$_3$, fluorides of the NaYF$_4$ type are synthesized in a more predictable manner, i.e., the synthesis protocols, mono-distribution of size, bio-functionalization protocols, and ability to make core-shell designs are much better controlled and reproducible.

(iii) **Anti-Stokes (up-conversion) emission under NIR photoexcitation** – typically 980 nm excitation for Yb^{3+} sensitizers or 808 nm photoexcitation for Nd^{3+} sensitizers is used to achieve visible and multicolor emission from activators such as Tm^{3+}, Er^{3+}, Ho^{3+}, and Tb^{3+}. No organic chromophores absorb at 980 nm (absorption of Yb sensitizers) or 800 nm (absorption of Nd^{3+} sensitizers); thus, the signal to noise ratio is usually very high. Only water molecules exhibit an absorption band at ∼980 nm, which under high photoexcitation densities may induce local overheating. These effects can be however diminished by using Nd^{3+} primary sensitizers, whose absorption cross-section at 800 nm is ∼5 times higher than that of Yb^{3+} at 980 nm; in contrast, the absorption coefficient of water at 800 nm is ∼20 times lower than that at 980 nm [145]. Recently, new possibilities have been discovered by nano-engineering the host materials and by developing core-multi-shell formations with independent doping of individual shells. These advances have opened new possibilities in terms of increased light penetration depth, limited local overheating, and multicolor emission capability [155].

However, most fluorescence dyes may not be single-photon excited at these wavelengths (Fig. 4B). They need to be two-photon or three-photon [133] excited. Consequently, to realize deep-tissue molecular imaging, it is necessary to have ultra-fast NIR excitation sources and nanomaterials suitable for generating contrast in the NIR range. Commonly used femtosecond/picosecond Ti:sapphire lasers have bandwidths of 10 nm/1 nm at 800 nm and transform-limited pulse-widths of 94 fs/0.9 ps. Their operation wavelength is tunable in the NIR range (700–1000 nm) for the two-photon excitation of most blue, green, and yellow fluorescence or phosphorescence dyes. The advantages of two-photon excitation in the NIR range is reduced out-of-focus photo-degradation of fluorescent dyes during 3D-sectioned imaging. They also serve as pump waves in CARS and SRS microscopy. Their application to different optical contrasts has been widely reported elsewhere. To excite red fluorescence or realize deeper imaging depths, 1000–1300 nm ultrafast light sources would be highly desired. Some researchers use Ti:sapphire lasers to pump an optical parametric oscillator (OPO) to obtain a tunable 1050–1300 nm femtosecond source. Nevertheless, such a setup is usually expensive and the maintenance of this system is complex and time consuming. In this section, we will review new advances in the 1000–1300 nm NIR laser sources for *in vivo* deep tissue imaging.

3.1. Nd:YAG and Nd:YVO$_4$ lasers

The neodymium-doped yttrium aluminum garnet (Nd:YAG) laser is a four-level laser system operating at ∼1064 nm using Nd^{3+} ions as gain centers. The upper state fluorescence lifetime is long (∼230 μs) [156], so that a significant population inversion can be maintained with a relatively low pump power. Therefore, it is usually operated as a Q-switched laser generating nanosecond pulses with a pulse energy on the order of tens of millijoules. Such a high pulse energy has been employed for deep tissue NIR photoacoustic imaging [157]. With the help of OPO, the wavelength of a Nd:YAG laser can be tuned to 1210 nm and 1700 nm for CH$_2$ and CH$_3$ bond-selective photoacoustic imaging, respectively [158]. With Nd^{3+} ions doped into yttrium vanadate (YVO$_4$), the gain bandwidth increases to 1 nm, which allows the generation of 2-ps-long laser pulses [159]. Laser sources of this type can be used for generating Stokes waves in CARS microscopy. The 532 nm SHG output of this laser can synchronously pump another OPO to generate tunable pump waves [160]. For CARS microscopy applications, picosecond lasers should have sufficiently strong nonlinearity for generating anti-Stokes signals. Femtosecond lasers will increase the non-resonant background of four-wave mixing and reduce the CARS contrast.

3.2. Cr:forsterite lasers

Pumped by 1064 nm Nd:YVO$_4$ or Yb:fiber lasers, the ultrafast Cr:forsterite laser can produce 1250 nm femtosecond-duration pulses for minimally invasive SHG, THG, and TPF microscopy [92–95]. Compared with Ti:sapphire lasers, the operation wavelength is far from the two-photon excitation wavelengths of most endogenous pigments such as NADH or flavins [161], which significantly reduces the on-focus damage and unwanted auto-fluorescence. This explains why Cr:forsterite lasers can increase the excitation intensity for generating THG without incurring tissue damage. Owing to these least invasive properties and highest penetration depth of wavelengths, Cr:forsterite lasers have been widely used in pre-clinical [92–95,105] and clinical studies [104,111,112,116,162–164] *in vivo*. Liu and co-workers employed this laser to develop a harmonic generation microscopy for the virtual optical biopsy of tumor microenvironments and tissue inflammation. The authors tracked collagen remodeling in melanoma microenvironment and extracted quantitative features for diagnostics [105].

3.3. Yb:fiber lasers

With a fiber amplifier, the ytterbium-doped fiber laser can produce 1030 nm pulses with a 300-fs pulse width and 40-nJ pulse energy. Using fiber-based OPO, this light source can be used to perform TPF and CARS multimodal microscopy [165]. If

the operating pulse energy of the Yb:fiber laser is reduced to the 1 nJ energy level (e.g., using dispersion compensation instruments), the pulse width can be optimized to 30 fs and the laser can be used for TPF, SHG, and THG microscopy [166].

3.4. Soliton-self-frequency shifted Er:fiber lasers

Tunable ultrafast lasers such as Ti:sapphire can only operate around a single wavelength. For multiple label imaging, researchers typically tune the wavelength for each label or choose a compromise wavelength that can excite them all. This arrangement induces bleed-through problems and reduces the contrast of fluorescence microscopy. Besides, for fast biological events such as neuronal action potentials or cellular circulation, multiple wavelength NIR femtosecond sources are required. To resolve this problem, we used a 400-nJ-energy, 1550-nm-wavelength Er:fiber laser to excite a large mode-area photonic crystal fiber and generate multiple solutions at 1900 nm and 1728 nm through a soliton-self-frequency-shift (SSFS) mechanism. After SHG, we obtained 775 nm, 864 nm, and 950 nm femtosecond sources for multiple labeling TPF imaging [167]. Using this SSFS mechanism, by choosing larger photonic crystal rods, the 1550 nm source can be efficiently red-shifted to generate intense 1700 nm light sources and thus realize deep-brain three photon fluorescence microscopy [133].

3.5. Laser diodes

Fig. 4D shows that many semiconductor-based materials can be used as light sources. Although the tunable range spans 630–900 nm (GaInAlP and GaAlAs), 710–850 nm (AlGaAs/GaAs), 900–1000 nm (InGaAs/GaAs), and 1000–1650 nm (InGaAsP/InP), laser diodes, which are commercially available and sufficiently powerful ($P \geq 1$ W) for biomedical theranostics applications, are limited to several discrete wavelengths that fall in the optical windows of the skin [131,132]. Most frequently, laser diodes operate in the 635–670 nm, 780–830 nm, 905–915 nm, 920–980 nm, 1064 nm, 1260 nm, and 1550 nm wavelengths, with an optical power above 1 W. Other wavelengths are not easily available, with a power of ∼100 mW.

4. Smart NIR linear and nonlinear optical nanomaterials

4.1. NIR linear optical nanoparticles

Using linear optical materials, fluorescent molecules in the visible range (∼400–650 nm), such as fluorescein dyes, rhodamine-related dyes and others [168] have been widely used in bio-sensing, immunoassays, Western blot detection and high-throughput devices., but have been less utilized for *in vivo* measurements. However, indocyanine green (ICG)-encapsulating polymers (e.g., polylactic-co-glycolic acid [169] and poly(allylamine hydrochloride) [170]), -micelle [171,172], -lipid [173], -human serum albumin [174], -mesoporous silica [175,176], -silica/Au [177], silica-poly(ε-caprolactone) [178] and -gold nanomaterial [179] composites are available for NIR brightened and robust bio-imaging detection and for photo-thermal energy conversion. The stability of ICG dyes can be improved by embedding them into polymers and inorganic nano-capsules. Another example is the IR-820 dye encapsulated in 1,2-Distearoyl-*sn*-glycero-3-phosphoethanolamine (DSPE)-mPEG500 polymer nanoparticles through a hydrophobic-hydrophilic self-assembly interaction method developed by Chu et al. [180]. These copolymer nanoparticles are much brighter than the aggregates of IR-820 powder (aggregation-caused quenching). By using a red excitation light near the NIR-I window, blood vessels at the depth of 500 μm could be visualized to obtain 3D reconstructed images of both the vasculature and brain signaling *in vivo*. A new bis(propylthio)tetrathiafulvenyl[i]dipyrido-[3,2-a:2′,3-c]phenazine (TTF-dppz) compound with λ_{abs} = 750 nm and λ_{em} = 975, 986, 1009, and 1020 nm was developed by Lapadula et al. [181]. After conjugating the Yb(III) molecular complex to the surface of silica nanoparticles (∼100 nm), this silica-based fluorophore absorbed and emitted in the NIR region (λ_{abs} = 750 nm, λ_{em} = 983 and 1050 nm).

Notably, fluorescent organic nanoparticles that consist of conjugated polymer dots [182,183], conjugated polyelectrolyte dots [184–186], conjugated carbon nanodots [187], or polymer-encapsulated dye molecules [188–190] have attracted considerable attention for bio-imaging applications, owing to their relatively high fluorescence emission quantum efficiency, photo-stability, and low cytotoxicity. However, only a few reports have successfully demonstrated the emission of organic nanodots that emit fluorescence in the NIR wavelength regions [191], which has limited their practical applications for bio-imaging of deep tissue. The excitation and emission peaks within the far-red/NIR wavelengths are highly desirable and match the tissue-transparency window for targeted *in vivo* fluorescence imaging and cancer diagnostics. Bioluminescence does not require optical excitation [192], but its spatial resolution is poor owing to tissue scattering. Another strategy is to employ the NIR absorption of conductive polymers in organic electronics and organic solar cells [193,194], such as polypyrrole [195] or poly-(3,4-ethylenedioxythiophene):poly(4-styrenesulfonate) (PEDOT:PSS). They provide strong photoacoustic contrast, achieve effective photo-thermal ablation [196], and have organic stealth for long-term circulation.

In addition to the aforementioned organic nanoparticles, yielding linear response functions in the NIR region, carbon nanotubes bear the promise for improving the efficacy of photo-thermal cancer therapy and the positional accuracy of treatment under the guidance of optical imaging, owing to the unique electronic states assisting electronic transitions in the UV–visible-NIR regions. The fluorescent contrast of dye label-free carbon nanotubes can be excited at 395 nm [197], 488 nm

[198], and 660 nm [199]/808 nm [200], yielding emission bands at 485 nm, 530 nm, and 900–1400 nm, respectively. Therefore, researchers have validated that laser light at 785–1100 nm can damage cancer cells after cellular uptake of single-walled carbon nanotubes (SWNTs) [201–203]. However, two major drawbacks associated with the use of SWNTs are related to their effects on the human body [204]. One issue is the toxicity of SWNTs with respect to cells and organs, which remains controversial [205,206]. Another limitation is the water dispersion of SWNTs in physiological environments.

4.2. NIR nonlinear optical nanoparticles

In most cases, inorganic solid samples can promote THG owing to a large difference between the refractive indices of particles and media (e.g., air and liquid) [207–209]. Metal oxides are characterized by high refractive indices, compared with both water and physiologically relevant media (n = 1.33). In addition to the intrinsic refractive index difference, the third-order nonlinear optical properties of sol-gel-derived V_2O_5, Nb_2O_5, and Ta_2O_5 thin films are primarily dominated by the lengths of metal–oxygen bonds. In fact, Tadanori et al. reported that transition metal oxides with the smallest l_b exhibit the highest third-order nonlinear susceptibility $\chi^{(3)}$. Conversely, non-transition metal oxides yield high $\chi^{(3)}$ as a result of a large l_b [208]. In THG microscopy coupled with nanoparticles, the THG signal under intense illumination converts three photons into one photon with a wavelength equal to one-third of the incident wavelength, and decreases the background owing to the cell auto-fluorescence.

Non-centrosymmetric metal oxides with harmonic generation properties have been extensively investigated [210]. ZnO is an n-type semiconductor that has a band gap of ~3.37 eV. The linear and nonlinear PL behaviors of ZnO nanoparticles are related to the intrinsic direct band gap and oxygen-related defects associated with the surface trapping states [211,212]. Owing to its anisotropic crystal structure, ZnO has been used for frequency conversion in SHG microscopy with an amplified Ti:sapphire laser at 800 nm (80 fs, 2.0 W, and 1 kHz) [207]. The enhancement of SHG signals is affected by the lattice atomic structure [213] and polar orientation [214].

Various multiphoton nonlinear optical processes have been studied in Cd-based QDs [119,215]. However, relatively little attention has been paid to the generated multiphoton fluorescence signals of graphitic carbon nanodots [216]. Eu-doped TiO_2 hollow nanoshells provide a new concept for two-photon fluorescence microscopy imaging of HeLa cervical cancer cells using a Ti:sapphire laser at 705 nm (3 W and 120 fs) [217]. The energy relaxation from the two-photon excitation of TiO_2 to Eu^{3+} ions contributes to the red emission at 617 nm. In contrast, depositing Eu ions in the shells of $KTiOPO_4$ single-crystal nanoparticles yields a dual light-emission property. The emission bands of as-obtained core-shell nanoparticles can be easily tuned to generate SHG from the $KTiOPO_4$ core (femtosecond laser λ_{ex}: 990 nm, pulse duration of 100 fs, repetition rate of 86 MHz, average power of 1 mW) and red photo luminescence (PL) from the shell [continuous wave (CW) laser λ_{ex}:532 nm, 10 mW] [218].

Two-photon fluorescent probes comprised of a two-photon fluorophore 4-(bis(4-(4-(diphenylamino)styryl)-phenyl)amino) benzaldehyde [219], phenyl thiourea linker, and amino triphenylamine dendron chelated, exhibited efficient TPF detection of Hg^{2+} in a wide dynamic range of concentrations (5 nM to 1.0 μM) [220]. Organometallic compounds (e.g., cyclometalated platinum (II) complexes) can be used for two-photon emission live-cell imaging [221,222]. Besides, Pt-based molecules have been also established as anticancer drugs that work by intercalating DNA [223–225].

Regarding organic dyes, molecules such as 1,1,2,3,4,5-hexaphenylsilole (HPS) and bis(4-(N-(1-naphthyl)phenylamino)-phenyl)fumaronitrile (NPAFN) can be loaded into polymeric micelles to form nanocarriers. These nanoconjugates exhibit good protection of the hydrophobic dye and provide high fluorescence intensity for imaging live cells with a low toxic impact [226]. The aggregation of aromatic dyes via the π-π interaction aids in the generation of a strong fluorescent intensity.

Ultra-bright organic dots, consisting of 4,7-bis[4-(1,2,2-triphenylvinyl)phenyl]benzo-2,1,3-thiadiazole (BTPEBT) aggregates, exhibit an aggregation-induced evolution of TPF [227] (Fig. 5). By using a femtosecond Ti:sapphire laser with λ_{ex} = 800 nm, the aggregation-induced emission of BTPEBT can be applied to observe smaller capillaries in 3D imaging of the brain, bone marrow, and ear skin.

Similar aggregation-induced two-photon emission was also observed in nanoparticles using 9,10-bis[4′-(4″-aminostyryl)styryl]anthracene (BDSA) derivative [228,229], pyran derivative, distyrylanthracene derivative [230], perylene-3,4:9,10-tetra carboxylic bisimide [231], and 2-(2,6-bis[(E)-4-(diphenylamino)styryl]-4H-pyran-4-ylidene)malononitrile [232]. These organic dyes in silica composite produced nano-sized hybrids and allowed for cancer cell imaging combined with the indirect excitation of a photosensitizer through two-photon excited energy transfer. Coating this NIR organic moiety on nanomaterials can improve the performance of multiphoton nonlinear optical processes. For example, the surface of Au nanorods coated with NIR polypyrrole (PPY) allows the flux of hot electrons to PPY to perform intracellular TPF imaging. This nonlinear process can be combined with two-photon excited photo-thermal therapy for treating HeLa cells using an 880-nm-wavelength laser with the fluence of 0.86 J/cm^2 [233].

4.3. Multiphoton up-conversion of lanthanide nanoparticles

Another strong advantage of lanthanide nanoparticles is the nearly perfect photo-stability of lanthanide-doped bio-labels. Neither photo-blinking nor photo-bleaching has been observed in these materials, which implies these can be used for long-term observations, such as studying time-dependent processes or studying the ability to trace such bio-functionalized labels circulating within living organisms.
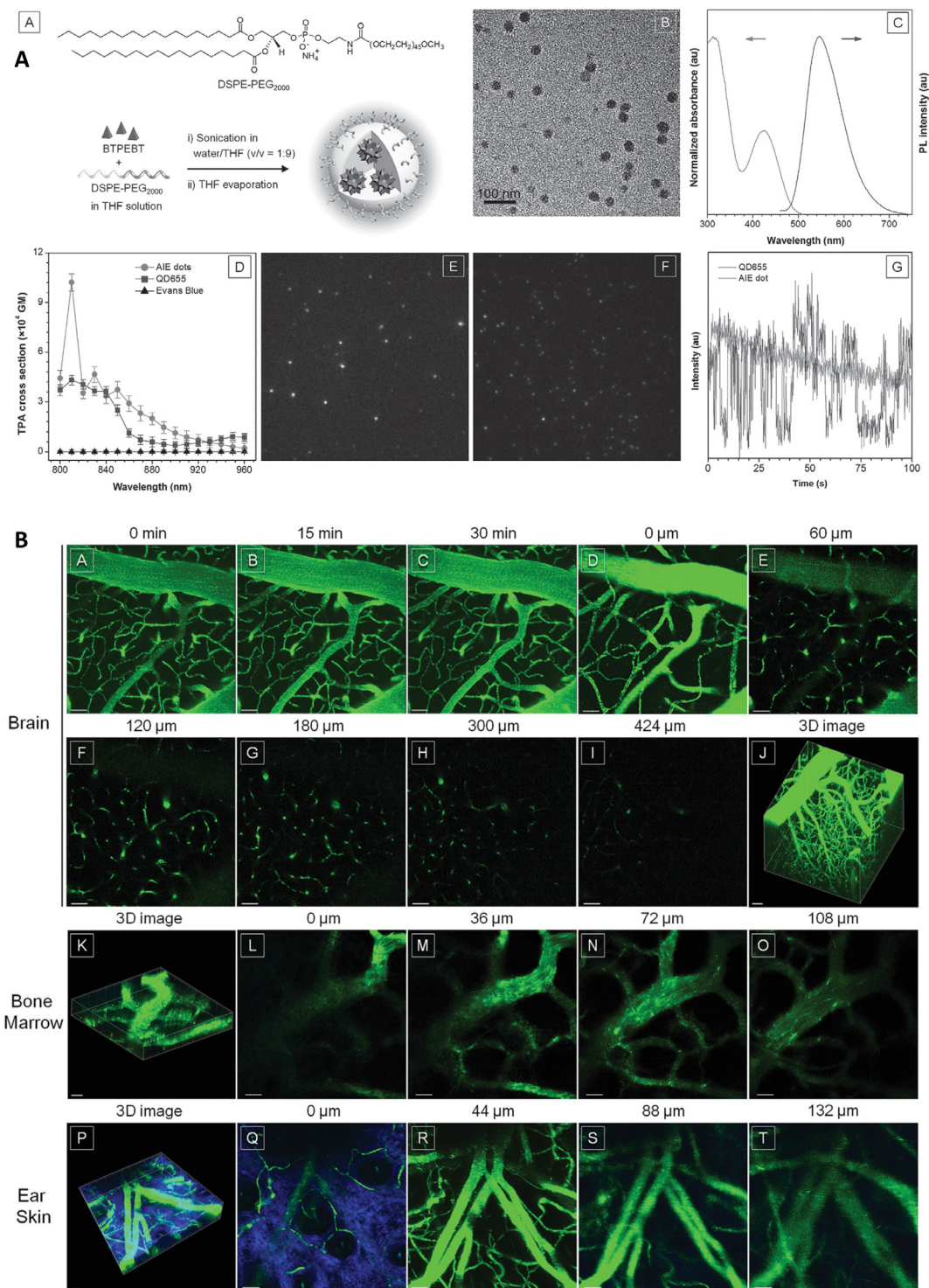
Fig. 5. (A) Schematic of aggregation-induced emission (AIE) dot fabrication. (B) TEM image of AIE dots. (C) UV–visible absorption and PL spectra of AIE dot suspension in water; λ_{ex} = 425 nm. (D) Two-photon absorption spectra of AIE dots and QD655 in water and Evans Blue in saline with 0.175 mg/mL bovine serum albumin (BSA). Data are presented as mean ± standard deviation (SD), (n = 3). (E and F) Wide-field (40 μm × 40 μm) luminescence images of single AIE dots (E) and QD655 (F). (G) Representative luminescence intensity time-traces for AIE dots and QD655. λ_{ex} = 488 nm for (E, F, and G). (B) Intra-vital TPF imaging of AIE-dot-stained blood vessels in different organs. (A–C) A time-lapse image sequence of maximum intensity projection showing blood vessels in the brain taken at 0 (A), 15 (B), and 30 (C) min post-injection of the AIE dots. (D–I) Images at various vertical depths of the brain. (J, K, P) 3D reconstructed images showing blood vessels in the brain, bone marrow, and mouse ear skin. (L–O, Q–T) Images at various vertical depths of the bone marrow and ear skin. Blue: second harmonic generation; collagen in dermis. Scale bar: 50 μm. λ_{ex} = 800 nm. Signal collected at 542 ± 27 nm. Reproduced with permission [227].

However, numerous additional features of these materials suggest interesting possibilities. First of all, lanthanide ions exhibit narrow- and multi-band absorption and emission. As a consequence, they exhibit large Stokes shifts, which helps to separate lanthanide emission from a much stronger excitation laser line. In addition, the narrowband and multiband emission makes multiplexing feasible, because numerous spectral codes may be designed for labeling multiple biological targets in the same samples, for example for marking a range of organelles in a single cell to unravel complex morphology, for simultaneously studying a few biological processes with, for example, a luminescence resonant energy transfer (LRET) technique, or for enhancing high-throughput screening performance to detect multiple rare cells or disease markers in human samples. The emission lines from Er, Tm, Ho, Sm, Tb, and Eu overlap partially, but spectral decomposition allows one to distinguish between the different spectral codes (Fig. 6). Although the locations of absorption/emission bands do not vary in terms of the wavelength, as can be found in quantum dots or organic dyes (only a relatively small variation in the spectral location and subtle structure of bands is observed across different host matrices), the color variation of Ln^{3+}-doped labels has been realized by engineering energy transfer pathways either passively (by varying the size [234,235], shape, composition, morphology [236,237], host matrix [238,239], surface ligands [240]; by admixing optically inactive ions such as K^+, Li^+ [241], Fe^{3+} [242]; or by substituting Gd^{3+} for Y^{3+} in $NaYF_4$ [243]) or actively (by varying the relative concentration of Ln^{3+} dopants [244–246], adding spectrally active ions such as Mn^{2+} [247,248] or Ce^{3+} [249,250]). Hierarchical layer-by-layer nanostructuring has been also demonstrated to yield a simple cascade multicolor emission [251]. Alternatively, more flexibility in designing optical codes can be achieved either by homogenous mixing of lanthanide complexes inside bar-codes (by mixing defined different color UCNPs within single SiO_2 or polyethylene glycol (PEG) beads [252]) or by doping lanthanides independently into cores and shells in active-core-active-shell nanoparticles [88]. Interestingly, owing to the relatively long luminescence lifetimes of lanthanides, the ability to intentionally design optical codes in the time domain has been previously predicted [253] and demonstrated [254,255].

The features of lanthanides become even more interesting when it comes to biosensing, and owing to multiple up-conversion emission spectra spanning the visible and NIR spectral regions, ratiometric biodetection becomes possible at increased depths; one of the emission bands serves as a reference, while the other is modulated proportionally to the concentration of the analytes. For example, LRET biosensors have been demonstrated, such as DNA hybridization or enzyme activity biosensors. In addition, pH- or [Hg]-sensitive probes were designed based on such ratiometric detection. This technique relies on the donor's emission quenching (DQ), non-radiative LRET, or inner filter effect (IFE), where only one of many Ln^{3+} up-converted emission bands (e.g., the one at 470 nm of Tm^{3+} emission) overlaps with the absorption of an acceptor (DQ, LRET) or sensitive chromophores (IFE), while the other emission bands (at 650 nm or 800 nm of Tm^{3+} emission) remain unaffected. Since the chromophores used in such bio-sensors are capable of enabling biological recognition (DQ, LRET) or responding to changes in the local chemical environment (e.g., changes in ionic concentrations) by changing the absorption
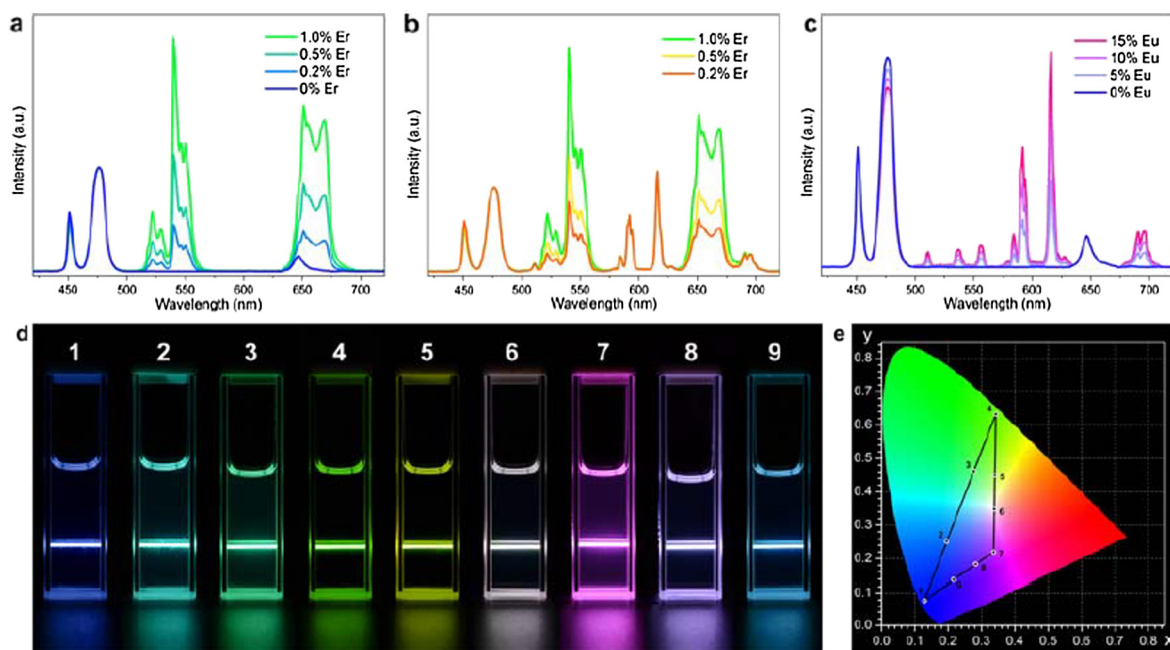
Fig. 6. Multicolor emission of (a) $NaGdF_4$:Yb,0.5%Tm, x Er@NaGdF_4:Yb@NaNdF_4:Yb, (b) $NaGdF_4$:Yb,0.5%Tm, xEr@NaGdF_4:Yb,15% Eu@NaNdF_4:Yb and (c) $NaGdF_4$:Yb,0.5%Tm@NaGdF_4:Yb, xEu@NaNdF_4:Yb colloidal solution of up-converting active-core-active-shell lanthanide doped nanoparticles [88]. (d and e) show illustrations of up-conversion and the corresponding Commission Internationale de l'Eclairage (CIE) coordinates, obtained for colloidal solutions of active-core-active-shell UCNPs. Reproduced with permission [88].

spectra (IFE), only one emission band is modulated, while the other serves as a reference for quantitative measurements. Examples of such ratiometric biosensors include pH [256], carbon dioxide [257], ammonia [258], mercury [259], glucose [260], cyanide anions [261], hydroxyl radicals [262], and oxygen [263] sensing. A similar idea was employed by Kang et al. to study the release characteristics of the ibuprofen drug. The up-conversion emission quantum yield was proportional to the amount of released ibuprofen [264], generating a platform for drug delivery and drug release monitoring.

The most severe drawback of Ln nanoparticles is a relatively low quantum efficiency owing to their low absorption and emission cross-sections, which result from a forbidden f-f optical transition. The efficiency, although much lower than that of organic dyes or quantum dots, is not prohibitive for bio-applications, and ultrasensitive immunoassays and detection of a few cancer cells have been successfully demonstrated. This low efficiency is also the outcome of a large surface to volume ratio of nanomaterials. A substantial number of doping ions are located close to the NC surface and their excited states are thus susceptible to chemical microenvironment, nanocrystal defects, ligands and solvents, which have been recognized as quenching mechanisms. However, these side effects may be relatively easily reduced using core-shell lanthanide-doped nanoparticle architectures. It has been shown, that ~4-nm-thick passive (un-doped) shells are suitable for complete surface passivation and for reducing the susceptibility to the nanoparticles' surface chemistry or to solvents [265]. A number of methods have been sought for improving the up-conversion emission intensity in nanoparticles. Basically, (i) surface passivation [266], (ii) passive (K^+, Li^+)/active ion (Nd^{3+}, Mn^{2+}) co-doping [247,248,267,268], (iii) plasmonics [269], (iv) increasing the concentration of the sensitizer (Yb^{3+}) [270], (v) host selection [271], and recent smart active-core-active-shell nanoparticle designs [272–274] are used to achieve this goal, with different outcomes. The photo-physical properties of lanthanide-doped nanomaterials have been extensively reviewed [275–278]. In addition, the biomedical properties and applications have been discussed in a growing number of excellent review articles [90,275,279–288].

Owing to the numerous photo-physical advantages of UCNPs that were briefly reviewed above, lanthanide-doped nanoparticles have been used in (i) passive, (ii) modulating, and (iii) active biomedical applications (Fig. 7) [288]. Passive applications include the use of the nanoparticles as contrast agents in fluorescence microscopy, MRI (owing to the accumulation of Gd^{3+} ions, e.g., NaGdF4 matrix [289–292]), X-ray imaging, or PET imaging (owing to the F^{18} isotopes attached to the nanoparticles' surface [293,294]). Often, these imaging modalities can be combined in pairs [292,295–298] or triplets [299]. Recently, hexamodal imaging has been demonstrated with PoP-coated UCNPs, which combined CT, PET, up-conversion, Cherenkov luminescence, photoacoustics, and FL [20]. The fluorescence contrasts of UCNP labels were so sensitive that as few as 10 stem cells could be detected *in vivo* [300] for at least one week after delivery [301].

Active applications include methods in which UCNPs affect biological tissue; examples include the possibility of hyperthermia (local overheating of cancerous tissue) with UCNPS directly [302,303] or with UCNPs bound to Au/Fe_2O_3 nanoparticles [304–306], (chemo-, geno-) therapeutic drug delivery [307], or up-converted photodynamic therapy [308–313]. UCNPs
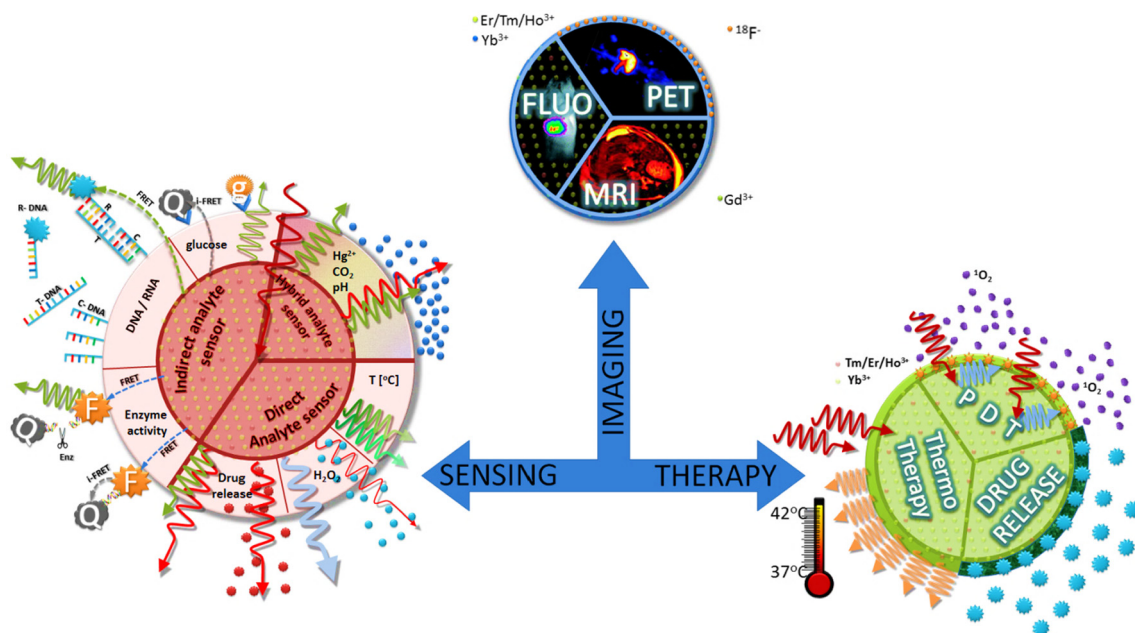
Fig. 7. State-of-the-art biomedical applications of lanthanide-doped (up-converting) nanoparticles. Active, passive, and modulation applications of UCNPs, which respectively relate to the direct impact of UCNPs on surrounding tissue (through temperature or PDT activation), lantern type contrast agents (PET, MRI, fluorescence), and modulation of spectral properties of UCNPs by either environment (e.g., CO_2, pH; (a)) responsive bio-molecules (hybrid sensors), FRET-based (quenching (b), nucleic acids hybridization (c), enzymatic (d)) sensors, or analytes (direct analyte sensors, e.g., temperature (g), drug (e), H_2O_2 (f)) [288].

are not very efficient in causing hyperthermia owing to a relatively weak absorption of light by lanthanides and thus, a relatively low heating efficiency. UCNPs are also not very well suited as drug delivery agents, because a crystal (and thus solid and firm) matrix is necessary to host lanthanides for making them luminescent. For this reason, there is no way to introduce external compounds into a system containing UCNPs. UCNPs can, however, be covered with mesoporous SiO_2 or polymeric shells, which may carry and release drugs. Prolonged and controlled release of drugs may be of high importance. $LaF_3:Yb^{3+}$, $Er^{3+}/nSiO_2/mSiO_2$ microspheres [314] and $NaYF_4:Yb^{3+},Er^{3+}/nSiO_2/mSiO_2$ [264] microspheres were demonstrated to sustain and control the release of ibuprofen that was loaded into mesoporous shells of UCNPs.

The most spectacular and promising example of using UCNPs in theranostics is NIR-initiated photodynamic therapy, also termed up-conversion photodynamic therapy. Such hybrid up-conversion-PDT nanoparticles include UCNPs as luminescent bio-probes in the core, and simultaneously photosensitizing molecules (e.g., chlorin e6) are either covalently attached to the surface of nanoparticles or embedded in mesoporous SiO_2/PEG shells. In most of these applications, UCNPs act as light transducers, converting light from NIR to visible or NIR spectral region, which basically increases the penetration depth of the excitation light and thus enables photo-biosensing [315,316] and phototherapy [305,317–319] of heterogeneous tissues. Moreover, UCNPs are well suited for theranostic applications [320,321], because it is relatively easy to combine several functional features within individual nanoparticles.

5. Application fields of NIR nanomaterials in cancer theranostics

Conventional cancer treatment modalities, such as surgery, radiation therapy, and chemotherapy, all result in serious side effects and in many cases (especially for rapidly developing cancers or tumors within delicate tissues in the head and neck), do not achieve complete removal of the cancer cells. For this reason, a single underlying biological process that could allow for selective targeting and destruction of diseased cells while preserving their healthy functional neighbors is highly desirable. However, the problem of successful cancer treatment originates from the complex nature of cancer development. Cancer cells originate from the host, exhibit un-regulated proliferation, and are often found to migrate [322]. Moreover, individual tumors display heterogeneous properties in terms of structure, biochemical behavior, nature of the surrounding microenvironment, and susceptibility to their biochemical environment and susceptibility to treatments. Despite the conceptually interesting idea of using antibodies to target drugs to cancerous tissues and cells [323–326], very few significant successful attempts have been made to date. This is largely for the following reasons [327]:

(1) Difficulties in achieving tumor-specific antibodies that also display high affinity.
(2) High biochemical (i.e. antigen) heterogeneity of tumors throughout their mass.
(3) At the organ scale, the antibodies either do not reach the tumor site or do not easily penetrate the tumor, and therefore remain in the tumor vasculature.
(4) At the cellular scale, the antibodies are generally not designed to penetrate the tumor cells and thus the cytotoxic agents may not reach the most sensitive intracellular sites (such as the mitochondria).

To investigate and understand these problems in the microenvironment of a specific biomedical context in an *in vivo* setting, one needs molecular probes with NIR optical contrasts. One also needs to design an appropriate imaging method for NIR excitation and detection. Once this is achieved, cancer cell distribution, the microscopic pharmacokinetics of nanomedicines, delivery of therapeutics, cell responses, and cell-cell interactions can be visualized and analyzed. This integration of NIR nanomaterials (i.e., ICG-encapsulating polymer [169–174], conjugated polymer dots [182–186], luminescent carbon nanomaterials [201–206], biocompatible Ag_2S nanoparticles [42,328], aggregated induced emission (AIE) dots and nano-oxides [211–214,216,217], dyes [219–227], plasmonic nanoparticles [329–338], upconverting lanthanide nanoparticles [234–240,242–255], and upconverting lanthanide nanocomposites [289–314]) with the NIR imaging system provides a proof-of-concept platform and visual evidence critical for the success of translational cancer nanomedicines.

5.1. Biosensing assays

Understanding the physical and chemical features of the tumor microenvironment provides an insight for the design of nanomedicines with better targeting and delivery efficiencies. The physiological parameters of interests include the partial oxygen pressure pO_2, pH value, and glucose level, permeability of the blood vessels and ROS levels. To visualize the conditions and dynamic processes *in vivo*, conjugated polymer and silicate nanoparticles have been developed as important molecular probes with NIR optical contrasts. For example, phosphorescence probes that can detect pO_2 [31–35] are useful in understanding the correlation between a hypoxic environment and the angiogenesis process [339,340]. In the material chemistry of organic light-emitting diodes, transition-metal based phosphors and molecular complexes have been developed as efficient phosphorescence chemicals [341,342]. Their strong spin-orbital coupling allows for efficient phosphorescence, which allows them to serve as sensors of pO_2 [343]. Among them, metalloporphyrin complexes [339,340,344], Ruthenium (II) complexes [345] and Iridium(III) complexes [346] have been designed for pO_2 sensing and imaging. For deep tissue pO_2 measurement, additional dyes like coumarin-343 have also been incorporated as two-photon antenna to raise the phosphorescence quantum yield [347].

Surface passivation is critical for these phosphorescence probes in order to avoid self-aggregation or adsorption to bio-macromolecules [33], although this may alter their oxygen sensitivity and result in erroneous measurements. Regarding the hypoxic condition in the tumor microenvironment, it is well known that this physiological property can change the glucose metabolism of cells from oxidative phosphorylation towards lactic acid fermentation, a less efficient way for cell to obtain energy currency, namely adenosine triphosphate (ATP). In this case, cells will take up more glucose to produce the same amount of ATPs and therefore become more acidic. This shift in acidity can be quantified using pH-sensitive fluorescent dyes [348]. Carried by pH-low insertion peptides, pH-sensitive fluorescent peptide probes can specifically measure the pH value at the cell surface [349]. Using dextran loading, Cong et al. have also developed a pH-activated NIR fluorescent probe (polylysine-liked rhodamine/IR783/PEG/In^{3+}-DOTA/dextran). These designs show that peptides or dextran could serve as targeting carriers for the sensing of ions around tumor cells [350].

The hypoxic tumor can further induce angiogenesis, producing a vasculature with an abnormal network. The endothelial surface of the vasculature is often fenestrated with gaps between endothelial cells, due to a decrease in the number or adhesiveness of pericytes [351]. These gaps can however enhance the permeation and accumulation of nanomedicines in circulation. To evaluate the particle size that results in maximal accumulation, researchers have commonly used fluorescent dextrans with molecular weights ranging from 20 to 2000 kDa [352,353]. To achieve deep tissue analysis of vessel permeation, NIR macromolecular dye-tagged dextrans therefore hold great promise.

Many proof-of-concept biosensors have been developed using UCNPs combined with bio-responsive molecules. While the UCNPs are not susceptible to changes in the chemical or bio-environment, they may be excited at much greater depths within the tissue mass. Due to multi-band emission and the overlap of lanthanide ion emission with the environment-sensitive molecules anchored at the surface of the UCNPs, ratio-metric bio-sensing using IFE can be achieved and sensitivity can be enhanced. Such types of biosensors have been shown to be effective in studying immunochromatographic assay (e.g. *E. coli* [354] and human chorionic gonadotropin [355] detection), DNA-hybridization [356,357], enzyme activity [358], pH value [256], carbon dioxide [257], ammonia [258], mercury [259], glucose [260], cyanide anions [261] or oxygen [263] concentrations. These sensors expand the well-known properties of some organic dyes with the ability to read the biosensor response at NIR photoexcitation wavelengths.

In the context of photodynamic therapy, it is of utmost importance to understand whether ROS are actually released around tumors. The use of organically modified silicate (ORMOSIL) to load ROS sensitive dyes and a reference dye to perform ratiometric fluorescence measurements is common [359–362]. The polymer matrices used can inhibit interaction of the dye with intracellular proteins, protect the dye from degradation, and inhibit undesired sequestration into subcellular compartments. A common strategy is to design systems where the fluorescence quenching mechanism occurs on the surface of metallic nanoparticles [363,364]. As long as the ROS interact on the surface-coating of ligands on metallic nanoparticles, the fluorescence will be quenched. Therefore, these types of nanoprobe can be used to sense ROS level in cells with excellent spatio-temporal resolution.

5.2. NIR imaging methods

Optical imaging relies on the illumination of light waves on a subject, the generation of contrast by molecules within, and the mapping of responses by an optical system and cameras. Therefore, the best-achievable resolution and imaging depth of an optical imaging system will be determined by the illumination and collection methods. Depending on the desired depth and the scattering properties of tissues, the types of optical imaging system can be divided into either diffusive or ballistic. For large-scale and whole-body imaging, nanomedicines usually reside in tissues at a depth several times the scattering lengths of light. The signal photons can be scattered multiple times, causing a loss of coherence of the wave-front before they leave the turbid tissue environment. In this case, the typical resolution of diffused photon imaging will be on the order of a centimeter. For *in vivo* microscopy of complicated tumor microenvironments, a ballistic imaging system with sectioning capability should be adopted. In this case, nanomedicines are illuminated by a focused laser beam and the imaging depth will be well-within the scattering length of light. For the NIR light source, the ballistic length is 300–500 μm for skin [131] and 1.5 mm for embryos [365]. The sectioning capability can be achieved using either a confocal imaging method, laser-scanned nonlinear optical microscopy, or light-sheet illumination. The resolution of a ballistic imaging system is typically sub-micron, so it can reveal the structural and sub-cellular details of the tumor microenvironment. For imaging of tumor vasculatures, the imaging depth should be deeper than the scattering lengths. To obtain a sufficiently high spatial resolution for vasculature imaging, the photoacoustic contrast should be considered. Since acoustic waves have less attenuation and less diffraction than optical light, the lateral resolution of photoacoustic imaging is typically 40 μm at 3-mm imaging depth. This resolution is much better than that of diffused optical imaging and can easily map tumor vasculatures.

To achieve low energy loss (i.e. prevent absorption and scattering at short wavelengths) and deposition in biological tissues, anisotropic Au particle [366], Ag$_2$S dots [42,328], CNT, dye-loaded composites [169–174], and nonlinear nanomaterials [211–214,216,217], upconverting lanthanide nanoparticles [234–240,242–255,289–314] have proven to be satisfactory choices of contrast agents for providing emission in the long wavelength region after long wavelength excitation in deep tissues.

5.3. NIR fluorescence for image-guided surgery

Various radiological imaging modalities (CT/MRI/PET) are used as a preoperative assessment for surgery guidance. During surgery, NIR contrast agents may be administered intravenously or intraperitoneally and visualized using an NIR fluorescence imaging system with adequate NIR excitation light, collection optics, filters, and a camera sensitive to NIR fluorescence emission light [367] (Fig. 8). For higher resolution diagnostics or intra-operative navigation, a microscopy imaging modality is required. For example, the biopsy of sentinel lymph nodes (SLN) around tumors is a critical diagnostic procedure used for the typing and staging of tumors. The administration of NIR fluorescence agents *in situ* combined with large-scale fluorescence imaging can help doctors visualize SLN [368]. In clinical practice, the *Food and Drug Administration*-approved ICG has been used off-label for the tracing of SLN. ICG excitation and fluorescence wavelengths are 780 and 822 nm, respectively, which is beneficial for deep-tissue real-time imaging. To increase solubility and fluorescence yield, a common strategy relies on the adsorption of ICG with human serum albumin. However, compared with ICG, type II semiconductor QDs can provide brighter 850 nm fluorescence for SLN imaging *in vivo* [369]. To provide favorable accumulation and longer retention of the NIR contrast agent in the draining SLN, the appropriate particle must be selected (20–50 nm) [370]. For deeper SLN imaging, several photoacoustic contrast agents have been developed. Perfluorocarbon nanoparticles loaded with NIR fluorescence dyes can achieve simultaneous NIR optical and photoacoustic imaging of SLN *in vivo* [371]. Whole-body lymph nodes have been visualized using a combination of NIR excited photoacoustic imaging and semiconducting polymer nanoparticles [372].

In the surgical resection of tumors, clinicians commonly used larger boundaries around the major nodule to maximize the clearance of cancer cells. But for organs like the brain, extra resections may result in a loss of psychological and motor functions. Besides this, for cancers with irregular or dendritic shapes, cancerous tissues may be present at the boundary of the excised lesions. Therefore, the residual cancer cells may result in recurrence and affect the prognosis after surgery. Thus, to identify tumor cells from adjacent non-tumor cells and critical structures like neurons intra-operatively, a common strategy is the development of contrast enhancement methods or fluorescence probes to augment the visual differences between normal and cancer cells.

Compared to 10–100-nm sized crystals, a contrast agent designed on a molecular scale (<10 nm) has the benefit of better penetration and uniform distribution at specific sites of the body. Therefore, several extrinsic fluorescence contrast enhancers have been developed for guided surgery [373]. These fluorescence probes can either target the metabolic features, or the hallmarks of specific cancer types. For example, the use of 5-aminolevulinic acid results in the accumulation of protoporphyrin IX in glioblastomas [374]. This porphyrin can be effectively excited at the Soret band (an intense peak in the blue wavelength region of the visible spectrum) and imaged at 600–750 nm NIR wavelengths. Another efficient approach is to use protease-sensitive probes, where the red fluorescence of cell-penetrating peptides can report the presence of tumor-associated matrix metalloproteinases (MMPs) [375] and thus the presence of residual tumors. To avoid damage to peripheral nerves during surgery, fluorescent peptides specifically bound to neural cells have been developed for systemic administration [376].
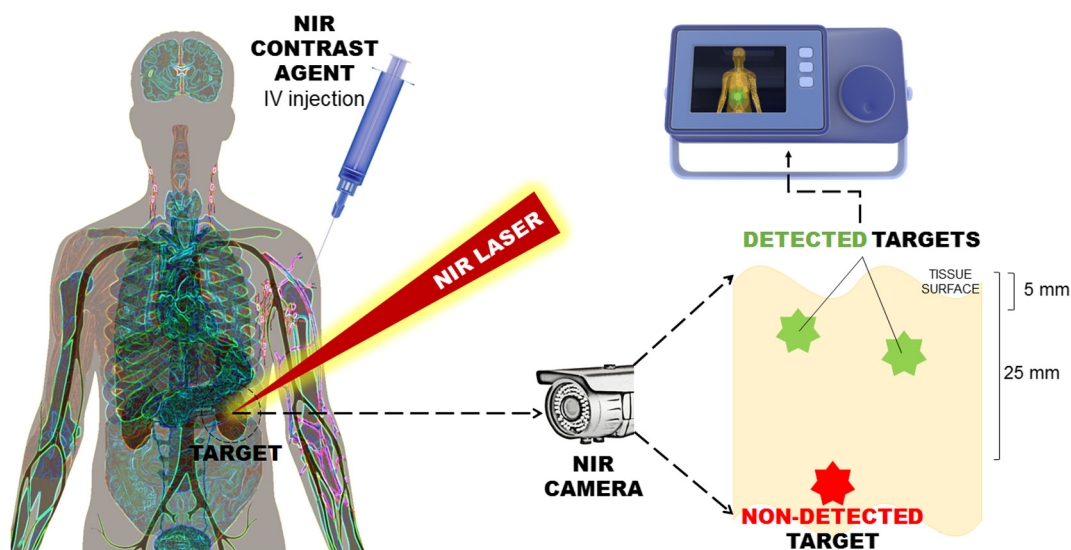
Fig. 8. NIR fluorescence for image-guided surgery. When performing surgery, an NIR contrast agent may be injected and monitored using an NIR fluorescence imaging system, with appropriate NIR excitation laser light and a camera sensitive to NIR fluorescence emission light in order to capture the signals and project them on a standard computer monitor or wall projector. Usually, targets up to 5–8 mm deep can be detected using NIR fluorescence imaging whereas a target deeper than 25 mm would not be detected.

5.4. NIR photo-triggered drug release

For better absorption or therapeutic efficacy, the time and place of drug release needs to be precisely controlled. For example, some pills or capsules carrying drugs have pH-sensitive coatings to avoid digestion in the stomach or intestine, in order to achieve specific colonic drug delivery [377]. To actively control the release of drugs from carriers, excitation using optical [4,455–341], acoustic [378,379] or magnetic [380] energy is required. These methods allow multiple dosages of drug to be achieved from a single administration with precise control of the timing, duration and magnitude. For light-activated drug release, the depth of action can be increased by illumination with NIR light [381]. For example, by exploiting the NIR absorption of ICG [382], the membrane of doxorubicin-loaded red blood cells can be thermally destroyed in order to achieve efficient and specific drug release. The SPR absorption of gold nanostructures can also enhance the local electric field and achieve NIR-triggered drug release [4]. For non-thermal release, a photo-labile linker that covalently bound a drug to dendrimers or dendrons has been developed [383]. To cleave a linker using NIR light, upconverting nanomaterials or two-photon excitation processes [384] can also be used. Changing the physical properties of loading matrices can also achieve controlled release. Successful processes include photo isomerization [385], photo-induced gel swelling [386], photo-reactive molecular valve [387], or the photo-decompression of particle sizes [388].

5.5. Photo-thermal therapy

Dark colored materials can absorb light and convert photo-energy into heat. This approach can be adopted for nanoparticles as means to treat tumors. As the nanoparticles absorb light energy, excited carriers will release their energy either through the emission of photons or through the generation of photons and heat. If the nanomaterial (i.e., Au [366,389], carbon [390,391], oxides [337,338,392–394], or dyes [174,180,382]) lack an efficient photon emission route, by using CW lasers as light sources, then most of the absorbed light energy will be converted into heat. In photo-thermal therapy (PTT), when the temperature of particles rises above 40 °C, adjacent cells will be abruptly damaged through pore formation, or will undergo apoptosis due to heat-shock [395].

Thermal therapies have been used since the 1980s for enhancing human metabolism and treating diseases (e.g. tumors in cancer therapy) [396,397]. In fact, the different thermal gradient readily changes tissue elasticity and blood flow rate [398,399], as well as inducing cell death pathways [400,401]. However, the thermal effect on cells in a changing microenvironment remains unclear because of the systemic host effects [402]. To avoid this uncertainty, controlled and localized heating is required for cancer treatment. For example, a carbon nanotube has been reported as an NIR-II light-to-heat converter for PTT of malignant cells [390,391]. The design of a multi-branched Au structure (~350 nm) resulted in a broadened absorption band extending to NIR wavelength [389]. Using a 1064 nm CW laser, both photo-thermal and photo-dynamic therapies have been achieved at a very low power intensity of 130 mW/cm^2. By special design, luminescent, lanthanide-doped, nanoparticles can serve as hyperthermia agents. For example, heavily doped Nd^{3+} can be used as nano-heater [303], imaging agent, and nano-thermometer [403], for remote tracing of temperature during hyperthermia. In addition to common plasmonic metal nanoparticles, a recent review manuscript has revisited the classification of NIR-absorbing non-metal nanomaterials for photo-thermal applications *in vitro* and *in vivo* [404].

5.6. Upconversion induced photodynamic therapy

Photodynamic therapy (PDT) was introduced 100 years ago [405]. This technique was used to treat various cancers, age-related macular degeneration, and actinic keratosis [406]. The activation of PDT requires spatial co-localization of three elements: light, a photosensitizer (PS), and oxygen. For a photosensitizer molecule such as porphyrin, part of the excited electrons may couple to triplet states through intersystem crossing. These long-lived triplet electrons may further produce ROS like singlet oxygen or free radicals. These ROS can destroy tumor cells directly, damage the tumor-associated vasculature, or activate an immune response against tumor cells [405]. Individual elements of the PDT procedure themselves are harmless and non-destructive, but as soon as they co localize, the singlet oxygen produced during PDT can oxidize critical cellular macromolecules such as lipids, nucleic acids, and amino acids, thereby inducing alterations in cellular permeability, damage to the plasma membrane, mitochondria and lysosomes [407,408] which in turn lead to cell death by necrosis or apoptosis [409].

Owing to the PS's preferential accumulation in cancerous tissues and cells, these cells are killed with higher spatial selectivity than chemotherapy or radiotherapy, and thus the secondary effects to patients may be considered as negligible. Currently, PDT treatment of numerous cancerous diseases (e.g. early lung cancer [410,411], Barrett's esophagus [412–414], bladder cancer [415,416], head and neck cancers [417], and skin cancers [418–420]) and non-cancerous diseases (e.g. age related macular degeneration [421], bacteria eradication [422]) have been approved.

Despite numerous successes in PDT treatment and numerous approvals for medical use, there are still many issues to be solved. Most of the PSs used to date display only a slight preference for malignant cells, often leading to significant skin photosensitivity and high uptake by healthy cells and tissues. The low uptake contrast between abnormal and normal tissues has stimulated biochemists to design third-generation PSs that are actively targeted towards diseased tissue. Unfortunately, PSs used for PDT have a tendency to aggregate owing to their planar aromatic ring systems, which also allows non-specific binding to bio-molecules (e.g. serum proteins such as albumins, lipoproteins, and high-density lipoprotein) [327]. This may lead

to difficulties in quantifying the biological activity and cytotoxicity of such conjugated and un-conjugated PS molecules, because the photo-physical and photo-chemical properties of such PS variants may differ significantly. In addition, such PS bio-conjugation, or PS-PS interaction, may decrease the PS's absorption coefficient, singlet state lifetimes, and triplet state yields, as well as the PS's excited state lifetimes. This in turn may affect the production of ROS during illumination and thus decrease the photo-cytotoxicity of the dye conjugates. Furthermore, as has been mentioned above, it is necessary not only to consider delivery of the PS to the target cell but also to get efficient accumulation of the PS at susceptible sub cellular locations.

Another severe drawback of conventional PDT treatment that hinders its broad adoption for solid high-volume tumors, and limits its use to only superficial carcinomas in epithelial tissues, is the low penetration depth of light suitable to photo-excite conventional photo-sensitizers. The approved photosensitizers usually absorb below 700 nm, but short-wavelength light undergoes significant scattering and absorption by tissue chromophores. Typically, porphyrin-based photosensitizers [Protoporphyrin (PpIX), Fotofrin, etc.] have a Soret band around 400 nm and a series of Q-bands at the green/red spectral regions [423,424]. Unfortunately, as described in previous sections, light in the 300–650 nm range will be strongly absorbed and scattered by pigments and heterogeneous structures in tissues. The effective region of conventional PDT is therefore rather limited. One approach to solving this issue has been through the use of light diffusers that can be inserted into the tissue to increase the effective volume of PDT treatment. The obvious disadvantage of such an approach is its invasive nature.

In order to overcome these drawbacks, an interesting idea has been proposed to combine photodynamic therapy with up-converting nanoparticles. Under NIR light, these up-converting nanoparticles demonstrate a relatively efficient up-conversion to the visible range and may trigger conventional photo-sensitizers (Fig. 9). Such an approach demonstrates some significant advantages over conventional approaches:
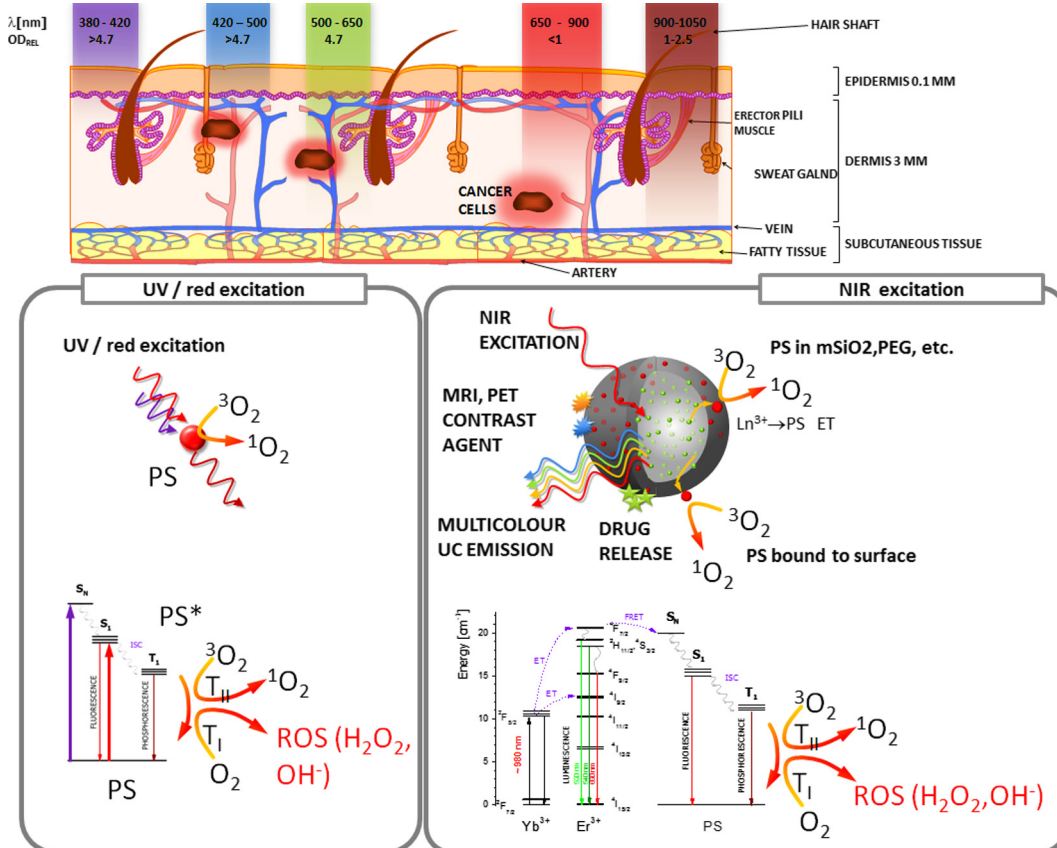
Fig. 9. Comparison of conventional photodynamic therapy (PDT) (left) and up-conversion PDT (right hand side) in terms of penetration depth and mechanism. Owing to the short wavelength of light typically required for photosensitizers, the penetration depth and PDT efficiency is usually limited to shallow skin layers. This is as a result of light scattering and absorption by skin/blood components (e.g. collagen, elastin, hemoglobin, etc.). Opposite to PDT, UC-PDT exploits NIR photoexcitation, which penetrates deeper into the skin layers and enables cancer treatment of larger masses. Conventional PDT, occurs by absorption, singlet → triplet inter system crossing, followed by free-radical (H_2O_2, OH^- or $^1O_2$) production, whereas UC-PDT occurs by the up-conversion process and indirect energy transfer to PS. While UC-PDT is less efficient in quantum terms than PDT, the use of NIR enables deeper light penetration and ultimately a more effective treatment.

1. Photosensitizer compounds encapsulated in mesoporous silica are protected from degradation in the complex biological environment. In addition, self-aggregation and conjugation to other bio-molecules (such as albumin) does not occur and consequently the PS photochemical properties are preserved. In addition, encapsulation limits their photo-bleaching and biochemical inactivation, thereby maintaining efficient ROS production during illumination leading to efficient photo-induced cytotoxicity.

2. Most of the current photo-sensitizers are hydrophobic, thus either polymer [425,426] or silica-based [309,427] shells will enable solubilization of these PSs [as UCNP@shell(PS)] in aqueous buffers.

3. The hybrid UCNPs@Shell(PS) NPs, upon bio-functionalization may offer the ability to target the PS to the desired cells. Chatterjee et al. were the first to demonstrate folate receptor targeting using UCNP-PS nanoparticles [428].

4. NIR radiation is used to initiate PDT, which offers an increased light penetration depth and suitability to treat larger tissue volumes. A new up-converting nanoparticle design has recently been demonstrated showing novel advancements using an active-core-active-shell design. By using Nd^{3+} primary up-conversion sensitizers, instead of the typical Yb^{3+} sensitizers, excitation light penetration depth was significantly improved. This is possibly a result of the significant reduction (around 25 times) in the absorption coefficient of water at 800 nm for Nd^{3+} vs 980 nm for Yb^{3+}. The overheating problem was also simultaneously diminished compared to conventional Yb^{3+}-RE^{3+} up-conversion pairs [145,429].

5. These advanced hybrid NPs may be designed to release their cargo (e.g. doxorubicin chemotherapeutic agents [307]) upon encountering the decreased pH levels often found in cancer tissues.

6. Numerous imaging modalities are also offered by UCNPs@shell(PS), such as up-converted multicolor (and thus multi-plexed) luminescence in the visible and NIR spectral region, or MRI imaging (through the use of Gd^{3+} ions within the UCNPs). Additionally, the UCNPs do not photo-blink, and are not susceptible to photo-bleaching, thus allowing for pro-longed visualization.

7. The shell may be intentionally designed to ensure a sufficiently long circulation time in the blood stream in order to tar-get tissues with a desired antigen profile via a receptor-mediated delivery systems or via an EPR mechanism [317,318].

The majority of the studies reported so far demonstrate a proof-of-concept for UC-PDT experiments. However, further research is required to (i) improve the efficiencies of every single step in the NIR light → visible light → PS → ROS path [430], (ii) design multimodal (PDT, drug delivery, fluorescence/luminescence/PET/MRI imaging) nanoparticles (iii) design smart NPs (e.g. that can release cargo upon an Ab-Ag interaction or upon pH lowering), (iv) bio-functionalize the NPs to achieve long circulation times and allow for highly selective targeting to the tumor sites. Due to the very low quantum efficiency of up-conversion (typically less than 1%) and strong power dependence, further research must be devoted to optimize the photo-physical properties of nanoparticles. One of the most important issues, is the development of methods for characterization that are capable of quantitatively comparing different approaches and that would then allow for optimization of theranostic agents in absolute terms.

5.7. Photo-dynamic therapy and photo-thermal ablation combined with NIR detection

The remarkably synergy between PDT and PTT has led to its development as a combination therapy that has achieved impressive results compared to the use of PDT or PTT alone. Several groups have demonstrated that complete tumor ablation can be achieved using a PDT/PTT combined therapeutic method [431]. The incorporation of photosensitizers onto the surface of a photo-thermal nanomaterial to produce a single particle composite [76,431–439] is the most common strategy used to achieve a photo-thermal/photo-dynamic combination therapy. Since NIR-based nanoparticles can be engineered to efficiently interact with NIR radiation, tracking and detecting these agents during therapeutic treatments is possible at a deep tissue level. This optical imaging-guided approach and the combination of PDT and PTT phototherapy has gained substantial attention and has become a prosperous field for meeting clinical needs without the need for adverse surgery, chemotherapy, or radiation treatment.

Wang et al. have designed a new nanohybrid of rose-bengal (RB)-conjugated Au nanorods for use as an efficient *in vivo* photo-dynamic and photo-thermal treatment for oral cancer [440]. Although rose bengal (RB) is a well-known photosensitizer that generates singlet oxygen species with a high quantum yield (~76%), the excitation wavelength is limited to 532-nm light irradiation and fails to produce NIR fluorescence [441,442]. However in 2013, Tae and co-workers synthesized NIR nanogels embedded with Au nanorods (GNRs) and Chlorin e6 (Ce6) for *in vitro* and *in vivo* photo-toxicity applications [431] (Fig. 10A and B). Before photon treatment, effective tumor accumulation *in vivo* was detectable using the red-NIR fluorescence arising from the Ce6 lumiphore within the nanogel. Compared to that of independent treatments with PDT or PTT alone, a better anti-neoplastic effect was observed with PDT followed by PTT. A similar study on a hybrid of iron oxide@Au and methylene blue (MB) was performed by Ray and co-workers [432], where the fluorescence imaging could be captured using the MB molecule (with excitation at 650 nm and fluorescence signal detection between 680 and 720 nm). Photo-ablation of HaCaT cancer cells has also been achieved through a synergistic combination of photo-thermal and photo-dynamic treatments. Using an alternative method, where Au vesicles are used to gel-encapsulate Ce6 PS, the SPR coupling effect in the Au nanoparticle monolayer resulted in NIR absorption peaks and thus enhanced the NIR PDT and photo-thermal tumor treatment (671 nm and 808 nm laser at 2.0 W/cm^2) (Fig. 10C). The accumulation within the tumor can also be tracked using a photoacoustic modality [443]. Simple assembly of the poly (dopamine) (PDA) nanoparticle followed by conjugation with Ce6 produced an excellent phototoxic PTT-PDT effect, with a combination laser irradiation of 670 and 808 nm and an
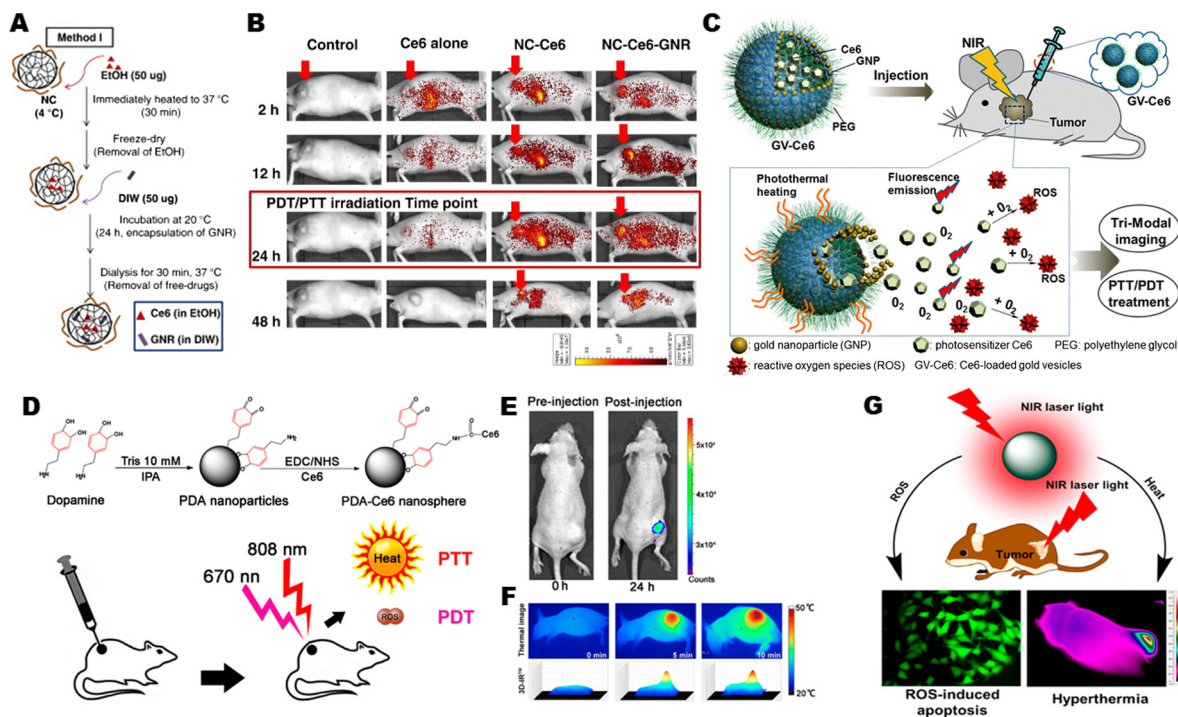
Fig. 10. Design of NIR excited PDT/PTT agents. (A) Scheme illustrating the procedure for loading the photo-agents (Ce6 and GNRs) into a Pluronic nanogel. (B) *In vivo* NIR fluorescence images of nude mice bearing SCC7 tumors after *i.v.* injection of photo-agents [431]. (C) Photosensitizer (Ce6)-loaded plasmonic gold vesicles (GVs) with trimodal (fluorescence/thermal/photoacoustic) imaging for use in photothermal/photodynamic cancer therapy [443]. (D) Schematic view of the preparation of PDA-Ce6 nanospheres for PDT and PTT treatments of HepG2 tumor-bearing nude mice. (E) *In vivo* NIR fluorescent images of HepG2 tumor-bearing nude mice 24 h after injection. (F) thermo-graphic images and 3D temperature distribution in tumor-bearing nude mice exposed to laser irradiation at 808 nm at different time points [433]. (G) A treatment scheme for the use of plasmonic copper sulfide ($Cu_{2-x}S$) nanocrystals (NCs) exhibiting both PTT and PDT capabilities [444]. Reproduced with permission [431,433,443,444].

extremely low dark toxicity [433] (Fig. 10D and E). This combined photo-therapy had high therapeutic efficiency both *in vitro* and *in vivo* compared with any single laser irradiation alone.

A non-invasive NIR therapeutic technique using combination therapy was also developed with graphene oxide as the PTT substrate followed by absorption of methylene blue as a potential photosensitizer [445]. Conjugation of Cy5.5 on the surface of the graphene oxide/MB was performed to track internalization of the particles under NIR imaging. By altering the PTT nanocore or the PS load, the following could be fabricated: gold-nanorod-PS layer-by-layer [446], sinoporphyrin sodium loaded graphene oxide [434,435], a pH-sensitive peptide inserting gold nanorod-photosensitizer conjugate [436], self-aggregation of Ce6 photo-sensitizers and gold nanorods [431,447], WS_2@BSA/MB nanosheets [437], and a ZnPc photosensitizer in a liposomal membrane decorated with a gold nanofilm [438]. Fluorescence, the PA technology, and an IR thermal camera with NIR light excitation, have been used for acquisition of both *in vitro* and *in vivo* images.

In a different approach, Vijayaraghavan et al. developed a new gold nanoechinus structure that was capable of NIR light-activated dual modal photodynamic (NIR-I and NIR-II biological window) and photo-thermal therapy (808 nm) [389]. Interestingly, the photon energy can also be converted to emit excitation wavelength-dependent fluorescence for quantification of cellular uptake, as well as quantification of cellular markers, *in vivo*. In this case, the Au nanoechinus acted as both the photon-to-thermal converting agent and the photosensitizer without the need for addition of an organic dye to produce singlet oxygen. In another enlightened study, Xu and co-workers reported the optical photon-physical and photon-chemical properties of Au nanorods [448]. Au nanorods are among the most commonly studied photo-thermal therapeutic agents that use NIR laser excitation [449]. The authors demonstrated that singlet oxygen from Au nanorods could be generated with one- or two-photon excitation. The application of two-photon excitation at 808 nm resulted in a high quantum yield of singlet oxygen, when compared with rose bengal and ICG [450,451] and this difference was ascribed to the large two-photon absorption cross-section of the molecules in the Au nanorods.

Carbon nano-dots [452], quantum dots [453,454], silica/fluorescent donors [229] and Ln-based UCNPs [455] have also been demonstrated to be excellent nano-converters for the two-photon excited energy transfer to PS on PDT treatment. These results have been widely reviewed elsewhere [456].

The current discovery of total inorganic composite nanomaterials has allowed for the dual PDT/PTT capability to be obtained with plasmonic copper sulfide ($Cu_{2-x}S$) nanocrystals [444], WO_3-x nanoparticles [457], Cd-based QDs [458–460], grapheme QDs [461–463], and Au nanorods [448]. In contrast, there are several reports on the use of the PDT/PTT platform

with organic nanocomposites, e.g., an NIR polymer and PS [433], IR825 and Ce6 in a nano-micelle [464], a human serum albumin-ICG hybrid [174], and doxorubin/ICG loaded lipid polymer nanoparticles [173]. Both infrared thermographic and NIR fluorescent maps are able to be captured and detected during the combined photo-therapeutic treatment *in situ*.

6. Nanotoxicology: concerns about the biosafety of NIR nanomaterials

The increasing number of studies and the production of numerous types of nanomaterials raises fundamental questions on their safety for use in humans and also for the environment. While classical toxicology has developed well-established tools and standards to assess the toxicity of various substances, their application to nanomaterial toxicity is problematic because these a new class of materials. Perhaps one of the most important aspects that deserves consideration is that nanomaterials have completely different physicochemical properties compared to the bulk form of the same material. Consequently, many aspects need to be taken into consideration when analyzing the impact of such materials on living organisms e.g. the fact that nanoparticles of the same material, and having the same shape but with a slightly different size may interact differently within a body thereby producing a different toxicity profile [465]. Parameters commonly accepted to be important determinants of nanoparticles toxicity are: structure, chemical composition, shape, surface composition, charge and area, redox properties, aggregation tendency, nature of the shell or coating material, chemical stability, biodegradability, as well as others [466]. Despite the growing number of studies, the mechanistic understanding of nanoparticles toxicity is still in its infancy.

With advances in the production of engineered nanomaterials and their broader applications in many aspects of life, exposure to nanoparticles has become an increasingly growing concern. Nanoparticles are extensively used in manufacturing; for example in new composite materials, protective coatings, inks, electronics, cleaning and disinfectant products, medicines, cosmetics and many other products. As a consequence, the penetration of manmade nanoparticles into the environment is inevitable.

Therefore, there is an urgent need for the introduction of reliable nanotoxicology methods that will allow for an assessment of the impact of nanoparticles on life in broad terms, including, toxicity at all levels of complexity (single cell, tissues, whole organisms), the impact on aquatic organisms, and the impact on various ecosystems. Exhaustive database on toxicology are a key part for the proper life cycle assessment of nanoparticles as products to be manufactured and used in a massive scale. This aspect, based on community expectations, should keep up with the technological progress and market needs [467].

Living organisms have evolved a number of adaptations to nanoparticles that naturally occur in the environment, however newly-fabricated materials present unique properties to which organisms have yet to adapt, and therefore they may become a serious health challenge.

Many studies have been conducted on the health effects of exposure to nanoparticles present as common pollutants, including airborne pollutants arising from the burning of carbon fuels and natural materials.

Ongoing discussions raise questions concerning their associated health hazards, the balance between benefits and threats, and on safe handling procedures. The Organization for Economic Cooperation and Development (OECD) has recently suggested a critical revision of currently employed methods for analysis of materials safety to specifically address man-made nanoparticles [468].

The implementation of new analytical methods may highlight so far undiscovered facts concerning the property of nanomaterials. For instance, some studies have shown that titanium dioxide and zinc oxide nanoparticles, although already recognized as safe, can under certain specific conditions be toxic to the human brain and lung cells [469–471].

6.1. Methods to analyze the toxicology of NIR nanomaterials

The number of available research models and methods for the nanotoxicity is constantly growing, enriching our database on the impact of nanomaterials in living systems.

The most commonly applied approach for the initial estimation of potential nanoparticle toxicity is based on *in vitro* studies using various cell lines. Living cells in a cell culture are treated with test materials and after a certain time (usually from a few to 24–48 h) their viability, morphology, ability to proliferate, as well as other parameters are analyzed. Viability and morphology can be studied directly using microcopy, or can be estimated in a more quantitative way using one of the many viability assays that are currently available on the market (MTT, MTS, XTT, WST-1, CCK-8, Resazurin viability assay, etc.). In general, their principle mechanism of action is the formation of colored or fluorescent compounds in the presence of active mitochondrial enzymes [472–474]. Other popular assays include, the lactate dehydrogenase (LDH) release assay, a test indicative of an effect on cell membrane integrity associated with the release of the cytosolic enzyme LDH from cells [475]; tests for ROS (reactive oxygen species) that allow analysis of the formation of ROS as a result of oxidative stress [476]; measurement of apoptosis markers (for e.g. the Annexin V test) that are used to observe whether the tested material has the ability to induce programmed cell death [477]. More complex studies can include immunohistochemistry or analysis of inflammatory cytokines released by cells treated with substances having pro-inflammatory activities. These types of tests involve ELISAs, quantitative real-time PCR, or flow cytometry [478].

The proliferation potential of cells can be easily estimated via thymidine incorporation assays (e.g. the older radionuclide incorporation assay or modern methods developed for flow cytometers) [479].

Information on the impact of nanomaterials on cellular genetic material (genotoxicity) can be gained using the simple and sensitive Comet Assay. In this assay DNA obtained from lysed cells embedded in agarose is subjected to electrophoresis at high pH resulting in structures resembling a comet when observed under a fluorescent microscope. The extent of the "comet tail" reflects the number of DNA breaks. This method allows for analysis of DNA breakage at a single cell level [480].

In vitro techniques are usually the methods of choice for most researchers during "proof of concept" or initial toxicology studies, and they can provide valuable data with relatively low cost and effort, and the necessary resources are usually available in standard research laboratories.

However, it must be considered that the data obtained from *in vitro* studies carries a significant level of uncertainty due to many constraints. First of all, most studies are performed on models, specifically cell lines, that are generally transformed, immortalized cells, and thus their function and responses to compounds may differ to some extent from normal cells. Normal cells have for example limited proliferative potential in comparison to cell lines. Cells in culture dishes function in an isolated surrounding; all of the complexity of interactions between cells in tissues, organs, and the whole body are missed from this analysis meaning that the results obtained may differ significantly from the real-life situation. To support this notion, one example can be given: it is well know that bacterial endotoxin (LPS) exerts it full toxic potential at the whole body level whereas at the cellular level cytotoxicity is lower and is restricted to certain cell types [481,482].

The potency of LPS relates to its ability to strongly stimulate the release of inflammatory cytokines by immune cells, overstimulation leads to the damage of vital organs and death, therefore an indirect mechanism is responsible for the toxic effect of LPS at the whole body level. Similarly, a lack of noticeable cytotoxicity of a nanomaterial in *in vitro* studies may not necessarily reflect the same at the whole organism level. On the other hand, it is much more probable that a compound demonstrating toxic effects in *in vitro* models will be toxic when applied to a body than vice versa.

New models for *in vitro* studies are continually being sought, e.g. pluripotent stem cells [483], in order to improve the predictive value of the data obtained.

Other difficulties noticed by many researchers are that interactions of certain new nanomaterials with components of assays can significantly affect measured values, as has been specifically noted for carbon-based nanomaterials [206]. The use of novel instrumentation that utilize microelectronic sensing devices capable of assessing cell viability and as well as other cell parameters may help to resolve the issue [484].

Toxicity studies conducted in models with higher levels of complexity, typically *in vivo* models, will cover many other parameters and can examine the effects of mutual complex interactions between diverse types of cells, tissues and organs within a body. The models provide more comprehensive toxicological data, but at significantly higher costs, and the technical complexity of the research, including ethical issues that are associated with animal studies are an additional burden.

Although there are several toxicology models based on invertebrate organisms, including *Caenorhabditis elegans*, *Drosophila melanogaster* [485] and others, the most popular models remain laboratory rodents (mice, rats, rabbits). Study on these common laboratory animals allow the investigation of more aspects of toxicity including bio-distribution, accumulation, excretion, and metabolisms following changes in dose and routes of administration.

Recent reports have also proposed the use of zebrafish as a versatile animal model to assess nanoparticle toxicity in a broad range of aspects including: acute toxicity, immunotoxicity, genotoxicity and gene expression, neurotoxicity, impact on fertility, etc. Significant advantages of this model include ease of handling, small size, high reproducibility, fast development and transparency of the embryo.

Different research methodologies are used to study toxicity in animal models. Following administration of a test substance, animals are monitored for symptoms of toxicity and adverse effects including death, diarrhea, lethargy, depression, suppression of movement, skin and eye irritation, swelling, depressed water and food uptake, and behavioral changes [486].

Depending on the study design, many biochemical and physical parameter can be tested using blood, urine, and feces sampling. Commonly, these biochemical markers, as well as hematological blood parameters (e.g. WBC – white blood cells count) are used as markers of health status. Furthermore, liver and kidney function can be monitored indirectly, as those organs play key roles in detoxification, excretion, and accumulation of foreign materials. In the case of an end point study, animals are euthanized and subjected to histological analysis of tissues and organs. Studies examining the effects of chronic exposure at low doses, impacts on genetic material, and fertility impact usually require long-term experiments and careful experimental design.

Recent reports have presented new interesting ideas to study nanotoxicity that may open new possibilities for the field. For example, Ivask et al. demonstrated a genomic approach to assess the different toxicities of different forms of a nanomaterial [487].

There have also been attempts to develop computational methodologies for the analysis of quantitative structure-activity relationships (QSARs). This technique might help to predict toxicity of nanoparticles based on correlation with specific parameters like size, shapes, coating, and porosity [488].

6.2. Toxicity of NIR nanomaterials

Several comprehensive review articles discussing the toxicity of engineered nanoparticles have been recently published, where quantum dots, gold, iron oxide nanoparticles [489], or lanthanide doped nanoparticles [490] were compared, and the influences of nanoparticle shape, size, and surface functionalization on cellular uptake were described [491,492].

Data on the toxicity of NIR materials are still scarce because these materials are relatively new to the field so there has been insufficient time to obtain enough data for conclusions to be drawn. Certainly, a long-term and systematic study is needed to draw reliable conclusions concerning the safety of these materials. So far, some features can be anticipated, based on comparison to known characteristics of other nanoparticles formed from analogous bulk materials.

An important notion is that most elements or materials employed for the formation of NIR nanoparticles (see Table 1) are not toxic in the bulk form, therefore eventual toxicity may be attributed to the nanoparticle form. Apparent toxicity applies to such elements like cadmium ions (in Cd based QDs), silver, other noble metals, and fluoride ions (in UCNPs).

NIR materials based on Au are probably the best characterized in terms of physical properties and biocompatibility [5,493]. In general, most spherical forms of AuNPs show little or no toxicity apart from particles with some specific sizes e.g. a nanoparticle with diameter of 1.4 nm that fits into the DNA major groove had increased toxicity [494]. It should be remembered that the surface coating strongly affects the properties of AuNPs including their bio-distribution and toxicity. Gold-based NIR materials are mainly represented by: nanorods, nanoshells and nanocages. Gold nanorods exert slightly higher toxicity than spherical particles; but this can be reduced by replacing hexadecyltrimethylammonium bromide (CTAB), a surfactant necessary for the synthesis of nanorods, with phosphatidylcholine, for example [495]. Gold nanoshells and nanocages, have been studied less extensively but so far no serious toxicity problems have been observed [331,496].

Noble metal NIR materials such as Pd nanosheets (<10 nm diameter), when formulated with glutathione, showed prolonged blood circulation, good accumulation in tumors, with no apparent toxicity in mice and were renally cleared [497]. Other recently developed materials such as WS_2 nanosheets, MoS_2 nanosheets also showed good stability and biocompatibility [498–500].

However, some intrinsic toxicity was observed for CuTe nanoparticles. However, further work using better encapsulation or more strictly controlled administration were suggested as being effective at addressing this problem [501].

Iron oxide nanoparticles possesses unique and useful properties and have been widely used in the biomedical field, as they are considered as safe and biocompatible [502]. Polypyrrole (PPY) NPs are another recently developed material with very promising features including photostability and a low synthesis cost. They have been studied for suitability as a photo-thermal cancer therapy with outstanding results both *in vitro* and *in vivo* [503,504].

Carbon-based nanomaterials have recently gained significant interest due to their spectacular properties and potential application in many fields. As of now, they will certainly take a leading position among the nanomaterials produced in high quantity. However, possible environment release and chronic exposure create safety concerns. A constantly growing number of reports predict that their application in nanomedicine will also be substantial. Studies *in vitro* and *in vivo* models have shown that some forms of graphene family nanoparticles showed toxic properties that were strongly dependent on dose, size, surface shape, chemistry, etc.; these reports are extensively discussed elsewhere [505].

Given that production and application of nanomaterials is a relatively recent achievement, nanotoxicology is therefore an emerging field and will have to solve problems that so far have not been encountered in classical toxicology. Nanoparticles have may complex features including size, shape, charge, coating and changes in these features may produce very different toxic effects. In addition, route of administration and factors such nanoparticle degradation, metabolism, adsorption to other molecules, and adsorption to tissues may all affect their toxicity profile.

These factors therefore create an enormous number of variables that have to be considered and analyzed during toxicology studies. The question that is raised is how to establish reliable standardized protocols for such studies. Although this question remains to be answered, it is widely recognized across the scientific community.

The evaluation of the safety of nanoparticle-based drugs or medical products also has the problem of extrapolating from *in vitro* and *in vivo* studies to the real-world clinical situation. For example, the doses used in toxicity studies are usually much higher than those generally required in routine clinical use as diagnostics or treatments, so the available data may not be relevant. Another problem is that most data is generated using short-term exposure experiments whereas long-term studies are necessary to really assess the effect of chronic exposure to NPs, including the effects of NPs that have accumulated in organs over time.

In conclusion, the existing data allow us to propose several new NIR materials, with no apparent toxicity, as candidates for medical applications. However, a final conclusion on biosafety will be possible only after thorough, detailed, studies (including clinical stage) have been conducted, and these data will have to apply to a particular product than a class of nanomaterials.

6.3. Regulatory issues on nanomaterials

Despite the fact that nanoparticle properties are rarely seen in their bulk counterparts and show promise in many alternative and new bio-medical applications, such as bio-sensing and bio-imaging, the toxic effect is very difficult to predict based solely on chemical composition. This issue originates from a number of factors, including surface chemistry (mostly related to charge) and surface to volume ratio, nanoparticle size, the nanoparticle's shape anisotropy, chemical composition, and susceptibility to dissolution in organic media, which all have been shown to affect their cytotoxicity to some degree. In general, nanomaterials are more chemically active and behave in different ways compared to their bulk component chemicals. They are also more likely to be taken up by humans and animals, through the skin, and lungs, and through food ingestion [490] and may then accumulate in different organs (liver, spleen, lungs, etc.). Moreover, the quantification of nanotoxicity at the cellular level *in vitro*, is not relevant for extrapolation of *in vivo* nanotoxicity. A simple example, which

Table 1
Overview of the toxicity aspects associated with NIR nanomaterials.

Material	Coating	Size	Research model	Dose/concentration	Treatment time	Results	Ref.
Metallic and metallic compound-based nanoparticles							
Au nanorods	Chitosan oligosaccharide lactate/chitosan anti anti-EGFR Ab	47 ± 3 nm/11 ± 1.8 nm	Oral adenosquamous carcinoma cell line CAL 27	1–200 µg/mL	72 h	Viability: 90–100%	[329]
			Male 6-week-old BALB/c nude mice	100 µg/i.v. injection	7 days	No significant changes in histology, hematological, and clinical biochemistry parameters apart from slight reduction of RBC count	
Au nanorods	PEG	65 ± 5 nm/11 ± 1 nm	HeLa cells	0.5 mM/Au atom	24 h	Viability: 90%	[330]
Silica core Au nanoshells	SH-PEG	55-nm core radius and a 10-nm-thick	Human breast epithelial carcinoma SK-BR-3 cells	4.4×10^9 particles per mL	3 h	No cell death (microscopy observation)	[331]
Porous hollow Au nanoparticles	Bare or SH-PEG coated	150 nm	Prostate cancer cell line (PC-3), human breast carcinoma cell line (MDA-MB-231), lung-metastasized prostate cancer cells (PC-3ML)	0.8, 4, 20, and 100 µM	24 and 72 h	Both types non-toxic in all concentrations, observed some growth inhibition of PC-3, PNT1A, and MDAMB231 cells at higher concentrations, and growth enhancement in PC3-ML cells after 72 h	[332]
Silica core Au nanoshells	–	30 nm core/shell thickness of 5–10 nm	Prostate cancer cell lines, LNCaP and PC3	4×10^{12} particles/mL	24 h	No toxicity detected (MTT assay)	[333]
Silica core Au nanoshells	Anti-HER2 or a nonspecific antibody (anti-IgG)	120 nm core/10 nm shell	SKBr3 breast adenocarcinoma cells	3×10^9 nanoshells/mL	From 1 h	No toxicity detected (calcein fluorescence)	[334]
Au nanocages	PEG-anti-EGFR Ab or PEG	50 ± 3 nm and wall thickness of 5 ± 1.2 nm	U87MGwtEGFR cells	0.02 nM	Up to 24 h	No toxicity observed (microscopy)	[335]
Au nanocages	Peg 5000	33 nm in edge length	Mice bearing EMT-6 tumors	1.7×10^{12} particle/mouse	1, 6, and 24 h	No signs of toxicity observed (behavioral observations)	[336]
Pd nanosheets	Reduced glutathione (GSH)	4.4 nm	Mice	400 µg/mouse	40 days	No sign of toxic side effects within 40 days. Neither death nor significant body weight drop. No noticeable signal of organ damage	[497]
Pd nanosheets	Doxorubicne/reduced glutathione	4.4 nm	Mice	300 µg/mouse	40 days	No changes in major organs (histological examinations)	[337]
Pd nanosheets	No coating	16 nm	Immunodeficient nude mice	160 µg/mouse	7 days	No changes in histological image of major organs	[338]
WS$_2$ nanosheets	PEG coated and no coated	1.1 nm thickness/50–100 nm diameter	Murine breast cancer cells (4T1), HeLa, human embryo kidney cells (293T)	0.1 mg/mL	24 h	No toxicity detected (MTT assay) for PEGylated particles, non-PEGylated were toxic at high conc.	[498]
WS$_2$ nanosheets	BSA	Average thickness 1.6 nm/diameters of 20–100 nm	HeLa	Up to 0.2 mg/mL	24 h	Viability: >80%	[437]
MoS$_2$ nanosheets	PEG, loaded with chlorin e6 (Ce6)	Thickness ~1 nm	Mice bearing 4T1 tumors	6.85 mg/kg	20 days	No significant side effects in major organs (histological study)	[499]
MoS$_2$ nanosheets	PEG	Thickness 0.29 nm/80 diameter; thickness 0.39 nm/103 nm dimeter	4T1 cells L929 cells	200 µg/mL	24 h	No significant cytotoxicity was observed (CCK-8 assay, morphology)	[500]
			BALB/c nude mice	200 µg/mouse	Up to 40 days	No changes observed in major organs	

Table 1 (continued)

Material	Coating	Size	Research model	Dose/concentration	Treatment time	Results	Ref.
						(histological examination)	
CuS	PEG	11 nm	U87 glioblastoma cells	500 µM	26 h	No apparent change in cell viability (microscopy)	[506]
Graphene oxide/CuS nanocomposite	PEG	13 nm	HeLa cells	500 µg/mL	24 h	Viability >90% (MTT assay)	[507]
FeS nanoplates	PEG	32–36 nm	BALB/c mice	100 mg/kg	1, 7 and 50 days	No changes in biochemical parameters of blood, kidney, liver, no changes observed in major organs (histological examination)	[508]
Ag$_2$S QDs	PEG	5.4 nm	BALB/c mice	15 and 30 mg/kg	Up to 60 days	No interference on the mice growth, blood biochemistry not changed after 60 days, transiently elevated AST value, drop in platelet and WBC counts at the first few days (normal level after 14 days)	[328]
ZnS:Mn/ZnS core/shell nanoparticles	Mercaptopropionic acid/folic acid	8.0 nm	HeLa cells	0–400 mg/mL	6 h or 24 h	Viability: about 90% at highest dose	[509]
CuTe NP	Poly(isobutylene-alt-maleic anhydride)	10–20 nm	3T3 embryonic fibroblasts	75 nM	3 h	Certain toxicity was visible (DAPI labeling)	[501]
Cs$_x$WO$_3$ nanorod	PEG	Diameter ~11 nm, length ~50 nm	HeLa	0.5 mg/mL	24 h	Viability >90%	[392]
Tungsten oxide nanorods	PEG	Diameter of 4.4 ± 1.5 nm, length of 13.1 ± 3.6 nm	HeLa cells L929 cells	Up to 1000 µg/mL	12 or 24 h	Viability – 80% up to conc. 500 µg/mL, decrease in viability at higher concentrations	[400]
W$_{18}$O$_{49}$ nanowires	PEG	Length of 80–400 nm, thickness 0.9 nm	HeLa cells	0.25–3.0 mg/mL	24 h	No significant differences in the cell proliferation, viability greater than 90% (MTT assay)	[393]
W$_{18}$O$_{49}$ nanoparticles	Anti-HER-2 monoclonal antibody	4.5 nm mean diameter	Human alveolar basal epithelial cell line A549	Up to 5 mg/mL	28 and 52 h	Decrease 16.8% in viability for the highest concentration 5 mg/mL	[394]
Na$_{0.3}$WO$_3$ nanorods	PEG	Diameter ~5 nm, length 39 nm	TC71 tumor cells	Up to 1 mg/mL	24 h	Viability 98.9% at 0.5 mg/mL and over 80% for 1.0 mg/mL	[510]
BaTiO$_3$ nanoparticles	Glycol-chitosan	285 nm	Human neuroblastoma SH-SY5Y cell line	0, 5, 10, 20, 50 and 100 µg/mL	48–52 h	Viability 90% (MTT assay) no membrane damage (live/dead viability/cytotoxicity test), absence of apoptosis (Annexin V test), not detectible oxidative stress signs	[511]
KTiOPO$_4$ nanocrystals	Bare	80 nm	Cortical neurons from mouse embryonic brain	Not reported	30 min exposure to NP, 2–4 days culture	Dendritic growth of cortical neurons not affected	[512]
CdTe QDs CdTe/CdS CdTe/CdS/ZnS core–shell–shell quantum dots	Bare	2.15 ± 0.26 nm 3.01 ± 0.42 nm 4.22 ± 0.52 nm (core sizes), 3.01 and 4.22 nm for core/shell NPs	HeLa	Up to 300 nM	24 h	CdTe-cytotoxic (even at lower conc. – 75 nM), core-shell CdTe/CdS QDs less toxic, viability ~80% at conc. 300 nM, lowest toxicity for CdTe/CdS/ZnS QDs – ~100% at conc. 300 nM	[513]

Carbon based nanomaterials

Table 1 (*continued*)

Material	Coating	Size	Research model	Dose/concentration	Treatment time	Results	Ref.
Nanodiamonds	–	2–10 nm	Kun Ming mice	0.8 mg/kg, 4 mg/kg, 20 mg/kg body weight (intra-tracheal instillation)	3 days	Lung toxicity observed (histopathological examination), changes in biochemical parameters of BAL fluid, kidney, liver and blood	[514]
	CM-dextran or BSA	~120 nm	*Caenorhabditis elegans*	1 mg/mL	3 h up to a few days	No change in longevity and reproductive potential, no symptoms of detectable stress to the organism	[515]
Single-walled carbon nanotubes	Mouse (anti-human CD22) IgG	Length 0.2–1.4 µm (average of 0.59 µm)	Burkitt's lymphoma cell line (Daudi cells)	3.6 µg	24 h	No toxicity observed ([3H]thymidine incorporation assay)	[516]
Single-walled carbon nanotubes	PEG (covalently bound)	300 nm to a micrometer	Male KM mice, BALB/c mice bearing EMF6 tumor and C57BL mice bearing Lewis tumor	2.4 mg/kg body weight	1 h, 1 day, 3 days and 7 days	No signs of acute toxicological responses or clinical abnormalities	[517]
Single-walled carbon nanotubes	Bare	Diameter of ca. 1.4 nm and a mean length of ca. 1 µm	Alveolar macrophages from guinea pigs	1.41, 2.82, 5.65, 11.30, 28.20, 56.50, 113.00, and 226.00 µg/cm^2	6 h	Significant, dose dependent toxicity	[518]
Graphene QDs	PEG	3–5 nm	HeLa, A549	10, 20, 40, 80 and 160, 320, and 640 µg/mL	24 h	95% viability at conc. 160 µg/mL, 85% at 640 µg/mL, negligible apoptosis or necrosis, no signs of oxidative stress or membrane damage	[519]
			BALB/c mice	20 mg/kg (7 injections)	40 days	No difference in major organs in comparison to controls, hematological markers not changed apart lower WBC (however still within a normal range), blood biochemical markers not changed	
Carbon nanodots	Bare PEI PEG	4–7 nm	NIH/3T3	5–400 µg/mL	24 h	Dose and charge dependent toxicity, negatively charged (PEI) highest tox. IC50 ~ 5 µg/mL low tox. for PEG coated CDs	[520]
Carbon nanodots	–	2–6 nm	CHHO-K1 COS-7 HeLa	0–10 mg/mL	24 h	No apparent toxicity at dose up to 5 mg/mL, dose dependent, low tox. at higher conc.	[521]
Carbon nanodots	–	2–6 nm	HepG2 cells	0.1–1 mg/mL	24 h	Cell viability 90–100% (MTT assay)	[522]
Graphene oxide nanosheets and reduced graphene oxide nanosheets	PEG	Mean of ~18.8 nm	U87MG, MCF-7 human epithelial breast cancer cells	Up to 1 mg/mL	48 h	Dose dependent toxicity observed: IC$_{50}$ of ~80 µg/mL (nano-rGO) and IC$_{50}$ of ~99 µg/mL for nano-GO	[523]
Graphene nanoplates intercalated with manganese	–	Diameter – 200 nm and 3 nm thickness,	NIH3T3 mouse fibroblasts, A498 (human kidney epithelial cells)	1–500 µg/mL	24 and 48 h	Dose dependent toxicity observed: IC$_{50}$ range 179–301 µg/ml (LDH and calcein-AM assay)	[524]
Other materials							
Mn-doped Si QDs	Dextran or dextran sulfate	4.3 ± 1.0 nm	P388D1 cells, mouse embryonic fibroblast NIH 3T3 cells	0.65, 1.31, 2.61, 5.22, and 10.45 mg/well and 0.64, 1.27, 2.55, 5.10, and 10.20 mg/well	24 h	Resazurin viability assay viability – 90% (P388D1 cells) and 97% (NIH 3T3 cells)	[525]
Polypyrrole nanoparticles	–	Average size of ~50 ± 5 nm	BALB/c mice	10 mg/kg	60 days	No changes observed in major organs (histological examination)	[503]
Polypyrrole nanoparticles	–	46 nm	Hela cells	300 µg/mL	12 h	Viability ~90%	[504]

demonstrates the level of complexity in nanotoxicity studies relates to the definition of dose of nanoparticle-based compounds. Should the mass of the NPs, their total number, or the surface area per unit volume be considered as the dose? These issues and question are in stark contrast to definition of toxicity based purely on chemical composition, making nanotoxicity studies using conventional methods unreliable and questionable. The European Commission's Scientific Committee on Emerging and Newly Identified Health Risks (SCENIHR) noted that "experts are of the unanimous opinion that the adverse effects of nanoparticles cannot be predicted (or derived) from the known toxicity of material of macroscopic size, which obey the laws of classical physics" (please refer to the European Commission's Scientific Committee on Emerging and Newly Identified Health Risks (SCENIHR) for a more detailed discussion concerning the appropriateness of existing methodologies to assess the potential risks associated with nanotechnologies). Similarly, the U.K. Royal Society and the Royal Academy of Engineering emphasized, "Free particles in the nanometre size range do raise health, environmental, and safety concerns, and their toxicology cannot be inferred from that of particles of the same chemical at a larger size" (please see the report from Royal Society of Engineering on 'Nanoscience and nanotechnologies: Opportunities and uncertainties'). Furthermore, the Institute of Occupational Medicine notes, "Because of their size and the ways they are used, they have specific physical-chemical properties and therefore may behave differently from their parent materials when released and interact differently with living systems. It is accepted, therefore, that it is not possible to infer the safety of nanomaterials by using information derived from the bulk parent material" [526].

There are some arguments against developing specialized regulations for nanotechnology products. This is because the existing methods exploit the most advanced available scientific methodologies to assess risks and safety, and they have been successful in identifying dangerous or unacceptable materials or products. Rather than creating a dedicated regulation based on size, it is postulated to treat particle size as one of the several parameters which define a substance to be approved. Another argument against global regulation originates from the fact that nanotechnology applications are often hypothetical with the strongest impact far in the future, thus regulating such futuristic technologies is vague. At the same time, the nano-materials and products based on them, are not much more challenging than any other new materials. Therefore, a minor tuning to already existing regulatory schemes is faster and more feasible than introducing global regulations [527].

The regulatory agencies of the European Union, the United States and Australia agree on the accurateness of existing regulations with respect to nanotoxicity, however numerous initiatives are being considered at the national and international level to decide whether additional studies are necessary. Some preliminary approaches to understand the role, and potential pitfalls of nanotechnology, were initiated in Europe in 2004, when a warning about the necessity of addressing any potential negative impacts of nanoparticles on public health, safety, and the environment were articulated (please see the report from the Commission of the European Communities, Communication from The Commission, Towards a European strategy for Nanotechnology, 2004). The expected future impact of nanotechnology on the quality of life, materials sciences, healthcare, information technology, and the environment has been acknowledged much earlier by many countries including the USA, Japan, Europe, China, and Russia. At that early time, the potential advantages of nanotechnology dominated the potential risks associated with the extensive production and use of nanomaterials. Eight years later, in 2011, the European Commission announced and adopted a definition of nanomaterials [528]. Existing knowledge concerning nanomaterials was summarized in 2012 in the Commission Communication on the Second Regulatory Review. At that time, carbon black and amorphous silica were the most predominant nanomaterials in the market-place but new nanomaterials, such as nano-titanium dioxide, nano-zinc oxide, fullerenes, carbon nanotubes, and nanosilver were fast gaining interest for use in new applications such as in catalysts, electronics, solar panels, batteries and in the biomedical field. The communication concluded (please see communication from the Commission to The European Parliament, The Council And The European Economic And Social Committee, Second Regulatory Review on Nanomaterials, 2012), that although nanomaterials "are similar to normal chemicals/substances in that, some may be toxic and some may not", possible risks are actually related to a given nanomaterial for a specific application, therefore the risk assessment shall be examined on a case-by-case basis. Despite the fact that current toxicity assessment methods have been found applicable to nanomaterials, continuing work on particular aspects of risk assessment was expected and the EU Commission advised modification of the Registration, Evaluation, Authorisation and restriction of CHemicals (REACH) Annexes and further development of guidance for registration of new (nanotechnology based) chemicals after 2013. Similar to REACH, the Scientific Committee on Emerging and Newly Identified Health Risks (SCENIHR) stated that while the existing toxicological and eco-toxicological methods are applicable to quantify and estimate many of the threats linked to the production and exploitation of nanoparticles, these methods may not be sufficient to address all of the hazards (please see Scientific Committee on Emerging And Newly Identified Health Risks (SCENIHR), Opinion on The appropriateness of existing methodologies to assess the potential risks associated with engineered and adventitious products of nanotechnologies, 2005). It should be noted, that many European countries (the German Federal Institute for Risk Assessment; the Department for Environment, Food and Rural Affairs (DEFRA) in the United Kingdom; the French Ministry of Ecology, Sustainable Development and Energy; the Danish Consumer Council and the Danish Ecological Council in cooperation with Technical University of Demark; the Netherlands National Institute for Public Health and the Environment-RIVM, as well as others) have developed their own regulations and guidelines, which more precisely described how approvals, labeling, reporting, or communication with REACH shall be performed when it comes to new products which involve nanomaterials [529].

In the USA, the advantages and industrial applications of nanomaterials have also been exploited before risk assessment methods had been developed and nanotoxicity had been understood. In 2007, the United States Food and Drug administration stated that it does not see the need to develop any regulatory definition of nanomaterials and nanotoxicology (please see the

Nanotechnology Task Force Report). However, in response to growing interest and commercial exploitation of nanomaterial products on the market, FDA decided to issue preliminary guidelines in 2011 (please see draft guidance: Considering Whether an FDA-Regulated Product Involves the Application of Nanotechnology) to indicate whether a product, which is a subject to FDA approval, contains any nanomaterials or involves nanotechnology products. The following year, more details were provided with respect to the food and cosmetic industries, which involved the use of nanomaterials (please see FDA Draft Guidance for Industry: Assessing the Effects of Significant Manufacturing Process Changes, including Emerging Technologies, on the Safety and Regulatory Status of Food Ingredients and Food Contact Substances, Including Food Ingredients that are Color Additives). Unlike in Europe, the FDA concluded in 2012, that safety assessment methods existing in the USA, are satisfactory for a variety of materials including nanomaterials. In 2001 a National Nanotechnology Initiative (NNI, www.nano.gov) was established as a response to the natural shift from the fundamental studies on the synthesis and characterization of nanomaterials towards exploiting nanotechnology-enabled products (e.g. in electronics, clean energy technologies, clothing and fabrics, car industry, the biomedical and drug market, etc.). Between 2009 and 2016, the US revenue from the sale of nanotechnology-based products increased over sixfold to reach ca. 500 billion US dollars. The most recent NNI Strategic Plan was issued in October 2016. The document discusses: (i) advancing a world-class nanotechnology R&D program, (ii) fostering the transfer of new nano-technologies into products for commercial and public products, (iii) developing and sustaining educational resources to advance nanotechnology and (iv) support responsible development of nanotechnologies. In the mean-time the US Environment Protection Agency (EPA) released numerous nanotechnology white papers (like EPA 100/B-07/001, February 2007), underlining the necessity to control and monitor the production of nanotechnology containing products. Recently the EPA has issued a final version of its rules, which oblige manufacturers to report manufactured or processed nanoparticles, which, as defined in Section 3 of Toxic Substances Control Act (TSCA), are solids at 25 °C and standard atmospheric pressure; are manufactured or processed in a form where any particles, including aggregates and agglomerates, are in the size range of 1–100 nm (nm) in at least one dimension; and are manufactured or processed to exhibit one or more unique and novel properties. This 'definition' of nanomaterial differs from the EU definition, which states that nanomaterial 'means a natural, incidental, or manufactured material containing particles, in an unbound state, or as an aggregate or as an agglomerate, where, for 50% or more of the particles in the size number distribution, one or more of the external dimensions is in the size range of 1–100 nm. The EPA rule does not apply to chemical substances manufactured or processed in forms that contain less than 1% by weight of any particles, including aggregates and agglomerates, in the size range of 1–100 nm. It is important to mention that according to the EPA, 'unique and novel properties' means the reportable chemical substances are not just compounds containing nanoparticles (size 1–100 nm), but they must also demonstrate a size-dependent property different from the properties of the material at sizes greater than 100 nm, which is actually the purpose that the chemical was manufactured or processed to have that form or size.

The situation in Australia is similar to that in the USA. A National Nanotechnology Strategy has been developed (please see the report from Australian Government, Approach to the Responsible Management of Nanotechnology). A 2008 review of Australia's regulatory framework (see a Review of Possible Impacts of Nanotechnology on Australia's Regulatory Framework Final Report September 2007) concluded that there were significant regulatory legal gaps that should be addressed. Even though it was obvious nanomaterials behave differently to bulk forms of the substance, most regulators (National Industrial Chemicals Notification and Assessment Scheme, Department of Environment or Therapeutic Goods Association) do not require a separate risk assessment of nanoforms of existing substances.

7. Current challenges and future perspectives

7.1. Sensitivity and background interference

The decreased light absorption of water, pigments, and fluorescent proteins provides an optimal signal-to-background ratio for NIR optical imaging, which makes it easy to capture/generate images and thermal signals up to a distance of a few millimeters [530]. However, non-negligible red to NIR auto-fluorescence from hemoglobin, melanin, lipids, and other endogenous fluorophores, may still be multi-photon excited by NIR femtosecond lasers [531]. Auto-fluorescence in the visible wavelengths is an important issue because it interferes with signal detection *in vivo* [532]. These auto-fluorescence signals will mask the desired signal and severely limit the target-to-background ratios [533]. For example, the commercially available Cy5.5 molecule has excitation/emission at 675 nm/694 nm which can be applied for molecular imaging in tracing. To avoid the absorption and scattering at short wavelengths and the elevated water absorption over 950 nm, imaging based on an NIR multi-photon process can yield the deepest tissue penetration, with improved resolution, the highest sensitivity, and with minimal photodamage/photobleaching (Fig. 11) [534]. Although NIR excitation can greatly suppress auto-fluorescence, it still has a major limitation in the lack of a suitable scale-up synthesis method for the production of biocompatible, large absorption cross-sections, high quantum efficiency, multiphoton, imaging nanoprobes.

Another strategy for improving sensitivity is by designing target-specific substances conjugated to NIR materials. The surface groups would help find the disease tissue and/or sense the targeting area. The substantial accumulation and internalization of desired particles would therefore be expected to locally increase signal generation. Additionally, in order to be an effective treatment at focused sites in solid tumors, the accumulation of the treatment in a very small area will prevent
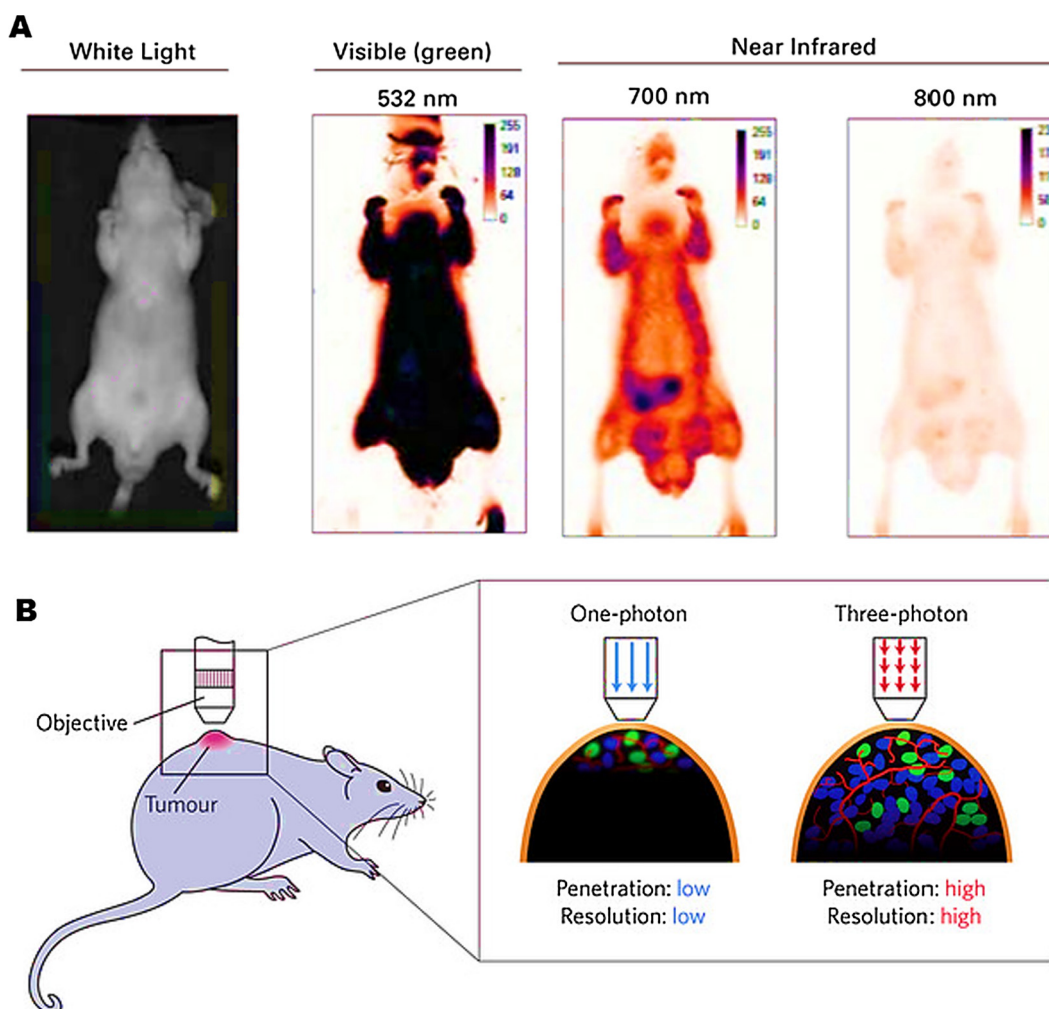
Fig. 11. (A) Tissue auto-fluorescence is much lower at NIR wavelengths. An untreated nude mouse was imaged with visible (532 nm) and NIR (700 nm or 800 nm) light. Auto-fluorescence at 532 nm (the Cy3 channel) was very high [532]. (B) A schematic showing how a tumor can be imaged directly through the skin in a live animal. The optical imaging modality (that is, one- or three-photon) and properties of the probes will determine the imaging penetration depth and resolution. If multiple tissue components are labeled with different color dyes, it is possible to image them simultaneously [534]. Reproduced with permission [532,534].

injury to the surrounding tissue. Indeed, targeting substances using a small peptide, DNA or an antibody can increase the binding selectivity in many pre-clinical and clinical studies [535,536].

Current studies have moved to further understand the molecular mechanisms for the motion, apoptosis, and necrosis of living cells in response to light [401,537–539]. In addition to the effect on cell migration, these reports also describe a pro-inflammatory response whereby pro-inflammatory cytokines are released into the extracellular milieu. These results have educated researchers and doctors to be more careful, by using the appropriate laser wavelengths, power density, and drug doses, in procedures aimed at disease healing, restoration and ablation.

7.2. Technical hurdles and potential solutions

In the clinic, therapeutic and surgical lasers commonly use He-Ne, Nd:YAG, and CO_2 lasers in the red-to-IR wavelengths. These laser systems traditionally require high-cost pump lasers. However, the laser power supply pumps even more energy in a very short time into the living system, which results in the generation of hot plasma and evaporation and damages the healthy tissue in addition to the tissue of interest. Therefore, the operation power needs to be lower than 250–670 mW/cm^2 to avoid a thermal effect that would otherwise damage the tissues [540].

Among the f-block, d-block, defect-related nanoparticles and organic dye donor–acceptor pair hybrid, lanthanide-doped UCNPs are a major focus of current research aimed at achieving better spatial and higher resolution optical imaging. Their advantage is the utility of low power ($\sim 10^{-1}$ W/cm^2) and the use of low cost CW laser diodes to generate upconverted

photons, which is in contrast with the high power density excitation (10^6 W/cm^2) needed with an expensive NIR ultrafast pulsed laser in nonlinear optical processes [140]. Early work focused on broad applications in biomedicine using different single solid nanocores and core-shell nanostrucutures with specific surface properties [84,140,321,541–543].

Size-dependent QDs have a multicolor tracking capacity and have been used to monitor multiple antibody labeling of cells *in vitro* and nanomedicine distribution *in vivo*. However, they suffer from toxicity to tissues *in vivo*. Therefore, there is an urgent need to replace the traditional toxic QD with new optical nano-reagents. A series of UCNPs with different Ln dopants had NIR-to-visible emission compatible with use as optical bio-probes. With adjustments in the Y/Yb/Er ratio, Ln-doped NaYF$_4$ UCNPs were created that exhibited different color emission peaks of blue, green, and red, as reported by Liu and co-workers [544]. These molecules provided a new insight into the multicolor tracking required for lymph node mapping. Compared to conventional QDs [82], they are less toxic to tissues. In addition, by tuning the ratio of the Ln dopants, and excitation with different laser wavelengths, a shift in the color of Ln-based UCNPs was observed. Yao and co-workers have reported a new polymer nanocomposites that consisted of poly-trimethylolpropane trimethacrylate as a polymer matrix and lanthanide orthophosphate:Tb NPs as the non-linear chromophore [545]. By adjusting the ratio of centrosymmetric LaPO$_4$ to non-centrosymmetric TbPO$_4$-based hydrate, the LaPO$_4$:Tb nanomaterials were demonstrated to have SHG properties due to symmetry breaking. These polymer-inorganic nanocomposites have wide spectral tunability from 375 nm to 425 nm for SHG peaks, with an excitation range of 750–850 nm. They also found that the SHG intensity was related to the refractive indices of the materials and was suggested to vary with the frequency of the fundamental wave [546,547]. In the future, controlling the atom number in the formation of the Au nanocluster might offer an alternative solution, in place of Ln-based nanoparticles, for obtaining color-tunable nanoreagents.

Considering that laser operation in photomedicine is required to be user friendly, a single CW laser irradiation that can perform simultaneous PDT/PPT treatments offers a new attractive method to overcome the intrinsic limitations of PDT or PTT alone. PPT alone is of particular benefit to large-area ablation of tumor cancer cells because the heating area is extended. However, the temperature at the periphery of the tumor tissue is less than at the central site and thus unaffected cancer cells can re-grow and migrate to affect healthy tissue nearby. Synchronous PDT treatment could be developed to assist clean-up of the residual cancer cells. On the other hand, the PDT process is oxygen-independent and has limited efficacy in the hypoxia environment. In that situation, the PTT can still do the job well (oxygen unnecessary). Based on this complementary advantage, a new NIR nanoparticle-platform consisting of a Au nanoreagent and a Ce6 photosensitizer was developed, which exhibited single wavelength stimulation of PTT/PDTon cancer cells at 671 nm (1–2 W/cm^2) [548]. An ICG-loaded human serum albumin composite (~75 nm), developed by Sheng et al. [174], can simultaneously convert the absorbed light energy to singlet oxygen species and heat upon an excitation at 808 nm laser for 5 min (0.8 W/cm^2) thus providing for synergistic PDT/PTT treatment. The combination of PDT and PTT had a higher anticancer efficacy than either single PDT or PTT in an animal study.

In recent years, low-level laser therapy (LLLT) with an NIR laser device has become an increasingly mainstream modality for curing disease [549]. This LLLT system can promote tissue regeneration, reduce inflammation and relieve pain through non-thermal mechanisms [538,550–552]. The most common LLLT management approach includes laser radiation, such as ruby (694 nm), argon (488 and 514 nm), helium-neon (632.8 nm), krypton (521, 530, 568, 647 nm), gallium-aluminum-As (805 or 650 nm), and gallium-AS (904 nm). The proposed LLLT system requires the following [552]:

(a) A power laser with 0.001–0.1 W of output.
(b) A wavelength in the range 300–10,600 nm.
(c) A pulse rate from 0, which is continuous to 5000 Hz (cycles per second).
(d) Intensity doses of 0.01–10 W/cm^2 and 0.01–100 J/cm^2.

However, for most nanoparticle-mediated tumor depletion, the commonly required power density for photo-thermal therapy is 1–6 W/cm^2, despite the high penetration of NIR light [457,553]. In contrast to high-energy photothermal ablation, the PDT treatment requires a lower power density of incident light. Although this advantage is addressed, most photosensitizers [405] (e.g. phthalocyanine-based derivatives [554,555], porphyrin-based compounds [556,557] and phenothiazine structured dyes [76,558,559]) can only be activated upon exposure to visible wavelengths. To overcome the limitation of the light absorption by tissues, upconversion nanoparticles can convert NIR light into visible light, and the neighboring PS can also be excited through FRET [560]. The ideal design is to overlap the emission spectra of UCNPs in some visible regions with photosensitizer loading. This idea was first presented and explored by Prasad and co-workers [561,562]. Since then, many groups have used UCNPs to convert the deeply penetrating near-infrared light into visible wavelengths for the photo-excitation of photosensitizers and then the production of cytotoxic $^1O_2$, resulting in cancer cell damage via apoptotic and necrotic pathways [458,563].

8. Concluding remarks

The engineered nanoparticles discussed here offer improved, often exotic, physico-chemical properties, and thus nanotechnology will definitely gain by the development of such novel NIR-to-NIR materials. Nevertheless, these developments in nanotechnology poses important questions regarding the impact of these new materials on living systems. Numerous

studies have demonstrated the need for nanoparticle risk assessment in relation to a long list of parameters, such as surface charge and (bio)chemistry, size, shape anisotropy, purity, stability, and many others. Such evaluations should contribute to nano-safety considerations during their design and optimization. These existing results also highlight the need to characterize not only NPs, but also the ultimate properties of NPs *in vitro* and *in vivo*, starting from protein adsorption in biological media, colloidal stability, cellular permeability and translocation within cell membranes and whole cells, up to *in vivo* circulation, aggregation, barrier translocation, and finally clearance. This knowledge is important not only for risk assessment of NPs, but also to understand their interaction with biological systems in order to intentionally design enhanced biomedical applications, for use as biomedical imaging, diagnostic tools, and nanoparticle based drug delivery theranostic systems. Moreover, during deep-tissue theranostics, the wavelength and intensity level of NIR excitation should be taken into consideration to achieve the least invasiveness. At excitation wavelengths shorter than 800 nm, endogenous photosensitizers like porphyrins can be excited by two photons, thus generating ROS in tissues. Even though the 1000–1300 nm wavelength range has high penetration in biological tissues, water or pigment absorption induced photo-damage will not be negligible in photoacoustic or high nonlinearity imaging like THG microscopy. A lower pulse excitation rate could help with the relaxation of thermal energy. On the other hand, efficient and multimodal NIR nanomaterials are required to obtain good-enough contrast at low excitation levels.

Acknowledgements

References

[1] Garman KS, Nevins JR, Potti A. Genomic strategies for personalized cancer therapy. Hum Mol Genet 2007;16(Spec no. 2):R226–32.
[2] Garralda E, Paz K, Lopez-Casas PP, Jones S, Katz A, Kann LM, et al. Integrated next-generation sequencing and avatar mouse models for personalized cancer treatment. Clin Cancer Res 2014;20:2476–84.
[3] Conde J, Dias JT, Grazu V, Moros M, Baptista PV, de la Fuente JM. Revisiting 30 years of biofunctionalization and surface chemistry of inorganic nanoparticles for nanomedicine. Front Chem 2014;2:48.
[4] Zhang ZJ, Wang J, Chen CH. Near-infrared light-mediated nanoplatforms for cancer thermo-chemotherapy and optical imaging. Adv Mater 2013;25:3869–80.
[5] Bao CC, Conde J, Polo E, del Pino P, Moros M, Baptista PV, et al. A promising road with challenges: where are gold nanoparticles in translational research? Nanomedicine 2014;9:2353–70.
[6] Li T-J, Huang C-C, Ruan P-W, Chuang K-Y, Huang K-J, Shieh D-B, et al. In vivo anti-cancer efficacy of magnetite nanocrystal-based system using locoregional hyperthermia combined with 5-fluorouracil chemotherapy. Biomaterials 2013;34:7873–83.
[7] Hervault A, Thanh NTK. Magnetic nanoparticle-based therapeutic agents for thermo-chemotherapy treatment of cancer. Nanoscale 2014;6:11553–73.
[8] Huang CC, Chang PY, Liu CL, Xu JP, Wu SP, Kuo WC. New insight on optical and magnetic Fe$_3$O$_4$ nanoclusters promising for near infrared theranostic applications. Nanoscale 2015;7:12689–97.
[9] Cuenca AG, Jiang HB, Hochwald SN, Delano M, Cance WG, Grobmyer SR. Emerging implications of nanotechnology on cancer diagnostics and therapeutics. Cancer 2006;107:459–66.
[10] Doria G, Conde J, Veigas B, Giestas L, Almeida C, Assuncao M, et al. Noble metal nanoparticles for biosensing applications. Sens – Basel 2012;12:1657–87.
[11] Conde J, Doria G, Baptista P. Noble metal nanoparticles applications in cancer. J Drug Deliv 2012;2012:751075.
[12] Arias JL. Advanced methodologies to formulate nanotheragnostic agents for combined drug delivery and imaging. Expert Opin Drug Deliv 2011;8:1589–608.
[13] Perrault SD, Chan WCW. In vivo assembly of nanoparticle components to improve targeted cancer imaging. Proc Natl Acad Sci USA 2010;107:11194–9.
[14] Bouziotis P, Psimadas D, Tsotakos T, Stamopoulos D, Tsoukalas C. Radiolabeled iron oxide nanoparticles as dual-modality SPECT/MRI and PET/MRI agents. Curr Top Med Chem 2012;12:2694–702.
[15] Chou SW, Shau YH, Wu PC, Yang YS, Shieh DB, Chen CC. In vitro and in vivo studies of FePt nanoparticles for dual modal CT/MRI molecular imaging. J Am Chem Soc 2010;132:13270–8.
[16] Popovtzer R, Agrawal A, Kotov NA, Popovtzer A, Balter J, Carey TE, et al. Targeted gold nanoparticles enable molecular CT imaging of cancer. Nano Lett 2008;8:4593–6.
[17] Kim D, Park S, Lee JH, Jeong YY, Jon S. Antibiofouling polymer-coated gold nanoparticles as a contrast agent for in vivo X-ray computed tomography imaging. J Am Chem Soc 2007;129:7661–5.
[18] Caravan P, Ellison JJ, McMurry TJ, Lauffer RB. Gadolinium(III) chelates as MRI contrast agents: structure, dynamics, and applications. Chem Rev 1999;99:2293–352.
[19] Weissleder R, Elizondo G, Wittenberg J, Rabito CA, Bengele HH, Josephson L. Ultrasmall superparamagnetic iron-oxide – characterization of a new class of contrast agents for MR imaging. Radiology 1990;175:489–93.
[20] Rieffel J, Chen F, Kim J, Chen G, Shao W, Shao S, et al. Hexamodal imaging with porphyrin-phospholipid-coated upconversion nanoparticles. Adv Mater 2015;1–6.
[21] Conde J, Rosa J, Lima JC, Baptista PV. Nanophotonics for molecular diagnostics and therapy applications. Int J Photoenergy 2012;2012:1–11.
[22] Dabbousi BO, RodriguezViejo J, Mikulec FV, Heine JR, Mattoussi H, Ober R, et al. (CdSe)ZnS core-shell quantum dots: synthesis and characterization of a size series of highly luminescent nanocrystallites. J Phys Chem B 1997;101:9463–75.

[23] Liu CL, Liu TM, Hsieh TY, Liu HW, Chen YS, Tsai CK, et al. In vivo metabolic imaging of insulin with multiphoton fluorescence of human insulin-Au nanodots. Small 2013;9:2103–10.

[24] Abad JM, Sendroiu LE, Gass M, Bleloch A, Mills AJ, Schiffrin DJ. Synthesis of omega-hydroxy hexathiolate-protected subnanometric gold clusters. J Am Chem Soc 2007;129:12932.

[25] Link S, El-Sayed MA, Schaaff TG, Whetten RL. Transition from nanoparticle to molecular behavior: a femtosecond transient absorption study of a size-selected 28 atom gold cluster. Chem Phys Lett 2002;356:240–6.

[26] Woehrle GH, Brown LO, Hutchison JE. Thiol-functionalized, 1.5-nm gold nanoparticles through ligand exchange reactions: scope and mechanism of ligand exchange. J Am Chem Soc 2005;127:2172–83.

[27] Wu TJ, Tzeng YK, Chang WW, Cheng CA, Kuo Y, Chien CH, et al. Tracking the engraftment and regenerative capabilities of transplanted lung stem cells using fluorescent nanodiamonds. Nat Nanotechnol 2013;8:682–9.

[28] Yu SJ, Kang MW, Chang HC, Chen KM, Yu YC. Bright fluorescent nanodiamonds: no photobleaching and low cytotoxicity. J Am Chem Soc 2005;127:17604–5.

[29] Liao MY, Wu CH, Lai PS, Yu JS, Lin HP, Liu TM, et al. Surface state mediated NIR two-photon fluorescence of iron oxides for nonlinear optical microscopy. Adv Funct Mater 2013;23:2044–51.

[30] Wang GJ, Volkow ND, Logan J, Pappas NR, Wong CT, Zhu W, et al. Brain dopamine and obesity. Lancet 2001;357:354–7.

[31] Wu CF, Bull B, Christensen K, McNeill J. Ratiometric single-nanoparticle oxygen sensors for biological imaging. Angew Chem – Int Ed 2009;48:2741–5.

[32] Lee YEK, Ulbrich EE, Kim G, Hah H, Strollo C, Fan WZ, et al. Near infrared luminescent oxygen nanosensors with nanoparticle matrix tailored sensitivity. Anal Chem 2010;82:8446–55.

[33] Brinas RP, Troxler T, Hochstrasser RM, Vinogradov SA. Phosphorescent oxygen sensor with dendritic protection and two-photon absorbing antenna. J Am Chem Soc 2005;127:11851–62.

[34] Koo YEL, Cao YF, Kopelman R, Koo SM, Brasuel M, Philbert MA. Real-time measurements of dissolved oxygen inside live cells by organically modified silicate fluorescent nanosensors. Anal Chem 2004;76:2498–505.

[35] Xu H, Aylott JW, Kopelman R, Miller TJ, Philbert MA. A real-time ratiometric method for the determination of molecular oxygen inside living cells using sol-gel-based spherical optical nanosensors with applications to rat C6 glioma. Anal Chem 2001;73:4124–33.

[36] Li YY, Wen T, Zhao RF, Liu XX, Ji TJ, Wang H, et al. Localized electric field of plasmonic nanoplatform enhanced photodynamic tumor therapy. ACS Nano 2014;8:11529–42.

[37] Li C. A targeted approach to cancer imaging and therapy. Nat Mater 2014;13:110–5.

[38] Sumer B, Gao J. Theranostic nanomedicine for cancer. Nanomedicine (Lond) 2008;3:137–40.

[39] Link S, Wang ZL, El-Sayed MA. How does a gold nanorod melt? J Phys Chem B 2000;104:7867–70.

[40] Hu KW, Liu TM, Chung KY, Huang KS, Hsieh CT, Sun CK, et al. Efficient near-IR hyperthermia and intense nonlinear optical imaging contrast on the gold nanorod-in-shell nanostructures. J Am Chem Soc 2009;131:14186.

[41] Jaffe HH, Miller AL. The fates of electronic excitation energy. J Chem Educ 1966;43:469.

[42] Jiang P, Tian Z-Q, Zhu C-N, Zhang Z-L, Pang D-W. Emission-tunable near-infrared Ag_2S quantum dots. Chem Mater 2012;24:3–5.

[43] Liu S, Zhang H, Qiao Y, Su X. One-pot synthesis of ternary $CuInS_2$ quantum dots with near-infrared fluorescence in aqueous solution. RSC Adv 2012;2:819–25.

[44] O'Connell MJ, Bachilo SM, Huffman CB, Moore VC, Strano MS, Haroz EH, et al. Band gap fluorescence from individual single-walled carbon nanotubes. Science 2002;297:593–6.

[45] Bachilo SM, Strano MS, Kittrell C, Hauge RH, Smalley RE, Weisman RB. Structure-assigned optical spectra of single-walled carbon nanotubes. Science 2002;298:2361–6.

[46] Welsher K, Liu Z, Daranciang D, Dai H. Selective probing and imaging of cells with single walled carbon nanotubes as near-infrared fluorescent molecules. Nano Lett 2008;8:586–90.

[47] Kim S, Fisher B, Eisler H-J, Bawendi M. Type-II quantum dots: CdTe/CdSe(core/shell) and CdSe/ZnTe(core/shell) heterostructures. J Am Chem Soc 2003;125:11466–7.

[48] Sykora M, Mangolini L, Schaller RD, Kortshagen U, Jurbergs D, Klimov VI. Size-dependent intrinsic radiative decay rates of silicon nanocrystals at large confinement energies. Phys Rev Lett 2008;100.

[49] Henderson EJ, Shuhendler AJ, Prasad P, Baumann V, Maier-Flaig F, Faulkner DO, et al. Colloidally stable silicon nanocrystals with near-infrared photoluminescence for biological fluorescence imaging. Small 2011;7:2507–16.

[50] Wang X, Cao L, Yang ST, Lu FS, Meziani MJ, Tian LL, et al. Bandgap-like strong fluorescence in functionalized carbon nanoparticles. Angew Chem – Int Ed 2010;49:5310–4.

[51] Baker SN, Baker GA. Luminescent carbon nanodots: emergent nanolights. Angew Chem – Int Ed 2010;49:6726–44.

[52] Liu HP, Ye T, Mao CD. Fluorescent carbon nanoparticles derived from candle soot. Angew Chem – Int Ed 2007;46:6473–5.

[53] Sun YP, Zhou B, Lin Y, Wang W, Fernando KAS, Pathak P, et al. Quantum-sized carbon dots for bright and colorful photoluminescence. J Am Chem Soc 2006;128:7756–7.

[54] Xu XY, Ray R, Gu YL, Ploehn HJ, Gearheart L, Raker K, et al. Electrophoretic analysis and purification of fluorescent single-walled carbon nanotube fragments. J Am Chem Soc 2004;126:12736–7.

[55] Xie JP, Zheng YG, Ying JY. Protein-directed synthesis of highly fluorescent gold nanoclusters. J Am Chem Soc 2009;131:888.

[56] Zhang CY, Yeh HC, Kuroki MT, Wang TH. Single-quantum-dot-based DNA nanosensor. Nat Mater 2005;4:826–31.

[57] Medintz IL, Uyeda HT, Goldman ER, Mattoussi H. Quantum dot bioconjugates for imaging, labelling and sensing. Nat Mater 2005;4:435–46.

[58] Chen HT, Kim SW, Li L, Wang SY, Park K, Cheng JX. Release of hydrophobic molecules from polymer micelles into cell membranes revealed by Forster resonance energy transfer imaging. Proc Natl Acad Sci USA 2008;105:6596–601.

[59] Lee CH, Cheng SH, Huang IP, Souris JS, Yang CS, Mou CY, et al. Intracellular pH-responsive mesoporous silica nanoparticles for the controlled release of anticancer chemotherapeutics. Angew Chem – Int Ed 2010;49:8214–9.

[60] Blacker TS, Mann ZF, Gale JE, Ziegler M, Bain AJ, Szabadkai G, et al. Separating NADH and NADPH fluorescence in live cells and tissues using FLIM. Nat Commun 2014;5.

[61] Lakowicz JR, Szmacinski H, Nowaczyk K, Johnson ML. Fluorescence lifetime imaging of free and protein-bound NADH. Proc Natl Acad Sci USA 1992;89:1271–5.

[62] Hui YY, Su LJ, Chen OY, Chen YT, Liu TM, Chang HC. Wide-field imaging and flow cytometric analysis of cancer cells in blood by fluorescent nanodiamond labeling and time gating. Sci Rep-Uk 2014;4.

[63] Wilson DF, Vinogradov SA, Grosul P, Kuroki A, Bennett J. Imaging oxygen pressure in the retina of the mouse eye. Adv Exp Med Biol 2005;566:159–65.

[64] Sakadzic S, Roussakis E, Yaseen MA, Mandeville ET, Srinivasan VJ, Arai K, et al. Two-photon high-resolution measurement of partial pressure of oxygen in cerebral vasculature and tissue. Nat Methods 2010;7. 755-U125.

[65] Spencer JA, Ferraro F, Roussakis E, Klein A, Wu JW, Runnels JM, et al. Direct measurement of local oxygen concentration in the bone marrow of live animals. Nature 2014;508:269.

[66] Skalak R, Branemar Pi. Deformation of red blood cells in capillaries. Science 1969;164:717.

[67] Zhang HF, Maslov K, Stoica G, Wang LHV. Functional photoacoustic microscopy for high-resolution and noninvasive in vivo imaging. Nat Biotechnol 2006;24:848–51.

[68] Bao CC, Beziere N, del Pino P, Pelaz B, Estrada G, Tian FR, et al. Gold nanoprisms as optoacoustic signal nanoamplifiers for in vivo bioimaging of gastrointestinal cancers. Small 2013;9:68–74.

[69] Bao CC, Conde J, Pan F, Li C, Zhang CL, Tian FR, et al. Gold nanoprisms as a hybrid in vivo cancer theranostic platform for in situ photoacoustic imaging, angiography, and localized hyperthermia. Nano Res 2016;9:1043–56.
[70] Anker JN, Hall WP, Lyandres O, Shah NC, Zhao J, Van Duyne RP. Biosensing with plasmonic nanosensors. Nat Mater 2008;7:442–53.
[71] Zhao Q, Zhou J, Zhang FL, Lippens D. Mie resonance-based dielectric metamaterials. Mater Today 2009;12:60–9.
[72] Luther JM, Jain PK, Ewers T, Alivisatos AP. Localized surface plasmon resonances arising from free carriers in doped quantum dots. Nat Mater 2011;10:361–6.
[73] Nie SM, Emery SR. Probing single molecules and single nanoparticles by surface-enhanced Raman scattering. Science 1997;275:1102–6.
[74] Liu TM, Tai SP, Yu CH, Wen YC, Chu SW, Chen LJ, et al. Measuring plasmon-resonance enhanced third-harmonic chi$^{(3)}$ of Ag nanoparticles. Appl Phys Lett 2006;89.
[75] Tai SP, Wu Y, Shieh DB, Chen LJ, Lin KJ, Yu CH, et al. Molecular imaging of cancer cells using plasmon-resonant-enhanced third-harmonic-generation in silver nanoparticles. Adv Mater 2007;19:4520.
[76] Liu TM, Yu JS, Chang CA, Chiou A, Chiang HK, Chuang YC, et al. One-step shell polymerization of inorganic nanoparticles and their applications in SERS/nonlinear optical imaging, drug delivery, and catalysis. Sci Rep-Uk 2014;4.
[77] Kneipp K, Kneipp H, Itzkan I, Dasari RR, Feld MS. Ultrasensitive chemical analysis by Raman spectroscopy. Chem Rev 1999;99:2957–76.
[78] Samanta A, Maiti KK, Soh KS, Liao XJ, Vendrell M, Dinish US, et al. Ultrasensitive near-infrared Raman reporters for SERS-based in vivo cancer detection. Angew Chem – Int Ed 2011;50:6089–92.
[79] Zheng XS, Hu P, Cui Y, Zong C, Feng JM, Wang X, et al. BSA-coated nanoparticles for improved SERS-based intracellular pH sensing. Anal Chem 2014;86:12250–7.
[80] Nima ZA, Mahmood M, Xu Y, Mustafa T, Watanabe F, Nedosekin DA, et al. Circulating tumor cell identification by functionalized silver-gold nanorods with multicolor, super-enhanced SERS and photothermal resonances. Sci Rep-Uk 2014;4.
[81] Murphy CJ. Optical sensing with quantum dots. Anal Chem 2002;74:520a–6a.
[82] Han MY, Gao XH, Su JZ, Nie S. Quantum-dot-tagged microbeads for multiplexed optical coding of biomolecules. Nat Biotechnol 2001;19:631–5.
[83] Wolkin MV, Jorne J, Fauchet PM, Allan G, Delerue C. Electronic states and luminescence in porous silicon quantum dots: the role of oxygen. Phys Rev Lett 1999;82:197–200.
[84] Haase M, Schafer H. Upconverting nanoparticles. Angew Chem – Int Ed 2011;50:5808–29.
[85] Heer S, Kompe K, Gudel HU, Haase M. Highly efficient multicolour upconversion emission in transparent colloids of lanthanide-doped NaYF$_4$ nanocrystals. Adv Mater 2004;16:2102.
[86] Babu P, Martin IR, Krishnaiah KV, Seo HJ, Venkatramu V, Jayasankar CK, et al. Photon avalanche upconversion in Ho^{3+}-Yb^{3+} co-doped transparent oxyfluoride glass-ceramics. Chem Phys Lett 2014;600:34–7.
[87] Yi GS, Chow GM. Water-soluble NaYF$_4$:Yb,Er(Tm)/NaYF$_4$/polymer core/shell/shell nanoparticles with significant enhancement of upconversion fluorescence. Chem Mater 2007;19:341–3.
[88] Zhong Y, Tian G, Gu Z, Yang Y, Gu L, Zhao Y, et al. Elimination of photon quenching by a transition layer to fabricate a quenching-shield sandwich structure for 800 nm excited upconversion luminescence of Nd^{3+}-sensitized nanoparticles. Adv Mater 2014;26:2831–7.
[89] Qiu HL, Yang CH, Shao W, Damasco J, Wang XL, Agren H, et al. Enhanced upconversion luminescence in Yb^{3+}/Tm^{3+}-codoped fluoride active core/active shell/inert shell nanoparticles through directed energy migration. Nanomater – Basel 2014;4:55–68.
[90] Gu Z, Yan L, Tian G, Li S, Chai Z, Zhao Y. Recent advances in design and fabrication of upconversion nanoparticles and their safe theranostic applications. Adv Mater 2013;25:3758–79.
[91] Stender AS, Marchuk K, Liu C, Sander S, Meyer MW, Smith EA, et al. Single cell optical imaging and spectroscopy. Chem Rev 2013;113:2469–527.
[92] Chu SW, Chen IH, Liu TM, Chen PC, Sun CK, Lin BL. Multimodal nonlinear spectral microscopy based on a femtosecond Cr:forsterite laser. Opt Lett 2001;26:1909–11.
[93] Campagnola PJ, Millard AC, Terasaki M, Hoppe PE, Malone CJ, Mohler WA. Three-dimensional high-resolution second-harmonic generation imaging of endogenous structural proteins in biological tissues. Biophys J 2002;82:493–508.
[94] Chu SW, Liu TM, Sun CK. Real-time second-harmonic-generation microscopy based on a 2-GHz repetition rate Ti:sapphire laser. Opt Express 2003;11:933–8.
[95] Chu SW, Chen SY, Tsai TH, Liu TM, Lin CY, Tsai HJ, et al. In vivo developmental biology study using noninvasive multi-harmonic generation microscopy. Opt Express 2003;11:3093–9.
[96] Campagnola PJ, Loew LM. Second-harmonic imaging microscopy for visualizing biomolecular arrays in cells, tissues and organisms. Nat Biotechnol 2003;21:1356–60.
[97] Fu Y, Wang HF, Shi RY, Cheng JX. Second harmonic and sum frequency generation imaging of fibrous astroglial filaments in ex vivo spinal tissues. Biophys J 2007;92:3251–9.
[98] Dombeck DA, Kasischke KA, Vishwasrao HD, Ingelsson M, Hyman BT, Webb WW. Uniform polarity microtubule assemblies imaged in native brain tissue by second-harmonic generation microscopy. Proc Natl Acad Sci USA 2003;100:7081–6.
[99] Hsieh CS, Ko CY, Chen SY, Liu TM, Wu JS, Hu CH, et al. In vivo long-term continuous observation of gene expression in zebrafish embryo nerve systems by using harmonic generation microscopy and morphant technology. J Biomed Opt 2008;13.
[100] Hsieh CS, Chen SU, Lee YW, Yang YS, Sun CK. Higher harmonic generation microscopy of in vitro cultured mammal oocytes and embryos. Opt Express 2008;16:11574–88.
[101] Tsai TH, Tai SP, Lee WJ, Huang HY, Liao YH, Sun CK. Optical signal degradation study in fixed human skin using confocal microscopy and higher-harmonic optical microscopy. Opt Express 2006;14:749–58.
[102] Chen SY, Wu HY, Sun CK. In vivo harmonic generation biopsy of human skin. J Biomed Opt 2009;14.
[103] Lee JH, Chen SY, Yu CH, Chu SW, Wang LF, Sun CK, et al. Noninvasive in vitro and in vivo assessment of epidermal hyperkeratosis and dermal fibrosis in atopic dermatitis. J Biomed Opt 2009;14.
[104] Liao YH, Kuo WC, Chou SY, Tsai CS, Lin GL, Tsai MR, et al. Quantitative analysis of intrinsic skin aging in dermal papillae by in vivo harmonic generation microscopy. Biomed Opt Exp 2014;5:3266–79.
[105] Wu PC, Hsieh TY, Tsai ZU, Liu TM. In vivo quantification of the structural changes of collagens in a melanoma microenvironment with second and third harmonic generation microscopy. Sci Rep-Uk 2015;5.
[106] Butet J, Duboisset J, Bachelier G, Russier-Antoine I, Benichou E, Jonin C, et al. Optical second harmonic generation of single metallic nanoparticles embedded in a homogeneous medium. Nano Lett 2010;10:1717–21.
[107] Nappa J, Revillod G, Russier-Antoine I, Benichou E, Jonin C, Brevet PF. Electric dipole origin of the second harmonic generation of small metallic particles. Phys Rev B 2005;71.
[108] Huang CC, Chuang KY, Huang CJ, Liu TM, Yeh CS. Graphite-shelled Si nanoparticles and their Au/Si heterodimers: preparation, photoluminescence, and second harmonic generation. J Phys Chem C 2011;115:9952–60.
[109] Pantazis P, Maloney J, Wu D, Fraser SE. Second harmonic generating (SHG) nanoprobes for in vivo imaging. Proc Natl Acad Sci USA 2010;107:14535–40.
[110] Yelin D, Silberberg Y. Laser scanning third-harmonic-generation microscopy in biology. Opt Express 1999;5:169–75.
[111] Tsai CK, Wang TD, Lin JW, Hsu RB, Guo LZ, Chen ST, et al. Virtual optical biopsy of human adipocytes with third harmonic generation microscopy. Biomed Opt Exp 2013;4:178–86.
[112] Debarre D, Supatto W, Pena AM, Fabre A, Tordjmann T, Combettes L, et al. Imaging lipid bodies in cells and tissues using third-harmonic generation microscopy. Nat Methods 2006;3:47–53.

[113] Yu CH, Tai SP, Kung CT, Wang IJ, Yu HC, Huang HJ, et al. In vivo and ex vivo imaging of intra-tissue elastic fibers using third-harmonic-generation microscopy. Opt Express 2007;15:11167–77.

[114] Chang CF, Yu CH, Sun CK. Multi-photon resonance enhancement of third harmonic generation in human oxyhemoglobin and deoxyhemoglobin. J Biophotonics 2010;3:678–85.

[115] Tsai CK, Chen YS, Wu PC, Hsieh TY, Liu HW, Yeh CY, et al. Imaging granularity of leukocytes with third harmonic generation microscopy. Biomed Opt Exp 2012;3:2234–43.

[116] Chen CK, Liu TM. Imaging morphodynamics of human blood cells in vivo with video-rate third harmonic generation microscopy. Biomed Opt Exp 2012;3:2860–5.

[117] Blom FC, Driessen A, Hoekstra HJWM, van Schoot JBP, Popma TJA. Third harmonic generation as a rapid selection tool for organic materials for nonlinear integrated optics devices. Opt Mater 1999;12:327–31.

[118] Chang CF, Chen HC, Chen MJ, Liu WR, Hsieh WF, Hsu CH, et al. Direct backward third-harmonic generation in nanostructures. Opt Express 2010;18:7397–406.

[119] Chang CF, Chen CY, Chang FH, Tai SP, Chen CY, Yu CH, et al. Cell tracking and detection of molecular expression in live cells using lipid-enclosed CdSe quantum dots as contrast agents for epi-third harmonic generation microscopy. Opt Express 2008;16:9534–48.

[120] Jung Y, Tong L, Tanaudommongkon A, Cheng JX, Yang C. In vitro and in vivo nonlinear optical imaging of silicon nanowires. Nano Lett 2009;9:2440–4.

[121] Zumbusch A, Holtom GR, Xie XS. Three-dimensional vibrational imaging by coherent anti-Stokes Raman scattering. Phys Rev Lett 1999;82:4142–5.

[122] Evans CL, Xie XS. Coherent anti-stokes Raman scattering microscopy: chemical imaging for biology and medicine. Annu Rev Anal Chem 2008;1:883–909.

[123] Freudiger CW, Min W, Saar BG, Lu S, Holtom GR, He CW, et al. Label-free biomedical imaging with high sensitivity by stimulated Raman scattering microscopy. Science 2008;322:1857–61.

[124] Saar BG, Freudiger CW, Reichman J, Stanley CM, Holtom GR, Xie XS. Video-rate molecular imaging in vivo with stimulated Raman scattering. Science 2010;330:1368–70.

[125] Kim H, Sheps T, Collins PG, Potma EO. Nonlinear optical imaging of individual carbon nanotubes with four-wave-mixing microscopy. Nano Lett 2009;9:2991–5.

[126] Pope I, Payne L, Zoriniants G, Thomas E, Williams O, Watson P, et al. Coherent anti-Stokes Raman scattering microscopy of single nanodiamonds. Nat Nanotechnol 2014;9:940–6.

[127] Jungst C, Winterhalder MJ, Zumbusch A. Fast and long term lipid droplet tracking with CARS microscopy. J Biophotonics 2011;4:435–41.

[128] Denk W, Strickler JH, Webb WW. 2-Photon laser scanning fluorescence microscopy. Science 1990;248:73–6.

[129] Zipfel WR, Williams RM, Webb WW. Nonlinear magic: multiphoton microscopy in the biosciences. Nat Biotechnol 2003;21:1368–76.

[130] Konig K. Multiphoton microscopy in life sciences. J Microsc 2000;200:83–104.

[131] Anderson RR, Parrish JA. The optics of human-skin. J Invest Dermatol 1981;77:13–9.

[132] Phan TG, Bullen A. Practical intravital two-photon microscopy for immunological research: faster, brighter, deeper. Immunol Cell Biol 2010;88:438–44.

[133] Horton NG, Wang K, Kobat D, Clark CG, Wise FW, Schaffer CB, et al. In vivo three-photon microscopy of subcortical structures within an intact mouse brain. Nat Photonics 2013;7:205–9.

[134] Moncorgé R, Merkle LD, Zandi B. UV-visible lasers based on rare-earth ions. MRS Bull 1999;24:21–6.

[135] Geusic JE, Marcos HM, Van Uitert LG. Laser oscillations in nd-doped yttrium aluminum, yttrium gallium and gadolinium garnets. Appl Phys Lett 1964;4.

[136] Quarles GJ, Rosenbaum A, Marquardt CL, Esterowitz L. Efficient room-temperature operation of a flash-lamp-pumped, Cr,Tm:YAG laser at 2.01 micron. Opt Lett 1990;15:42–4.

[137] Digonnet MJF. Rare-earth-doped fiber lasers and amplifiers. 2nd ed rev., expanded ed. New York: Marcel Dekker; 2001.

[138] Lakshmanan A. Luminescence and display phosphors: phenomena and applications. New York; Lancaster: Nova Science Publishers; Gazelle Drake Academic [distributor]; 2008.

[139] Esterowitz L, Schnitzler A, Noonan J, Bahler J. Rare Earth infrared quantum counter. Appl Opt 1968;7:2053–70.

[140] Auzel F. Upconversion and anti-stokes processes with f and d ions in solids. Chem Rev 2004;104:139–73.

[141] Downing E, Hesselink L, Ralston J, Macfarlane R. A three-color, solid-state, three-dimensional display. Science 1996;273:1185–9.

[142] Berthou H, Jorgensen CK. Optical-fiber temperature sensor based on upconversion-excited fluorescence. Opt Lett 1990;15:1100–2.

[143] Lenth W, Macfarlane RM, Silversmith AJ. Green infrared-pumped upconversion lasers. Opt News 1987;13:26–9.

[144] Wang YF, Liu GY, Sun LD, Xiao JW, Zhou JC, Yan CH. Nd^{3+}-sensitized upconversion nanophosphors: efficient in vivo bioimaging probes with minimized heating effect. ACS Nano 2013;7:7200–6.

[145] Zhong Y, Tian G, Gu Z, Yang Y, Gu L, Zhao Y, et al. Elimination of photon quenching by a transition layer to fabricate a quenching-shield sandwich structure for 800 nm excited upconversion luminescence of Nd-sensitized nanoparticles. Adv Mater 2013.

[146] Wang F, Deng R, Wang J, Wang Q, Han Y, Zhu H, et al. Tuning upconversion through energy migration in core-shell nanoparticles. Nat Mater 2011;10:968–73.

[147] Rajendran M, Yapici E, Miller LW. Lanthanide-based imaging of protein-protein interactions in live cells. Inorg Chem 2014;53:1839–53.

[148] Wang R, Zhang F. NIR luminescent nanomaterials for biomedical imaging. J Mater Chem B 2014;2:2422–43.

[149] Rocha U, Kumar KU, Jacinto C, Villa I, Sanz-Rodriguez F, de la Cruz Iglesias, et al. Neodymium-doped LaF_3 nanoparticles for fluorescence bioimaging in the second biological window. Small 2014;10:1141–54.

[150] Rocha U, Jacinto da Silva C, Ferreira Silva W, Guedes I, Benayas A, Martinez Maestro L, et al. Subtissue thermal sensing based on neodymium-doped LaF_3 nanoparticles. ACS Nano 2013;7:1188–99.

[151] Yu XF, Chen LD, Li M, Xie MY, Zhou L, Li T, et al. Highly efficient fluorescence of NdF_3 SiO_2 core/shell nanoparticles and the applications for in vivo NIR detection. Adv Mater 2008;10:1–6.

[152] Kamimura M, Kanayama N, Tokuzen K, Soga K, Nagasaki Y. Near-infrared (1550 nm) in vivo bioimaging based on rare-earth doped ceramic nanophosphors modified with PEG-b-poly(4-vinylbenzylphosphonate). Nanoscale 2011;3:3705–13.

[153] Chen GY, Ohulchanskyy TY, Liu S, Law WC, Wu F, Swihart MT, et al. Core/shell $NaGdF_4$:Nd^{3+}/$NaGdF_4$ nanocrystals with efficient near-infrared to near-infrared downconversion photoluminescence for bioimaging applications. ACS Nano 2012;6:2969–77.

[154] Naczynski DJ, Tan MC, Zevon M, Wall B, Kohl J, Kulesa A, et al. Rare-earth-doped biological composites as in vivo shortwave infrared reporters. Nat Commun 2013;4:2199.

[155] Xie X, Gao N, Deng R, Sun Q, Xu QH, Liu X. Mechanistic investigation of photon upconversion in Nd^{3+}-sensitized core-shell nanoparticles. J Am Chem Soc 2013;135:12608–11.

[156] Singh S, Smith RG, Vanuiter Lg. Stimulated-emission cross-section and fluorescent quantum efficiency of Nd^{3+} in yttrium aluminum garnet at room-temperature. Phys Rev B 1974;10:2566–72.

[157] Kim C, Erpelding TN, Jankovic L, Pashley MD, Wang LHV. Deeply penetrating in vivo photoacoustic imaging using a clinical ultrasound array system. Biomed Opt Exp 2010;1:278–84.

[158] Wang P, Wang HW, Sturek M, Cheng JX. Bond-selective imaging of deep tissue through the optical window between 1600 and 1850 nm. J Biophotonics 2012;5:25–32.

[159] Fan YX, He JL, Wang YG, Liu S, Wang HT, Ma XY. 2-ps passively mode-locked Nd:YVO_4 laser using an output-coupling-type semiconductor saturable absorber mirror. Appl Phys Lett 2005;86.

[160] Yang YL, Li FH, Gao L, Wang ZY, Thrall MJ, Shen SS, et al. Differential diagnosis of breast cancer using quantitative, label-free and molecular vibrational imaging. Biomed Opt Exp 2011;2:2160–74.
[161] Zipfel WR, Williams RM, Christie R, Nikitin AY, Hyman BT, Webb WW. Live tissue intrinsic emission microscopy using multiphoton-excited native fluorescence and second harmonic generation. Proc Natl Acad Sci USA 2003;100:7075–80.
[162] Chen SY, Chen SU, Wu HY, Lee WJ, Liao YH, Sun CK. In vivo virtual biopsy of human skin by using noninvasive higher harmonic generation microscopy. IEEE J Sel Top Quant 2010;16:478–92.
[163] Tsai MR, Chen SY, Shieh DB, Lou PJ, Sun CK. In vivo optical virtual biopsy of human oral mucosa with harmonic generation microscopy. Biomed Opt Exp 2011;2:2317–28.
[164] Liao YH, Chen SY, Chou SY, Wang PH, Tsai MR, Sun CK. Determination of chronological aging parameters in epidermal keratinocytes by in vivo harmonic generation microscopy. Biomed Opt Exp 2013;4:77–88.
[165] Zhai YH, Goulart C, Sharping JE, Wei HF, Chen S, Tong WJ, et al. Multimodal coherent anti-Stokes Raman spectroscopic imaging with a fiber optical parametric oscillator. Appl Phys Lett 2011;98.
[166] Nie B, Saytashev I, Chong AD, Liu H, Arkhipov SN, Wise FW, et al. Multimodal microscopy with sub-30 fs Yb fiber laser oscillator. Biomed Opt Exp 2012;3:1750–6.
[167] Wang K, Liu TM, Wu JW, Horton NG, Lin CP, Xu C. Three-color femtosecond source for simultaneous excitation of three fluorescent proteins in two-photon fluorescence microscopy. Biomed Opt Exp 2012;3:1972–7.
[168] Kobayashi H, Ogawa M, Alford R, Choyke PL, Urano Y. New strategies for fluorescent probe design in medical diagnostic imaging. Chem Rev 2010;110:2620–40.
[169] Saxena V, Sadoqi M, Shao J. Degradation kinetics of indocyanine green in aqueous solution. J Pharm Sci 2003;92:2090–7.
[170] Yu J, Yaseen MA, Anvari B, Wong MS. Synthesis of near-infrared-absorbing nanoparticle-assembled capsules. Chem Mater 2007;19:1277–84.
[171] Peng CL, Shih YH, Lee PC, Hsieh TMH, Luo TY, Shieh MJ. Multimodal image-guided photothermal therapy mediated by Re-188-labeled micelles containing a cyanine-type photosensitizer. ACS Nano 2011;5:5594–607.
[172] Yuan A, Qiu XF, Tang XL, Liu W, Wu JH, Hu YQ. Self-assembled PEG-IR-780-C13 micelle as a targeting, safe and highly-effective photothermal agent for in vivo imaging and cancer therapy. Biomaterials 2015;51:184–93.
[173] Zheng MB, Yue CX, Ma YF, Gong P, Zhao PF, Zheng CF, et al. Single-step assembly of DOX/ICG loaded lipid-polymer nanoparticles for highly effective chemo-photothermal combination therapy. ACS Nano 2013;7:2056–67.
[174] Sheng ZH, Hu DH, Zheng MB, Zhao PF, Liu HL, Gao DY, et al. Smart human serum albumin-indocyanine green nanoparticles generated by programmed assembly for dual-modal imaging-guided cancer synergistic phototherapy. ACS Nano 2014;8:12310–22.
[175] Lee CH, Cheng SH, Wang YJ, Chen YC, Chen NT, Souris J, et al. Near-infrared mesoporous silica nanoparticles for optical imaging: characterization and in vivo biodistribution. Adv Func Mater 2009;19:215–22.
[176] Xing L, Zheng HQ, Cao YY, Che SA. Coordination polymer coated mesoporous silica nanoparticles for pH-responsive drug release. Adv Mater 2012;24:6433–7.
[177] Luo T, Huang P, Gao G, Shen GX, Fu S, Cui DX, et al. Mesoporous silica-coated gold nanorods with embedded indocyanine green for dual mode X-ray CT and NIR fluorescence imaging. Opt Express 2011;19:17030–9.
[178] Schonbachler A, Glaied O, Huwyler J, Frenz M, Pieles U. Indocyanine green loaded biocompatible nanoparticles: stabilization of indocyanine green (ICG) using biocompatible silica-poly(epsilon-caprolactone) grafted nanocomposites. J Photochem Photobiol A 2013;261:12–9.
[179] Kuo WS, Chang YT, Cho KC, Chiu KC, Lien CH, Yeh CS, et al. Gold nanomaterials conjugated with indocyanine green for dual-modality photodynamic and photothermal therapy. Biomaterials 2012;33:3270–8.
[180] Chu LL, Wang SW, Li KH, Xi W, Zhao XY, Qian J. Biocompatible near-infrared fluorescent nanoparticles for macro and microscopic in vivo functional bioimaging. Biomed Opt Exp 2014;5:4076–88.
[181] Lapadula G, Trummer D, Conley MP, Steinmann M, Ran YF, Brasselet S, et al. One-photon near-infrared sensitization of well-defined Yb(III) surface complexes for NIR-to-NIR single nanoparticle imaging. Chem Mater 2015;27:2033–9.
[182] Howes P, Green M, Levitt J, Suhling K, Hughes M. Phospholipid encapsulated semiconducting polymer nanoparticles: their use in cell imaging and protein attachment. J Am Chem Soc 2010;132:3989–96.
[183] Wu CF, Hansen SJ, Hou QO, Yu JB, Zeigler M, Jin YH, et al. Design of highly emissive polymer dot bioconjugates for in vivo tumor targeting. Angew Chem – Int Ed 2011;50:3430–4.
[184] Pu KY, Liu B. Fluorescent conjugated polyelectrolytes for bioimaging. Adv Func Mater 2011;21:3408–23.
[185] Pu KY, Li K, Liu B. Multicolor conjugate polyelectrolyte/peptide complexes as self-assembled nanoparticles for receptor-targeted cellular imaging. Chem Mater 2010;22:6736–41.
[186] Mcrae RL, Phillips RL, Kim IB, Bunz UHF, Fahrni CJ. Molecular recognition based on low-affinity polyvalent interactions: selective binding of a carboxylated polymer to fibronectin fibrils of live fibroblast cells. J Am Chem Soc 2008;130:7851.
[187] Qu SN, Wang XY, Lu QP, Liu XY, Wang LJ. A biocompatible fluorescent ink based on water-soluble luminescent carbon nanodots. Angew Chem – Int Ed 2012;51:12215–8.
[188] Pansare VJ, Hejazi S, Faenza WJ, Prud'homme RK. Review of long-wavelength optical and NIR imaging materials: contrast agents, fluorophores, and multifunctional nano carriers. Chem Mater 2012;24:812–27.
[189] Luo SL, Zhang EL, Su YP, Cheng TM, Shi CM. A review of NIR dyes in cancer targeting and imaging. Biomaterials 2011;32:7127–38.
[190] Wang D, Qian J, He SL, Park JS, Lee KS, Han SH, et al. Aggregation-enhanced fluorescence in PEGylated phospholipid nanomicelles for in vivo imaging. Biomaterials 2011;32:5880–8.
[191] Li K, Liu B. Polymer-encapsulated organic nanoparticles for fluorescence and photoacoustic imaging. Chem Soc Rev 2014;43:6570–97.
[192] Xiong LQ, Shuhendler AJ, Rao JH. Self-luminescing BRET-FRET near-infrared dots for in vivo lymph-node mapping and tumour imaging. Nat Commun 2012;3.
[193] Lefebvre M, Qi ZG, Rana D, Pickup PG. Chemical synthesis, characterization, and electrochemical studies of poly(3,4-ethylenedioxythiophene)/poly (styrene-4-sulfonate) composites. Chem Mater 1999;11:262–8.
[194] Yun JM, Yeo JS, Kim J, Jeong HG, Kim DY, Noh YJ, et al. Solution-processable reduced graphene oxide as a novel alternative to PEDOT:PSS hole transport layers for highly efficient and stable polymer solar cells. Adv Mater 2011;23:4923–8.
[195] Zha ZB, Deng ZJ, Li YY, Li CH, Wang JR, Wang SM, et al. Biocompatible polypyrrole nanoparticles as a novel organic photoacoustic contrast agent for deep tissue imaging. Nanoscale 2013;5:4462–7.
[196] Cheng L, Yang K, Chen Q, Liu Z. Organic stealth nanoparticles for highly effective in vivo near-infrared photothermal therapy of cancer. ACS Nano 2012;6:5605–13.
[197] Lacerda L, Pastorin G, Wu W, Prato M, Bianco A, Kostarelos K. Luminescence of functionalized carbon nanotubes as a tool to monitor bundle formation and dissociation in water: the effect of plasmid-DNA complexation. Adv Func Mater 2006;16:1839–46.
[198] Lacerda L, Pastorin G, Gathercole D, Buddle J, Prato M, Bianco A, et al. Intracellular trafficking of carbon nanotubes by confocal laser scanning microscopy. Adv Mater 2007;19:1480.
[199] Cherukuri P, Bachilo SM, Litovsky SH, Weisman RB. Near-infrared fluorescence microscopy of single-walled carbon nanotubes in phagocytic cells. J Am Chem Soc 2004;126:15638–9.
[200] Welsher K, Liu Z, Sherlock SP, Robinson JT, Chen Z, Daranciang D, et al. A route to brightly fluorescent carbon nanotubes for near-infrared imaging in mice. Nat Nanotechnol 2009;4:773–80.
[201] Zhou FF, Wu SN, Yuan Y, Chen WR, Xing D. Mitochondria-targeting photoacoustic therapy using single-walled carbon nanotubes. Small 2012;8:1543–50.

[202] Lednev VN, Pershin SM, Obraztsova ED, Kudryashov SI, Bunkin AF. Single-shot and single-spot measurement of laser ablation threshold for carbon nanotubes. J Phys D Appl Phys 2013;46.

[203] Whitney J, DeWitt M, Whited BM, Carswell W, Simon A, Rylander CG, et al. 3D viability imaging of tumor phantoms treated with single-walled carbon nanohorns and photothermal therapy. Nanotechnology 2013;24.

[204] Heister E, Brunner EW, Dieckmann GR, Jurewicz I, Dalton AB. Are carbon nanotubes a natural solution? Applications in biology and medicine. ACS Appl Mater Interfaces 2013;5:1870–91.

[205] Murray AR, Kisin E, Leonard SS, Young SH, Kommineni C, Kagan VE, et al. Oxidative stress and inflammatory response in dermal toxicity of single-walled carbon nanotubes. Toxicology 2009;257:161–71.

[206] Monteiro-Riviere NA, Inman AO, Zhang LW. Limitations and relative utility of screening assays to assess engineered nanoparticle toxicity in a human cell line. Toxicol Appl Pharm 2009;234:222–35.

[207] Johnson JC, Yan HQ, Schaller RD, Petersen PB, Yang PD, Saykally RJ. Near-field imaging of nonlinear optical mixing in single zinc oxide nanowires. Nano Lett 2002;2:279–83.

[208] Hashimoto T, Yamada T, Yoko T. Third-order nonlinear optical properties of sol-gel derived alpha-Fe_2O_3, gamma-Fe_2O_3, and Fe_3O_4 thin films. J Appl Phys 1996;80:3184–90.

[209] Aouani H, Rahmani M, Navarro-Cia M, Maier SA. Third-harmonic-upconversion enhancement from a single semiconductor nanoparticle coupled to a plasmonic antenna. Nat Nanotechnol 2014;9:290–4.

[210] Rogov A, Mugnier Y, Bonacina L. Harmonic nanoparticles: noncentrosymmetric metal oxides for nonlinear optics. J Optics-Uk 2015;17.

[211] Cheng B, Shi WS, Russell-Tanner JM, Zhang L, Samulski ET. Synthesis of variable-aspect-ratio, single-crystalline ZnO nanostructures. Inorg Chem 2006;45:1208–14.

[212] Djurisic AB, Leung YH. Optical properties of ZnO nanostructures. Small 2006;2:944–61.

[213] Liu CW, Chang SJ, Brahma S, Hsiao CH, Chang FM, Wang PH, et al. Enhancement in the structure quality of ZnO nanorods by diluted Co dopants: analyses via optical second harmonic generation. J Appl Phys 2015;117.

[214] Liu WW, Wang K, Long H, Chu S, Wang B, Lu PX. Near-resonant second-order nonlinear susceptibility in c-axis oriented ZnO nanorods. Appl Phys Lett 2014;105.

[215] Lin CY, Liu TM, Chen CY, Huang YL, Huang WK, Sun CK, et al. Quantitative and qualitative investigation into the impact of focused ultrasound with microbubbles on the triggered release of nanoparticles from vasculature in mouse tumors. J Control Release 2010;146:291–8.

[216] Cao L, Wang X, Meziani MJ, Lu FS, Wang HF, Luo PJG, et al. Carbon dots for multiphoton bioimaging. J Am Chem Soc 2007;129:11318.

[217] Sandoval S, Yang J, Alfaro JG, Liberman A, Makale M, Chiang CE, et al. Europium-doped TiO_2 hollow nanoshells: two-photon imaging of cell binding. Chem Mater 2012;24:4222–30.

[218] Mayer L, Dantelle G, Jacques V, Perruchas S, Patriarche G, Roch JF, et al. Dual light-emitting nanoparticles: second harmonic generation combined with rare-earth photoluminescence. J Mater Chem C 2014;2:7681–6.

[219] Yao S, Belfield KD. Two-photon fluorescent probes for bioimaging. Eur J Org Chem 2012:3199–217.

[220] Liu F, Ding CQ, Jin M, Tian Y. A highly selective two-photon fluorescent probe for the determination of mercury ions. Analyst 2015;140:3285–9.

[221] Koo CK, Wong KL, Man CWY, Lam YW, So KY, Tam HL, et al. A bioaccumulative cyclometalated platinum(II) complex with two-photon-induced emission for live cell imaging. Inorg Chem 2009;48:872–8.

[222] Botchway SW, Charnley M, Haycock JW, Parker AW, Rochester DL, Weinstein JA, et al. Time-resolved and two-photon emission imaging microscopy of live cells with inert platinum complexes. Proc Natl Acad Sci USA 2008;105:16071–6.

[223] Hall MD, Amjadi S, Zhang M, Beale PJ, Hambley TW. The mechanism of action of platinum(IV) complexes in ovarian cancer cell lines. J Inorg Biochem 2004;98:1614–24.

[224] Min YZ, Mao CQ, Xu DC, Wang J, Liu YZ. Gold nanorods for platinum based prodrug delivery. Chem Commun 2010;46:8424–6.

[225] Ding D, Wang J, Zhu ZS, Li RT, Wu W, Liu BR, et al. Tumor accumulation, penetration, and antitumor response of cisplatin-loaded gelatin/poly(acrylic acid) nanoparticles. ACS Appl Mater Interfaces 2012;4:1838–46.

[226] Wu WC, Chen CY, Tian YQ, Jang SH, Hong YN, Liu Y, et al. Enhancement of aggregation-induced emission in dye-encapsulating polymeric micelles for bioimaging. Adv Func Mater 2010;20:1413–23.

[227] Ding D, Goh CC, Feng GX, Zhao ZJ, Liu J, Liu RR, et al. Ultrabright organic dots with aggregation-induced emission characteristics for real-time two-photon intravital vasculature imaging. Adv Mater 2013;25:6083–8.

[228] Kim S, Pudavar HE, Bonoiu A, Prasad PN. Aggregation-enhanced fluorescence in organically modified silica nanoparticles: a novel approach toward high-signal-output nanoprobes for two-photon fluorescence bioimaging. Adv Mater 2007;19:3791.

[229] Kim S, Ohulchanskyy TY, Pudavar HE, Pandey RK, Prasad PN. Organically modified silica nanoparticles co-encapsulating photosensitizing drug and aggregation-enhanced two-photon absorbing fluorescent dye aggregates for two-photon photodynamic therapy. J Am Chem Soc 2007;129:2669–75.

[230] Zhang XY, Zhang XQ, Yang B, Liu LJ, Hui JF, Liu MY, et al. Aggregation-induced emission dye based luminescent silica nanoparticles: facile preparation, biocompatibility evaluation and cell imaging applications. RSC Adv 2014;4:10060–6.

[231] Zhao QL, Li K, Chen SJ, Qin AJ, Ding D, Zhang S, et al. Aggregation-induced red-NIR emission organic nanoparticles as effective and photostable fluorescent probes for bioimaging. J Mater Chem 2012;22:15128–35.

[232] Qin W, Ding D, Liu JZ, Yuan WZ, Hu Y, Liu B, et al. Biocompatible nanoparticles with aggregation-induced emission characteristics as far-red/near-infrared fluorescent bioprobes for in vitro and in vivo imaging applications. Adv Func Mater 2012;22:771–9.

[233] Du CL, Wang AH, Fei JB, Zhao J, Li JB. Polypyrrole-stabilized gold nanorods with enhanced photothermal effect towards two-photon photothermal therapy. J Mater Chem B 2015;3:4539–45.

[234] Lim SF, Ryu WS, Austin RH. Particle size dependence of the dynamic photophysical properties of $NaYF_4$:Yb,Er nanocrystals. Opt Express 2010;18:2309–16.

[235] Schietinger S, Menezes LdS, Lauritzen Br, Benson O. Observation of size dependence in multicolor upconversion in single Yb^{3+}, Er^{3+} codoped $NaYF_4$ nanocrystals. Nano Lett 2009;9:2477–81.

[236] Zhang F, Li J, Shan J, Xu L, Zhao DY. Shape, size, and phase-controlled rare-earth fluoride nanocrystals with optical up-conversion properties. Chem-Eur J 2009;15:11010–9.

[237] Damasco JA, Chen G, Shao W, Agren H, Huang H, Song W, et al. Size-tunable and monodisperse Tm^{3+}/Gd^{3+}-doped hexagonal $NaYbF_4$ nanoparticles with engineered efficient near infrared-to-near infrared upconversion for in vivo imaging. ACS – Appl Mater Interfaces 2014;6:13884–93.

[238] Renero-Lecuna C, Martín-Rodríguez R, Valiente R, González J, Rodríguez F, Krämer KW, et al. Origin of the high upconversion green luminescence efficiency in β-$NaYF_4$:2%Er^{3+},20%Yb^{3+}. Chem Mater 2011;23:3442–8.

[239] Haase M, Schäfer H. Upconverting nanoparticles. Angew Chem Int Ed 2011;50:5808–29.

[240] Niu W, Wu S, Zhanga S. A facile and general approach for the multicolor tuning of lanthanide-ion doped $NaYF_4$ upconversion nanoparticles within a fixed composition. J Mater Chem 2010;20:9113–7.

[241] Cheng Q, Sui J, Cai W. Enhanced upconversion emission in Yb^{3+} and Er^{3+} codoped $NaGdF_4$ nanocrystals by introducing Li^+ ions. Nanoscale 2012;4:779–84.

[242] Ramasamy P, Chandra P, Rhee SW, Kim J. Enhanced upconversion luminescence in $NaGdF_4$:Yb,Er nanocrystals by Fe^{3+} doping and their application in bioimaging. Nanoscale 2013;5:8711–7.

[243] Li Z, Wang B, Xing L, Liu S, Tan N, Xiao S, et al. Enhancement of upconversion luminescence of $YAlO_3$:Er^{3+} by Gd^{3+} doping. Chin Opt Lett 2012;10:081602.

[244] Wang F, Liu X. Upconversion multicolor fine-tuning: visible to near-infrared emission from lanthanide-doped $NaYF_4$ nanoparticles. J Am Chem Soc 2008;130:5642–3.

[245] Qian HS, Zhang Y. Synthesis of hexagonal-phase core-shell NaYF$_4$ nanocrystals with tunable upconversion fluorescence. Langmuir: ACS J Surf Colloids 2008;24:12123–5.

[246] Dou Q, Idris NM, Zhang Y. Sandwich-structured upconversion nanoparticles with tunable color for multiplexed cell labeling. Biomaterials 2013;34:1722–31.

[247] Tian G, Gu Z, Zhou L, Yin W, Liu X, Yan L, et al. Mn^{2+} dopant-controlled synthesis of NaYF$_4$:Yb/Er upconversion nanoparticles for in vivo imaging and drug delivery. Adv Mater 2012;24:1226–31.

[248] Wang H, Lu W, Yi Z, Rao L, Zeng S, Li Z. Enhanced upconversion luminescence and single-band red emission of NaErF$_4$ nanocrystals via Mn^{2+} doping. J Alloy Compd 2015;618:776–80.

[249] Chen G, Liu H, Somesfalean G, Liang H, Zhang Z. Upconversion emission tuning from green to red in Yb^{3+}/Ho^{3+}-codoped NaYF$_4$ nanocrystals by tridoping with Ce^{3+} ions. Nanotechnology 2009;20:385704.

[250] Gao W, Zheng H, Han Q, He E, Gao F, Wanga R. Enhanced red upconversion luminescence by codoping Ce^{3+} in β-NaY(Gd$_{0.4}$)F$_4$:Yb^{3+}/Ho^{3+} nanocrystals. J Mater Chem C 2014;2:5327–34.

[251] Peng DF, Ju Q, Chen X, Ma RH, Chen B, Bai GX, et al. Lanthanide-doped energy cascade nanoparticles: full spectrum emission by single wavelength excitation. Chem Mater 2015;27:3115–20.

[252] Gerver RE, Gomez-Sjoberg R, Baxter BC, Thorn KS, Fordyce PM, Diaz-Botia CA, et al. Programmable microfluidic synthesis of spectrally encoded microspheres. Lab Chip 2012;12:4716–23.

[253] Bednarkiewicz A, Strek W. Interstitial single fiber multi-decay-probe for light dosimetry in photodynamic therapy: modelling. Proc SPIE 2005;5862:586210.

[254] Zhao JB, Lu ZD, Yin YD, Mcrae C, Piper JA, Dawes JM, et al. Upconversion luminescence with tunable lifetime in NaYF$_4$:Yb,Er nanocrystals: role of nanocrystal size. Nanoscale 2013;5:944–52.

[255] Lu YQ, Zhao JB, Zhang R, Liu YJ, Liu DM, Goldys EM, et al. Tunable lifetime multiplexing using luminescent nanocrystals. Nat Photonics 2014;8:33–7.

[256] Sun L-N, Peng H, Stich MIJ, Achatz D, Wolfbeis OS. pH sensor based on upconverting luminescent lanthanide nanorods. Chem Commun 2009:5000–2.

[257] Ali R, Saleh SM, Meier RJ, Azab HA, Abdelgawad II, Wolfbeis OS. Upconverting nanoparticle based optical sensor for carbon dioxide. Sens Actuators, B 2010;150:126–31.

[258] Mader HS, Wolfbeis OS. Optical ammonia sensor based on upconverting luminescent nanoparticles. Anal Chem 2010;82:5002–4.

[259] Liu Q, Peng JJ, Sun LN, Li FY. High-efficiency upconversion luminescent sensing and bioimaging of Hg(II) by chromophoric ruthenium complex-assembled nanophosphors. ACS Nano 2011;5:8040–8.

[260] Wang L, Li Y. Luminescent nanocrystals for nonenzymatic glucose concentration determination. Chem-Eur J 2007;13:4203–7.

[261] Liu J, Liu Y, Liu Q, Li C, Sun L, Li F. Iridium(III) complex-coated nanosystem for ratiometric upconversion luminescence bioimaging of cyanide anions. J Am Chem Soc 2011;133:15276–9.

[262] Mei QS, Li Y, Li BN, Zhang Y. Oxidative cleavage-based upconversional nanosensor for visual evaluation of antioxidant activity of drugs. Biosens Bioelectron 2015;64:88–93.

[263] Achatz DE, Ali R, Wolfbeis OS. Luminescent chemical sensing, biosensing, and screening using upconverting nanoparticles. In: Prodi L, Montalti M, Zaccheroni N, editors. Luminescence applied in sensor science. Berlin, Heidelberg: Springer; 2010. p. 29–50.

[264] Kang X, Cheng Z, Li C, Yang D, Shang M, Ma P, et al. Core–shell structured up-conversion luminescent and mesoporous NaYF$_4$:Yb^{3+}/Er^{3+}@nSiO$_2$@mSiO$_2$ nanospheres as carriers for drug delivery. J Phys Chem C 2011;115:15801–11.

[265] Prorok K, Bednarkiewicz A, Cichy B, Gnach A, Misiak M, Sobczyk M, et al. The impact of shell host (NaYF$_4$/CaF$_2$) and shell deposition methods on the up-conversion enhancement in Tb^{3+}, Yb^{3+} codoped colloidal alpha-NaYF$_4$ core-shell nanoparticles. Nanoscale 2014;6:1855–64.

[266] Arppe R, Hyppanen I, Perala N, Peltomaa R, Kaiser M, Wurth C, et al. Quenching of the upconversion luminescence of NaYF$_4$:Yb^{3+},Er^{3+} and NaYF$_4$:Yb^{3+}, Tm^{3+} nanophosphors by water: the role of the sensitizer Yb^{3+} in non-radiative relaxation. Nanoscale 2015;7:11746–57.

[267] Misiak M, Cichy B, Bednarkiewicz A, Strek W. Influence of Li$^+$ doping on up-conversion and structural properties of Yb^{3+}/Tm^{3+}-doped cubic NaYF$_4$ nanocrystals. J Lumin 2014;145:956–62.

[268] Li XM, Wang R, Zhang F, Zhou L, Shen DK, Yao C, et al. Nd^{3+} sensitized up/down converting dual-mode nanomaterials for efficient in-vitro and in-vivo bioimaging excited at 800 nm. Sci Rep-Uk 2013;3.

[269] Schietinger S, Aichele T, Wang HQ, Nann T, Benson O. Plasmon-enhanced upconversion in single NaYF$_4$:Yb^{3+}/Er^{3+} codoped nanocrystals. Nano Lett 2010;10:134–8.

[270] Zhang F, Haushalter RC, Haushalter RW, Shi YF, Zhang YC, Ding KL, et al. Rare-earth upconverting nanobarcodes for multiplexed biological detection. Small 2011;7:1972–6.

[271] Singh AK, Singh SK, Rai SB. Role of Li$^+$ ion in the luminescence enhancement of lanthanide ions: favorable modifications in host matrices. RSC Adv 2014;4:27039–61.

[272] Li XM, Shen DK, Yang JP, Yao C, Che RC, Zhang F, et al. Successive layer-by-layer strategy for multi-shell epitaxial growth: shell thickness and doping position dependence in upconverting optical properties. Chem Mater 2013;25:106–12.

[273] Wang J, Deng RR, MacDonald MA, Chen BL, Yuan JK, Wang F, et al. Enhancing multiphoton upconversion through energy clustering at sublattice level. Nat Mater 2014;13:157–62.

[274] Kwon OS, Song HS, Conde J, Kim HI, Artzi N, Kim JH. Dual-color emissive upconversion nanocapsules for differential cancer bioimaging in vivo. ACS Nano 2016;10:1512–21.

[275] Chen X, Peng D, Ju Q, Wang F. Photon upconversion in core-shell nanoparticles. Chem Soc Rev 2014.

[276] Liu G. Advances in the theoretical understanding of photon upconversion in rare-earth activated nanophosphors. Chem Soc Rev 2014.

[277] Tsang MK, Bai G, Hao J. Stimuli responsive upconversion luminescence nanomaterials and films for various applications. Chem Soc Rev 2014.

[278] Tu L, Liu X, Wu F, Zhang H. Excitation energy migration dynamics in upconversion nanomaterials. Chem Soc Rev 2014.

[279] Xu CT, Svenmarker P, Liu H, Wu X, Messing ME, Wallenberg LR, et al. High-resolution fluorescence diffuse optical tomography developed with nonlinear upconverting nanoparticles. ACS Nano 2012;6:4788–95.

[280] Dong H, Sun LD, Yan CH. Energy transfer in lanthanide upconversion studies for extended optical applications. Chem Soc Rev 2014.

[281] Idris NM, Jayakumar MK, Bansal A, Zhang Y. Upconversion nanoparticles as versatile light nanotransducers for photoactivation applications. Chem Soc Rev 2014.

[282] Li X, Zhang F, Zhao D. Lab on upconversion nanoparticles: optical properties and applications engineering via designed nanostructure. Chem Soc Rev 2014.

[283] Sun Y, Feng W, Yang P, Huang C, Li F. The biosafety of lanthanide upconversion nanomaterials. Chem Soc Rev 2014.

[284] Yang D, Ma P, Hou Z, Cheng Z, Li C, Lin J. Current advances in lanthanide ion (Ln)-based upconversion nanomaterials for drug delivery. Chem Soc Rev 2014.

[285] Zheng W, Huang P, Tu D, Ma E, Zhu H, Chen X. Lanthanide-doped upconversion nano-bioprobes: electronic structures, optical properties, and biodetection. Chem Soc Rev 2014.

[286] Zhou L, Zheng X, Gu Z, Yin W, Zhang X, Ruan L, et al. Mesoporous NaYbF$_4$@NaGdF$_4$ core-shell up-conversion nanoparticles for targeted drug delivery and multimodal imaging. Biomaterials 2014;35:7666–78.

[287] Gnach A, Lipinski T, Bednarkiewicz A, Rybka J, Capobianco J. Upconverting nanoparticles: assessing the toxicity. Chem Soc Rev 2015.

[288] Gnach A, Bednarkiewicz A. Lanthanide-doped up-converting nanoparticles: merits and challenges. Nano Today 2012;7:532–63.

[289] Petoral RM, Söderlind F, Klasson A, Suska A, Fortin MA, Abrikossova N, et al. Synthesis and characterization of Tb^{3+}-doped Gd$_2$O$_3$ nanocrystals: a bifunctional material with combined fluorescent labeling and MRI contrast agent properties. J Phys Chem C 2009;113:6913–20.

[290] Ju Q, Tu D, Liu Y, Li R, Zhu H, Chen J, et al. Amine-functionalized lanthanide-doped KGdF$_4$ nanocrystals as potential optical/magnetic multimodal bioprobes. J Am Chem Soc 2011;134:1323–30.
[291] Xing H, Bu W, Zhang S, Zheng X, Li M, Chen F, et al. Multifunctional nanoprobes for upconversion fluorescence, MR and CT trimodal imaging. Biomaterials 2012;33:1079–89.
[292] Kumar R, Nyk M, Ohulchanskyy TY, Flask CA, Prasad PN. Combined optical and MR bioimaging using rare earth ion doped NaYF$_4$ nanocrystals. Adv Func Mater 2009;19:853–9.
[293] Zhou J, Yu M, Sun Y, Zhang X, Zhu X, Wu Z, et al. Fluorine-18-labeled Gd^{3+}/Yb^{3+}/Er^{3+} co-doped NaYF$_4$ nanophosphors for multimodality PET/MR/UCL imaging. Biomaterials 2011;32:1148–56.
[294] Liu Q, Sun Y, Li C, Zhou J, Li C, Yang T, et al. ^{18}F-labeled magnetic-upconversion nanophosphors via rare-earth cation-assisted ligand assembly. ACS Nano 2011;5:3146–57.
[295] Xia A, Zhang X, Zhang J, Deng Y, Chen Q, Wu S, et al. Enhanced dual contrast agent, Co^{2+}-doped NaYF$_4$:Yb^{3+},Tm^{3+} nanorods, for near infrared-to-near infrared upconversion luminescence and magnetic resonance imaging. Biomaterials. Biomaterials 2014;35:9167–76.
[296] Xia A, Gao Y, Zhou J, Li CY, Yang TS, Wu DM, et al. Core-shell NaYF$_4$:Yb^{3+},Tm^{3+}@Fe$_x$O$_y$ nanocrystals for dual-modality T(2)-enhanced magnetic resonance and NIR-to-NIR upconversion luminescent imaging of small-animal lymphatic node. Biomaterials 2011;32:7200–8.
[297] Zhou J, Sun Y, Du X, Xiong L, Hu H, Li F. Dual-modality in vivo imaging using rare-earth nanocrystals with near-infrared to near-infrared (NIR-to-NIR) upconversion luminescence and magnetic resonance properties. Biomaterials 2010;31:3287–95.
[298] Yin W, Zhou L, Gu Z, Tian G, Jin S, Yan L, et al. Lanthanide-doped GdVO$_4$ upconversion nanophosphors with tunable emissions and their applications for biomedical imaging. J Mater Chem 2012;22:6974–81.
[299] Xia A, Chen M, Gao Y, Wu D, Feng W, Li F. Gd^{3+} complex-modified NaLuF$_4$-basedupconversion nanophosphors for trimodality imaging of NIR-to-NIR upconversion luminescence, X-ray computed tomography and magnetic resonance. Biomaterials 2012;33:5394–405.
[300] Wang C, Cheng L, Xu H, Liu Z. Towards whole-body imaging at the single cell level using ultra-sensitive stem cell labeling with oligo-arginine modified upconversion nanoparticles. Biomaterials 2012;33:4872–81.
[301] Idris NM, Li Z, Ye L, Wei Sim EK, Mahendran R, Ho PC-L, et al. Tracking transplanted cells in live animal using upconversion fluorescent nanoparticles. Biomaterials 2009;30:5104–13.
[302] Bednarkiewicz A, Wawrzynczyk D, Nyk M, Strek W. Synthesis and spectral properties of colloidal Nd^{3+} doped NaYF$_4$ nanocrystals. Opt Mater 2011;33:1481–6.
[303] Bednarkiewicz A, Wawrzynczyk D, Nyk M, Strek W. Optically stimulated heating using Nd^{3+} doped NaYF$_4$ colloidal near infrared nanophosphors. Appl Phys B: Lasers Opt 2011;103:847–52.
[304] Qian LP, Zhou LH, Too H-P, Chow G-M. Gold decorated NaYF$_4$:Yb,Er/NaYF$_4$/silica (core/shell/shell) upconversion nanoparticles for photothermal destruction of BE(2)-C neuroblastoma cells. J Nanopart Res 2010;13:499–510.
[305] Cheng L, Yang K, Li Y, Chen J, Wang C, Shao M, et al. Facile preparation of multifunctional upconversion nanoprobes for multimodal imaging and dual-targeted photothermal therapy. Angew Chem Int Ed 2011;50:7385–90.
[306] Cheng L, Yang K, Li Y, Zeng X, Shao M, Lee S-T, et al. Multifunctional nanoparticles for upconversion luminescence/MR multimodal imaging and magnetically targeted photothermal therapy. Biomaterials 2012;33:2215–22.
[307] Wang C, Cheng L, Liu Z. Drug delivery with upconversion nanoparticles for multi-functional targeted cancer cell imaging and therapy. Biomaterials 2011;32:1110–20.
[308] Shan J, Budijono SJ, Hu G, Yao N, Kang Y, Ju Y, et al. Pegylated composite nanoparticles containing upconverting phosphors and meso-tetraphenyl porphine (TPP) for photodynamic therapy. Adv Func Mater 2011;21:2488–95.
[309] Qian HS, Guo HC, Ho PCL, Mahendran R, Zhang Y. Mesoporous-silica-coated up-conversion fluorescent nanoparticles for photodynamic therapy. Small 2009;5:2285–90.
[310] Chatterjee DK, Yong Z. Upconverting nanoparticles as nanotransducers for photodynamic therapy in cancer cells. Nanomedicine (Philadelphia, PA, US) 2008;3:73–82.
[311] Zhou A, Wei Y, Wu B, Chen Q, Xing D. Pyropheophorbide A and c(RGDyK) comodified chitosan-wrapped upconversion nanoparticle for targeted near-infrared photodynamic therapy. Mol Pharm 2012;9:1580–9.
[312] Zhao Z, Han Y, Lin C, Hu D, Wang F, Chen X, et al. Multifunctional core–shell upconverting nanoparticles for imaging and photodynamic therapy of liver cancer cells. Chem-Asia J 2012;7:830–7.
[313] Cui S, Chen H, Zhu H, Tian J, Chi X, Qian Z, et al. Amphiphilic chitosan modified upconversion nanoparticles for in vivo photodynamic therapy induced by near-infrared light. J Mater Chem 2012;22:4861–73.
[314] Yang Y, Qu Y, Zhao J, Zeng Q, Ran Y, Zhang Q, et al. Fabrication of and drug delivery by an upconversion emission nanocomposite with monodisperse LaF$_3$:Yb,Er core/mesoporous silica shell structure. Eur J Inorg Chem 2010;2010:5195–9.
[315] Deng RR, Xie XJ, Vendrell M, Chang YT, Liu XG. Intracellular glutathione detection using MnO$_2$-nanosheet-modified upconversion nanoparticles. J Am Chem Soc 2011;133:20168–71.
[316] Xiong LQ, Chen ZG, Tian QW, Cao TY, Xu CJ, Li FY. High contrast upconversion luminescence targeted imaging in vivo using peptide-labeled nanophosphors. Anal Chem 2009;81:8687–94.
[317] Ungun B, Prud'homme RK, Budijono SJ, Shan JN, Lim SF, Ju YG, et al. Nanofabricated upconversion nanoparticles for photodynamic therapy. Opt Express 2009;17:80–6.
[318] Cui SS, Chen HY, Zhu HY, Tian JM, Chi XM, Qian ZY, et al. Amphiphilic chitosan modified upconversion nanoparticles for in vivo photodynamic therapy induced by near-infrared light. J Mater Chem 2012;22:4861–73.
[319] Dou QQ, Rengaramchandran A, Selvan ST, Paulmurugan R, Zhang Y. Core-shell upconversion nanoparticle-semiconductor heterostructures for photodynamic therapy. Sci Rep-Uk 2015;5.
[320] Zhou B, Shi BY, Jin DY, Liu XG. Controlling upconversion nanocrystals for emerging applications. Nat Nanotechnol 2015;10:924–36.
[321] Chen GY, Qiu HL, Prasad PN, Chen XY. Upconversion nanoparticles: design, nanochemistry, and applications in theranostics. Chem Rev 2014;114:5161–214.
[322] Gibbs WW. Untangling the roots of cancer. Sci Am 2003;289:56–65.
[323] Boyle FT, Costello GF. Cancer therapy: a move to the molecular level. Chem Soc Rev 1998;27:251–61.
[324] Mayo GL, Melendez RF, Kumar N, McKinnon SJ, Glickman RD. Antibody-targeted photodynamic therapy. Am J Ophthalmol 2003;136:1151–2.
[325] Scott AM, Wolchok JD, Old LJ. Antibody therapy of cancer. Nat Rev Cancer 2012;12:278–87.
[326] Vanneman M, Dranoff G. Combining immunotherapy and targeted therapies in cancer treatment. Nat Rev Cancer 2012;12:237–51.
[327] Sharman WM, van Lier JE, Allen CM. Targeted photodynamic therapy via receptor mediated delivery systems. Adv Drug Deliv Rev 2004;56:53–76.
[328] Zhang Y, Zhang Y, Hong G, He W, Zhou K, Yang K, et al. Biodistribution, pharmacokinetics and toxicology of Ag$_2$S near-infrared quantum dots in mice. Biomaterials 2013;34:3639–46.
[329] Charan S, Sanjiv K, Singh N, Chien FC, Chen YF, Nergui NN, et al. Development of chitosan oligosaccharide-modified gold nanorods for in vivo targeted delivery and noninvasive imaging by NIR irradiation. Bioconjug Chem 2012;23:2173–82.
[330] Niidome T, Yamagata M, Okamoto Y, Akiyama Y, Takahashi H, Kawano T, et al. PEG-modified gold nanorods with a stealth character for in vivo applications. J Control Release: Off J Control Release Soc 2006;114:343–7.
[331] Hirsch LR, Stafford RJ, Bankson JA, Sershen SR, Rivera B, Price RE, et al. Nanoshell-mediated near-infrared thermal therapy of tumors under magnetic resonance guidance. Proc Natl Acad Sci USA 2003;100:13549–54.
[332] Smitha Rao CH, Tata Uday, Wu Peter, Arora Nikhil, Ahn Jinsung, Lin Victor K, et al. Evaluation of cytotoxic effects of different concentrations of porous hollow Au nanoparticles (PHAuNPs) on cells. J Nanotechnol 2014;2014:7.

[333] Leung JP, Wu S, Chou KC, Signorell R. Investigation of sub-100 nm gold nanoparticles for laser-induced thermotherapy of cancer. Nanomater-Basel 2013;3:86–106.
[334] Loo C, Lowery A, Halas N, West J, Drezek R. Immunotargeted nanoshells for integrated cancer imaging and therapy. Nano Lett 2005;5:709–11.
[335] Au L, Zhang Q, Cobley CM, Gidding M, Schwartz AG, Chen JY, et al. Quantifying the cellular uptake of antibody-conjugated au nanocages by two-photon microscopy and inductively coupled plasma mass spectrometry. ACS Nano 2010;4:35–42.
[336] Wang Y, Liu Y, Luehmann H, Xia X, Wan D, Cutler C, et al. Radioluminescent gold nanocages with controlled radioactivity for real-time in vivo imaging. Nano Lett 2013;13:581–5.
[337] Tang SH, Chen M, Zheng NF. Multifunctional ultrasmall Pd nanosheets for enhanced near-infrared photothermal therapy and chemotherapy of cancer. Nano Res 2015;8:165–74.
[338] Nie LM, Chen M, Sun XL, Rong PF, Zheng NF, Chen XY. Palladium nanosheets as highly stable and effective contrast agents for in vivo photoacoustic molecular imaging. Nanoscale 2014;6:1271–6.
[339] Ziemer LS, Lee WMF, Vinogradov SA, Sehgal C, Wilson DF. Oxygen distribution in murine tumors: characterization using oxygen-dependent quenching of phosphorescence. J Appl Physiol 2005;98:1503–10.
[340] Vinogradov SA, Lo LW, Jenkins WT, Evans SM, Koch C, Wilson DF. Noninvasive imaging of the distribution in oxygen in tissue in vivo using near-infrared phosphors. Biophys J 1996;70:1609–17.
[341] Chi Y, Chou PT. Contemporary progresses on neutral, highly emissive Os(II) and Ru(II) complexes. Chem Soc Rev 2007;36:1421–31.
[342] Chi Y, Chou PT. Transition-metal phosphors with cyclometalating ligands: fundamentals and applications. Chem Soc Rev 2010;39:638–55.
[343] Quaranta M, Borisov SM, Klimant I. Indicators for optical oxygen sensors. Bioanal Rev 2012;4:115–57.
[344] Helmlinger G, Yuan F, Dellian M, Jain RK. Interstitial pH and pO_2 gradients in solid tumors in vivo: high-resolution measurements reveal a lack of correlation. Nat Med 1997;3:177–82.
[345] Morris KJ, Roach MS, Xu W, Demas JN, DeGraff BA. Luminescence lifetime standards for the nanosecond to microsecond range and oxygen quenching of ruthenium(II) complexes. Anal Chem 2007;79:9310–4.
[346] Zhang SJ, Hosaka M, Yoshihara T, Negishi K, Iida Y, Tobita S, et al. Phosphorescent light-emitting iridium complexes serve as a hypoxia-sensing probe for tumor imaging in living animals. Can Res 2010;70:4490–8.
[347] Finikova OS, Lebedev AY, Aprelev A, Troxler T, Gao F, Garnacho C, et al. Oxygen microscopy by two-photon-excited phosphorescence. ChemPhysChem 2008;9:1673–9.
[348] Martin GR, Jain RK. Noninvasive measurement of interstitial Ph profiles in normal and neoplastic tissue using fluorescence ratio imaging microscopy. Can Res 1994;54:5670–4.
[349] Anderson M, Moshnikova A, Engelman DM, Reshetnyak YK, Andreev OA. Probe for the measurement of cell surface pH in vivo and ex vivo. Proc Natl Acad Sci USA 2016;113:8177–81.
[350] Li C, Xia JA, Wei XB, Yan HH, Si Z, Ju SH. PH-activated near-infrared fluorescence nanoprobe imaging tumors by sensing the acidic microenvironment. Adv Func Mater 2010;20:2222–30.
[351] Yuan F, Dellian M, Fukumura D, Leunig M, Berk DA, Torchilin VP, et al. Vascular-permeability in a human tumor xenograft – molecular-size dependence and cutoff size. Can Res 1995;55:3752–6.
[352] Dreher MR, Liu WG, Michelich CR, Dewhirst MW, Yuan F, Chilkoti A. Tumor vascular permeability, accumulation, and penetration of macromolecular drug carriers. J Natl Cancer Inst 2006;98:335–44.
[353] Egawa G, Nakamizo S, Natsuaki Y, Doi H, Miyachi Y, Kabashima K. Intravital analysis of vascular permeability in mice using two-photon microscopy. Sci Rep-Uk 2013;3.
[354] Niedbala RS, Feindt H, Kardos K, Vail T, Burton J, Bielska B, et al. Detection of analytes by immunoassay using up-converting phosphor technology. Anal Biochem 2001;293:22–30.
[355] Hampl J, Hall M, Mufti NA, Yao YM, MacQueen DB, Wright WH, et al. Upconverting phosphor reporters in immunochromatographic assays. Anal Biochem 2001;288:176–87.
[356] van de Rijke F, Zijlmans H, Li S, Vail T, Raap AK, Niedbala RS, et al. Up-converting phosphor reporters for nucleic acid microarrays. Nat Biotechnol 2001;19:273–6.
[357] Ylihärsilä M, Valta T, Karp M, Hattara L, Harju E, Hölsä J, et al. Oligonucleotide array-in-well platform for detection and genotyping human adenoviruses by utilizing upconverting phosphor label technology. Anal Chem 2011;83:1456–61.
[358] Rantanen T, Järvenpää M-L, Vuojola J, Kuningas K, Soukka T. Fluorescence-quenching-based enzyme-activity assay by using photon upconversion. Angew Chem Int Ed 2008;47:3811–3.
[359] Kim G, Lee YEK, Xu H, Philbert MA, Kopelman R. Nanoencapsulation method for high selectivity sensing of hydrogen peroxide inside live cells. Anal Chem 2010;82:2165–9.
[360] Cao YF, Koo YEL, Koo SM, Kopelman R. Ratiometric singlet oxygen nano-optodes and their use for monitoring photodynamic therapy nanoplatforms. Photochem Photobiol 2005;81:1489–98.
[361] Kim SH, Kim B, Yadavalli VK, Pishko MV. Encapsulation of enzymes within polymer spheres to create optical nanosensors for oxidative stress. Anal Chem 2005;77:6828–33.
[362] Kim JY, Il Choi W, Kim YH, Tae G. Highly selective in-vivo imaging of tumor as an inflammation site by ROS detection using hydrocyanine-conjugated, functional nano-carriers. J Control Release 2011;156:398–405.
[363] Wen F, Dong YH, Feng L, Wang S, Zhang SC, Zhang XR. Horseradish peroxidase functionalized fluorescent gold nanoclusters for hydrogen peroxide sensing. Anal Chem 2011;83:1193–6.
[364] Shiang YC, Huang CC, Chang HT. Gold nanodot-based luminescent sensor for the detection of hydrogen peroxide and glucose. Chem Commun 2009:3437–9.
[365] Gao L, Jin L, Xue P, Xu J, Wang Y, Ma H, et al. Reconstruction of complementary images in second harmonic generation microscopy. Opt Express 2006;14:4727–35.
[366] Huang CC, Liu TM. Controlled Au-polymer nanostructures for multiphoton imaging, prodrug delivery, and chemo-photothermal therapy platforms. ACS Appl Mater Interfaces 2015;7:25259–69.
[367] Vahrmeijer AL, Hutteman M, van der Vorst JR, van de Velde CJH, Frangioni JV. Image-guided cancer surgery using near-infrared fluorescence. Nat Rev Clin Oncol 2013;10:507–18.
[368] Verbeek FPR, Troyan SL, Mieog JSD, Liefers GJ, Moffitt LA, Rosenberg M, et al. Near-infrared fluorescence sentinel lymph node mapping in breast cancer: a multicenter experience. Breast Cancer Tr 2014;143:333–42.
[369] Kim S, Lim YT, Soltesz EG, De Grand AM, Lee J, Nakayama A, et al. Near-infrared fluorescent type II quantum dots for sentinel lymph node mapping. Nat Biotechnol 2004;22:93–7.
[370] Nakajima M, Takeda M, Kobayashi M, Suzuki S, Ohuchi N. Nano-sized fluorescent particles as new tracers for sentinel node detection: experimental model for decision of appropriate size and wavelength. Cancer Sci 2005;96:353–6.
[371] Akers WJ, Kim C, Berezin M, Guo K, Fuhrhop R, Lanza GM, et al. Noninvasive photoacoustic and fluorescence sentinel lymph node identification using dye-loaded perfluorocarbon nanoparticles. ACS Nano 2011;5:173–82.
[372] Pu KY, Shuhendler AJ, Jokerst JV, Mei JG, Gambhir SS, Bao ZN, et al. Semiconducting polymer nanoparticles as photoacoustic molecular imaging probes in living mice. Nat Nanotechnol 2014;9:233–9.
[373] Nguyen QT, Tsien RY. Fluorescence-guided surgery with live molecular navigation – a new cutting edge. Nat Rev Cancer 2013;13:653–62.
[374] Stummer W, Pichlmeier U, Meinel T, Wiestler OD, Zanella F, Hans-Jurgen R, et al. Fluorescence-guided surgery with 5-aminolevulinic acid for resection of malignant glioma: a randomised controlled multicentre phase III trial. Lancet Oncol 2006;7:392–401.

[375] Nguyen QT, Olson ES, Aguilera TA, Jiang T, Scadeng M, Ellies LG, et al. Surgery with molecular fluorescence imaging using activatable cell-penetrating peptides decreases residual cancer and improves survival. Proc Natl Acad Sci USA 2010;107:4317–22.

[376] Whitney MA, Crisp JL, Nguyen LT, Friedman B, Gross LA, Steinbach P, et al. Fluorescent peptides highlight peripheral nerves during surgery in mice. Nat Biotechnol 2011;29. 352-U181.

[377] Philip AK, Philip B. Colon targeted drug delivery systems: a review on primary and novel approaches. Oman Med J 2010;25:79–87.

[378] Mitragotri S. Innovation – healing sound: the use of ultrasound in drug delivery and other therapeutic applications. Nat Rev Drug Discov 2005;4:255–60.

[379] Liu HL, Fan CH, Ting CY, Yeh CK. Combining microbubbles and ultrasound for drug delivery to brain tumors: current progress and overview. Theranostics 2014;4:432–44.

[380] Hu SH, Chen SY, Liu DM, Hsiao CS. Core/single-crystal-shell nanospheres for controlled drug release via a magnetically triggered rupturing mechanism. Adv Mater 2008;20:2690.

[381] Timko BP, Dvir T, Kohane DS. Remotely triggerable drug delivery systems. Adv Mater 2010;22:4925–43.

[382] Sun XQ, Wang C, Gao M, Hu AY, Liu Z. Remotely controlled red blood cell carriers for cancer targeting and near-infrared light-triggered drug release in combined photothermal-chemotherapy. Adv Func Mater 2015;25:2386–94.

[383] Park C, Lim J, Yun M, Kim C. Photoinduced release of guest molecules by supramolecular transformation of self-assembled aggregates derived from dendrons. Angew Chem – Int Ed 2008;47:2959–63.

[384] Banerjee SS, Chen DH. A multifunctional magnetic nanocarrier bearing fluorescent dye for targeted drug delivery by enhanced two-photon triggered release. Nanotechnology 2009;20.

[385] Kocer A, Walko M, Meijberg W, Feringa BL. A light-actuated nanovalve derived from a channel protein. Science 2005;309:755–8.

[386] Bult H, Boeckxstaens GE, Pelckmans PA, Jordaens FH, Vanmaercke YM, Herman AG. Nitric-oxide as an inhibitory nonadrenergic noncholinergic neurotransmitter. Nature 1990;345:346–7.

[387] He SQ, Krippes K, Ritz S, Chen ZJ, Best A, Butt HJ, et al. Ultralow-intensity near-infrared light induces drug delivery by upconverting nanoparticles. Chem Commun 2015;51:431–4.

[388] Tong R, Hemmati HD, Langer R, Kohane DS. Photoswitchable nanoparticles for triggered tissue penetration and drug delivery. J Am Chem Soc 2012;134:8848–55.

[389] Vijayaraghavan P, Liu CH, Vankayala R, Chiang CS, Hwang KC. Designing multi-branched gold nanoechinus for NIR light activated dual modal photodynamic and photothermal therapy in the second biological window. Adv Mater 2014;26:6689–95.

[390] Kam NWS, O'Connell M, Wisdom JA, Dai H. Carbon nanotubes as multifunctional biological transporters and near-infrared agents for selective cancer cell destruction. Proc Natl Acad Sci 2005;102:11600–5.

[391] Wang CH, Chiou SH, Chou CP, Chen YC, Huang YJ, Peng CA. Photothermolysis of glioblastoma stem-like cells targeted by carbon nanotubes conjugated with CD133 monoclonal antibody. Nanomed – Nanotechnol Biol Med 2011;7:69–79.

[392] Xu WJ, Meng ZQ, Yu N, Chen ZG, Sun B, Jiang XZ, et al. PEGylated Cs_xWO_3 nanorods as an efficient and stable 915 nm-laser-driven photothermal agent against cancer cells. RSC Adv 2015;5:7074–82.

[393] Chen ZG, Wang Q, Wang HL, Zhang LS, Song GS, Song LL, et al. Ultrathin PEGylated $W_{18}O_{49}$ nanowires as a new 980 nm-laser-driven photothermal agent for efficient ablation of cancer cells in vivo. Adv Mater 2013;25:2095–100.

[394] Huo D, He J, Li H, Huang AJ, Zhao HY, Ding Y, et al. X-ray CT guided fault-free photothermal ablation of metastatic lymph nodes with ultrafine HER-2 targeting $W_{18}O_{49}$ nanoparticles. Biomaterials 2014;35:9155–66.

[395] Roti JLR. Cellular responses to hyperthermia (40–46 degrees C): cell killing and molecular events. Int J Hyperther 2008;24:3–15.

[396] Habash RW, Bansal R, Krewski D, Alhafid HT. Thermal therapy, part 1: an introduction to thermal therapy. Crit Rev Biomed Eng 2006;34:459–89.

[397] Johannsen M, Gneveckow U, Eckelt L, Feussner A, Waldofner N, Scholz R, et al. Clinical hyperthermia of prostate cancer using magnetic nanoparticles: presentation of a new interstitial technique. Int J Hyperther 2005;21:637–47.

[398] Song CW. Effect of local hyperthermia on blood-flow and microenvironment – a review. Can Res 1984;44:4721–30.

[399] Akkus O, Rimnac CM. Cortical bone tissue resists fatigue fracture by deceleration and arrest of microcrack growth. J Biomech 2001;34:757–64.

[400] Zhou ZG, Kong B, Yu C, Shi XY, Wang MW, Liu W, et al. Tungsten oxide nanorods: an efficient nanoplatform for tumor CT imaging and photothermal therapy. Sci Rep-Uk 2014;4.

[401] Melamed JR, Edelstein RS, Day ES. Elucidating the fundamental mechanisms of cell death triggered by photothermal therapy. ACS Nano 2015;9:6–11.

[402] Jaque D, Maestro LM, del Rosal B, Haro-Gonzalez P, Benayas A, Plaza JL, et al. Nanoparticles for photothermal therapies. Nanoscale 2014;6:9494–530.

[403] Wawrzynczyk D, Bednarkiewicz A, Nyk M, Strek W, Samoc M. Neodymium(III) doped fluoride nanoparticles as non-contact optical temperature sensors. Nanoscale 2012;4:6959–61.

[404] Liu TM, Conde J, Lipiński T, Bednarkiewicz A, Huang CC. Revisiting the classification of NIR-absorbing/emitting nanomaterials for in vivo bioapplications. NPG Asia Mater 2016;8.

[405] Dolmans DEJGJ, Fukumura D, Jain RK. Photodynamic therapy for cancer. Nat Rev Cancer 2003;3:380–7.

[406] Castano AP, Mroz P, Hamblin MR. Photodynamic therapy and anti-tumour immunity. Nat Rev Cancer 2006;6:535–45.

[407] Dougherty TJ, Gomer CJ, Henderson BW, Jori G, Kessel D, Korbelik M, et al. Photodynamic therapy. J Natl Cancer Inst 1998;90:889–905.

[408] Moor ACE. Signaling pathways in cell death and survival after photodynamic therapy. J Photochem Photobiol B 2000;57:1–13.

[409] Wilson BC. Photodynamic therapy for cancer: principles. Can J Gastroenterol 2002;16:393–6.

[410] Moghissi K. Photodynamic therapy for lung cancer 30 years on. Photodiagn Photodynam 2013;10:95.

[411] Usuda J, Inoue T, Ohtani K, Honda H, Ohira T, Tsuboi M, et al. New era of photodynamic therapy for lung cancer using photofrin and NPe6. Lung Cancer 2005;49. S163-S.

[412] Noorullah O, Lekahraju P, Povalarapu N, Kapoor N. Comparison of costs of photodynamic therapy and radiofrequency ablation for management of dysplasia in Barrett's oesophagus: the Aintree experience. Gut 2011;60. A33-U1455.

[413] Nava HR, Allamaneni SS, Cooper MT, Dougherty T, Wilding GE, Henderson BW. A phase I/II study of photodynamic therapy (PDT) using HPPH for the treatment of Barrett's and precancerous lesions of the esophagus. J Clin Oncol 2010;28.

[414] Spechler SJ, Souza RF. Biomarkers and photodynamic therapy for Barrett's esophagus: time to FISH or cut bait? Gastroenterology 2008;135:354–7.

[415] Senior K. Photodynamic therapy for bladder cancer. Lancet Oncol 2005;6:546.

[416] Briggs C, Shackley DC, Gilhooley A, Whitehurst A, Moore JV, Betts CD, et al. Photodynamic therapy for superficial bladder cancer under local anaesthetic. Brit J Cancer 2001;85:53.

[417] Biel M. Advances in photodynamic therapy for the treatment of head and neck cancers. Laser Surg Med 2006;38:349–55.

[418] Anand S, Atanaskova N, Wilson C, Hasan T, Maytin EV. Enhancement of protoporphyrin IX and suppression of ferrochelatase levels by Vitamin D in tumor models of nonmelanoma skin cancer: implications for tumor response to photodynamic therapy. J Invest Dermatol 2010;130. S137-S.

[419] de Felicio LBA, Ferreira J, Bentley MVB, Bagnato VS, Tedesco CA, Souza CD. Topical 5-aminolevulinic acid photodynamic therapy as a treatment modality for nonmelanoma skin cancer. An Bras Dermatol 2008;83:309–16.

[420] Szeimies RM, Morton CA, Sidoroff A, Braathen LR. Photodynamic therapy for non-melanoma skin cancer. Acta Derm-Venereol 2005;85:483–90.

[421] Csaky KG, Grp C-PS. Phase II trial of Celebrex in photodynamic therapy (c-PDT) for neovascular age-related macular degeneration (AMD): rationale and baseline characteristics. Invest Ophth Vis Sci 2005;46.

[422] Nakonechny F, Firer MA, Nitzan Y, Nisnevitch M. Intracellular antimicrobial photodynamic therapy: a novel technique for efficient eradication of pathogenic bacteria. Photochem Photobiol 2010;86:1350–5.

[423] Sternberg ED, Dolphin D, Bruckner C. Porphyrin-based photosensitizers for use in photodynamic therapy. Tetrahedron 1998;54:4151–202.

[424] Yoon I, Li JZ, Shim YK. Advance in photosensitizers and light delivery for photodynamic therapy. Clin Endosc 2013;46:7–23.

[425] Wang C, Tao HQ, Cheng L, Liu Z. Near-infrared light induced in vivo photodynamic therapy of cancer based on upconversion nanoparticles. Biomaterials 2011;32:6145–54.
[426] Shan JN, Budijono SJ, Hu GH, Yao N, Kang YB, Ju YG, et al. Pegylated composite nanoparticles containing upconverting phosphors and meso-tetraphenyl porphine (TPP) for photodynamic therapy. Adv Func Mater 2011;21:2488–95.
[427] Zhang P, Steelant W, Kumar M, Scholfield M. Versatile photosensitizers for photodynamic therapy at infrared excitation. J Am Chem Soc 2007;129:4526.
[428] Chatterjee DK, Yong Z. Upconverting nanoparticles as nanotransducers for photodynamic therapy in cancer cells. Nanomed-Uk 2008;3:73–82.
[429] Wang F, Sun LD, Gu J, Wang YF, Feng W, Yang Y, et al. Selective heteroepitaxial nanocrystal growth of rare earth fluorides on sodium chloride: synthesis and density functional calculations. Angew Chem – Int Ed 2012;51:8796–9.
[430] Wang D, Xue B, Kong X, Tu L, Liu X, Zhang Y, et al. 808 nm driven Nd^{3+}-sensitized upconversion nanostructures for photodynamic therapy and simultaneous fluorescence imaging. Nanoscale 2014;7:190–7.
[431] Kim JY, Choi WI, Kim M, Tae G. Tumor-targeting nanogel that can function independently for both photodynamic and photothermal therapy and its synergy from the procedure of PDT followed by PTT. J Control Release 2013;171:113–21.
[432] Fan Z, Dai X, Lu Y, Yu E, Brahmbatt N, Carter N, et al. Enhancing targeted tumor treatment by near IR light-activatable photodynamic-photothermal synergistic therapy. Mol Pharm 2014;11:1109–16.
[433] Zhang D, Wu M, Zeng YY, Wu LJ, Wang QT, Han X, et al. Chlorin e6 conjugated poly(dopamine) nanospheres as PDT/PTT dual-modal therapeutic agents for enhanced cancer therapy. ACS Appl Mater Interfaces 2015;7:8176–87.
[434] Yan XF, Niu G, Lin J, Jin AJ, Hu H, Tang YX, et al. Enhanced fluorescence imaging guided photodynamic therapy of sinoporphyrin sodium loaded graphene oxide. Biomaterials 2015;42:94–102.
[435] Yan XF, Hu H, Lin J, Jin AJ, Niu G, Zhang SL, et al. Optical and photoacoustic dual-modality imaging guided synergistic photodynamic/photothermal therapies. Nanoscale 2015;7:2520–6.
[436] Wang NN, Zhao ZL, Lv YF, Fan HH, Bai HR, Meng HM, et al. Gold nanorod-photosensitizer conjugate with extracellular pH-driven tumor targeting ability for photothermal/photodynamic therapy. Nano Res 2014;7:1291–301.
[437] Yong Y, Zhou LJ, Gu ZJ, Yan L, Tian G, Zheng XP, et al. WS2 nanosheet as a new photosensitizer carrier for combined photodynamic and photothermal therapy of cancer cells. Nanoscale 2014;6:10394–403.
[438] Oh J, Yoon HJ, Park JH. Plasmonic liposomes for synergistic photodynamic and photothermal therapy. J Mater Chem B 2014;2:2592–7.
[439] Huang CC, Lin PH, Lee CW. OFF/ON galvanic replacement reaction for preparing divergent AuAg nano-hollows as a SERS-visualized drug delivery system in targeted photodynamic therapy. RSC Adv 2016;6:64494–8.
[440] Wang BK, Wang JH, Liu Q, Huang H, Chen M, Li KY, et al. Rose-bengal-conjugated gold nanorods for in vivo photodynamic and photothermal oral cancer therapies. Biomaterials 2014;35:1954–66.
[441] Redmond RW, Gamlin JN. A compilation of singlet oxygen yields from biologically relevant molecules. Photochem Photobiol 1999;70:391–475.
[442] Gandin E, Lion Y, Vandevorst A. Quantum yield of singlet oxygen production by xanthene derivatives. Photochem Photobiol 1983;37:271–8.
[443] Lin J, Wang SJ, Huang P, Wang Z, Chen SH, Niu G, et al. Photosensitizer-loaded gold vesicles with strong plasmonic coupling effect for imaging-guided photothermal/photodynamic therapy. ACS Nano 2013;7:5320–9.
[444] Wang SH, Riedinger A, Li HB, Fu CH, Liu HY, Li LL, et al. Plasmonic copper sulfide nanocrystals exhibiting near-infrared photothermal and photodynamic therapeutic effects. ACS Nano 2015;9:1788–800.
[445] Sahu A, Choi WI, Lee JH, Tae G. Graphene oxide mediated delivery of methylene blue for combined photodynamic and photothermal therapy. Biomaterials 2013;34:6239–48.
[446] Kim SB, Lee TH, Yoon I, Shim YK, Lee WK. Gold nanorod-photosensitizer complex obtained by layer-by-layer method for photodynamic/photothermal therapy in vitro. Chem-Asian J 2015;10:563–7.
[447] Jang B, Park JY, Tung CH, Kim IH, Choi Y. Gold nanorod-photosensitizer complex for near-infrared fluorescence imaging and photodynamic/photothermal therapy in vivo. ACS Nano 2011;5:1086–94.
[448] Zhao TT, Shen XQ, Li L, Guan ZP, Gao NY, Yuan PY, et al. Gold nanorods as dual photo-sensitizing and imaging agents for two-photon photodynamic therapy. Nanoscale 2012;4:7712–9.
[449] Huang X, El-Sayed IH, Qian W, El-Sayed MA. Cancer cell imaging and photothermal therapy in the near-infrared region by using gold nanorods. J Am Chem Soc 2006;128:2115–20.
[450] Velusamy M, Shen JY, Lin JT, Lin YC, Hsieh CC, Lai CH, et al. A new series of quadrupolar type two-photon absorption chromophores bearing 11,12-dibutoxydibenzo[a,c]-phenazine bridged amines; their applications in two-photon fluorescence imaging and two-photon photodynamic therapy. Adv Func Mater 2009;19:2388–97.
[451] He F, Ren XS, Shen XQ, Xu QH. Water-soluble conjugated polymers for amplification of one- and two-photon properties of photosensitizers. Macromolecules 2011;44:5373–80.
[452] Wang J, Zhang ZH, Zha S, Zhu YY, Wu PY, Ehrenberg B, et al. Carbon nanodots featuring efficient FRET for two-photon photodynamic cancer therapy with a low fs laser power density. Biomaterials 2014;35:9372–81.
[453] Fowley C, Nomikou N, McHale AP, McCarron PA, McCaughan B, Callan JF. Water soluble quantum dots as hydrophilic carriers and two-photon excited energy donors in photodynamic therapy. J Mater Chem 2012;22:6456–62.
[454] Lemon CM, Karnas E, Bawendi MG, Nocera DG. Two-photon oxygen sensing with quantum dot-porphyrin conjugates. Inorg Chem 2013;52:10394–406.
[455] Liu K, Liu XM, Zeng QH, Zhang YL, Tu LP, Liu T, et al. Covalently assembled NIR nanoplatform for simultaneous fluorescence imaging and photodynamic therapy of cancer cells. ACS Nano 2012;6:4054–62.
[456] Arguinzoniz AG, Ruggiero E, Habtemariam A, Hernandez-Gil J, Salassa L, Mareque-Rivas JC. Light harvesting and photoemission by nanoparticles for photodynamic therapy. Part Part Syst Char 2014;31:46–75.
[457] Kalluru P, Vankayala R, Chiang CS, Hwang KC. Photosensitization of singlet oxygen and in vivo photodynamic therapeutic effects mediated by PEGylated $W_{18}O_{49}$ nanowires. Angew Chem Int Ed Engl 2013;52:12332–6.
[458] Juzenas P, Chen W, Sun YP, Coelho MAN, Generalov R, Generalova N, et al. Quantum dots and nanoparticles for photodynamic and radiation therapies of cancer. Adv Drug Deliv Rev 2008;60:1600–14.
[459] Chu MQ, Pan XJ, Zhang D, Wu Q, Peng JL, Hai WX. The therapeutic efficacy of CdTe and CdSe quantum dots for photothermal cancer therapy. Biomaterials 2012;33:7071–83.
[460] Fan YY, Liu HL, Han RC, Huang L, Shi H, Sha YL, et al. Extremely high brightness from polymer-encapsulated quantum dots for two-photon cellular and deep-tissue imaging. Sci Rep-Uk 2015;5.
[461] Zhang W, Guo ZY, Huang DQ, Liu ZM, Guo X, Zhong HQ. Synergistic effect of chemo-photothermal therapy using PEGylated graphene oxide. Biomaterials 2011;32:8555–61.
[462] Hu SH, Chen YW, Hung WT, Chen IW, Chen SY. Quantum-dot-tagged reduced graphene oxide nanocomposites for bright fluorescence bioimaging and photothermal therapy monitored in situ. Adv Mater 2012;24:1748–54.
[463] Ge JC, Lan MH, Zhou BJ, Liu WM, Guo L, Wang H, et al. A graphene quantum dot photodynamic therapy agent with high singlet oxygen generation. Nat Commun 2014;5.
[464] Gong H, Dong ZL, Liu YM, Yin SN, Cheng L, Xi WY, et al. Engineering of multifunctional nano-micelles for combined photothermal and photodynamic therapy under the guidance of multimodal imaging. Adv Func Mater 2014;24:6492–502.
[465] E. Anklam et al. Impact of engineered nanomaterials on health: considerations for benefit-risk assessment. Publications Office of the European Union; 2011.

[466] Fadeel B, Garcia-Bennett AE. Better safe than sorry: understanding the toxicological properties of inorganic nanoparticles manufactured for biomedical applications. Adv Drug Deliv Rev 2010;62:362–74.

[467] Hischier R, Walser T. Life cycle assessment of engineered nanomaterials: state of the art and strategies to overcome existing gaps. Sci Total Environ 2012;425:271–82.

[468] Petersen EJ, Diamond SA, Kennedy AJ, Goss GG, Ho K, Lead J, et al. Adapting OECD aquatic toxicity tests for use with manufactured nanomaterials: key issues and consensus recommendations. Environ Sci Technol 2015;49:9532–47.

[469] Lai JCK, Lai MB, Jandhyam S, Dukhande VV, Bhushan A, Daniels CK, et al. Exposure to titanium dioxide and other metallic oxide nanoparticles induces cytotoxicity on human neural cells and fibroblasts. Int J Nanomed 2008;3:533–45.

[470] Gurr JR, Wang ASS, Chen CH, Jan KY. Ultrafine titanium dioxide particles in the absence of photoactivation can induce oxidative damage to human bronchial epithelial cells. Toxicology 2005;213:66–73.

[471] Kim IS, Baek M, Choi SJ. Comparative cytotoxicity of Al_2O_3, CeO_2, TiO_2 and ZnO nanoparticles to human lung cells. J Nanosci Nanotechnol 2010;10:3453–8.

[472] Bahadar H, Maqbool F, Niaz K, Abdollahi M. Toxicity of nanoparticles and an overview of current experimental models. Iran Biomed J 2016;20:1–11.

[473] Qin H, Zhu C, An ZQ, Jiang Y, Zhao YC, Wang JX, et al. Silver nanoparticles promote osteogenic differentiation of human urine-derived stem cells at noncytotoxic concentrations. Int J Nanomed 2014;9:2469–78.

[474] Gonzales M, Mitsumori LM, Kushleika JV, Rosenfeld ME, Krishnan KM. Cytotoxicity of iron oxide nanoparticles made from the thermal decomposition of organometallics and aqueous phase transfer with Pluronic F127. Contrast Media Mol I 2010;5:286–93.

[475] Han XL, Gelein R, Corson N, Wade-Mercer P, Jiang JK, Biswas P, et al. Validation of an LDH assay for assessing nanoparticle toxicity. Toxicology 2011;287:99–104.

[476] Roesslein M, Hirsch C, Kaiser JP, Krug HF, Wick P. Comparability of in vitro tests for bioactive nanoparticles: a common assay to detect reactive oxygen species as an example. Int J Mol Sci 2013;14:24320–37.

[477] Lu X, Qian JC, Zhou HJ, Gan Q, Tang W, Lu JX, et al. In vitro cytotoxicity and induction of apoptosis by silica nanoparticles in human HepG2 hepatoma cells. Int J Nanomed 2011;6:1889–901.

[478] Elsabahy M, Wooley KL. Cytokines as biomarkers of nanoparticle immunotoxicity. Chem Soc Rev 2013;42:5552–76.

[479] Hillegass JM, Shukla A, Lathrop SA, MacPherson MB, Fukagawa NK, Mossman BT. Assessing nanotoxicity in cells in vitro. Wires Nanomed Nanobiol 2010;2:219–31.

[480] Kumaravel TS, Jha AN. Reliable Comet assay measurements for detecting DNA damage induced by ionising radiation and chemicals. Mutat Res – Genetic Toxicol Environ Mutag 2006;605:7–16.

[481] Chang FM, Reyna SM, Granados JC, Wei SJ, Innis-Whitehouse W, Maffi SK, et al. Inhibition of neddylation represses lipopolysaccharide-induced proinflammatory cytokine production in macrophage cells. J Biol Chem 2012;287:35756–67.

[482] Roy S, Bonfield T, Tartakoff AM. Non-apoptotic toxicity of *Pseudomonas aeruginosa* toward murine cells. PLoS ONE 2013;8.

[483] Handral HK, Tong HJ, Islam I, Sriram G, Rosa V, Cao T. Pluripotent stem cells: an in vitro model for nanotoxicity assessments. J Appl Toxicol 2016;36:1250–8.

[484] Moe B, Gabos S, Li XF. Real-time cell-microelectronic sensing of nanoparticle-induced cytotoxic effects. Anal Chim Acta 2013;789:83–90.

[485] Cattaneo AG, Gornati R, Chiriva-Internati M, Bernardini G. Ecotoxicology of nanomaterials: the role of invertebrate testing. ISJ-Invert Surviv J 2009;6:78–97.

[486] Parasuraman S. Toxicological screening. J Pharmacol Pharmacother 2011;2:74–9.

[487] Ivask A, ElBadawy A, Kaweeteerawat C, Boren D, Fischer H, Ji ZX, et al. Toxicity mechanisms in *Escherichia coli* vary for silver nanoparticles and differ from ionic silver. ACS Nano 2014;8:374–86.

[488] Walkey CD, Olsen JB, Song F, Liu R, Guo H, Olsen DW, et al. Protein corona fingerprinting predicts the cellular interaction of gold and silver nanoparticles. ACS Nano 2014;8:2439–55.

[489] Soenen SJ, Rivera-Gil P, Montenegro JM, Parak WJ, De Smedt SC, Braeckmans K. Cellular toxicity of inorganic nanoparticles: common aspects and guidelines for improved nanotoxicity evaluation. Nano Today 2011;6:446–65.

[490] Gnach A, Lipinski T, Bednarkiewicz A, Rybka J, Capobianco JA. Upconverting nanoparticles: assessing the toxicity. Chem Soc Rev 2015;44:1561–84.

[491] Ma NN, Ma C, Li CY, Wang T, Tang YJ, Wang HY, et al. Influence of nanoparticle shape, size, and surface functionalization on cellular uptake. J Nanosci Nanotechnol 2013;13:6485–98.

[492] Verma A, Stellacci F. Effect of surface properties on nanoparticle-cell interactions. Small 2010;6:12–21.

[493] Jain PK, Huang XH, El-Sayed IH, El-Sayed MA. Noble metals on the nanoscale: optical and photothermal properties and some applications in imaging, sensing, biology, and medicine. Acc Chem Res 2008;41:1578–86.

[494] Rivera Gil P, Huhn D, del Mercato LL, Sasse D, Parak WJ. Nanopharmacy: inorganic nanoscale devices as vectors and active compounds. Pharmacol Res 2010;62:115–25.

[495] Takahashi H, Niidome Y, Niidome T, Kaneko K, Kawasaki H, Yamada S. Modification of gold nanorods using phospatidylcholine to reduce cytotoxicity. Langmuir 2006;22:2–5.

[496] Xia YN, Li WY, Cobley CM, Chen JY, Xia XH, Zhang Q, et al. Gold nanocages: from synthesis to theranostic applications. Acc Chem Res 2011;44:914–24.

[497] Tang SH, Chen M, Zheng NF. Sub-10-nm Pd nanosheets with renal clearance for efficient near-infrared photothermal cancer therapy. Small 2014;10:3139–44.

[498] Cheng L, Liu JJ, Gu X, Gong H, Shi XZ, Liu T, et al. PEGylated WS2 nanosheets as a multifunctional theranostic agent for in vivo dual-modal CT/ photoacoustic imaging guided photothermal therapy. Adv Mater 2014;26:1886–93.

[499] Liu T, Wang C, Cui W, Gong H, Liang C, Shi XZ, et al. Combined photothermal and photodynamic therapy delivered by PEGylated MoS_2 nanosheets. Nanoscale 2014;6:11219–25.

[500] Wang SG, Li K, Chen Y, Chen HR, Ma M, Feng JW, et al. Biocompatible PEGylated MoS_2 nanosheets: controllable bottom-up synthesis and highly efficient photothermal regression of tumor. Biomaterials 2015;39:206–17.

[501] Li WH, Zamani R, Gil PR, Pelaz B, Ibanez M, Cadavid D, et al. CuTe nanocrystals: shape and size control, plasmonic properties, and use as SERS probes and photothermal agents. J Am Chem Soc 2013;135:7098–101.

[502] Chu MQ, Shao YX, Peng JL, Dai XY, Li HK, Wu QS, et al. Near-infrared laser light mediated cancer therapy by photothermal effect of Fe_3O_4 magnetic nanoparticles. Biomaterials 2013;34:4078–88.

[503] Chen M, Fang XL, Tang SH, Zheng NF. Polypyrrole nanoparticles for high-performance in vivo near-infrared photothermal cancer therapy. Chem Commun 2012;48:8934–6.

[504] Zha ZB, Yue XL, Ren QS, Dai ZF. Uniform polypyrrole nanoparticles with high photothermal conversion efficiency for photothermal ablation of cancer cells. Adv Mater 2013;25:777–82.

[505] Singh Z. Applications and toxicity of graphene family nanomaterials and their composites. Nanotechnol Sci Appl 2016;9:15–28.

[506] Zhou M, Zhang R, Huang MA, Lu W, Song SL, Melancon MP, et al. A chelator-free multifunctional [Cu-64]CuS nanoparticle platform for simultaneous micro-PET/CT imaging and photothermal ablation therapy. J Am Chem Soc 2010;132:15351–8.

[507] Bai J, Liu YW, Jiang XE. Multifunctional PEG-GO/CuS nanocomposites for near-infrared chemo-photothermal therapy. Biomaterials 2014;35:5805–13.

[508] Yang K, Yang GB, Chen L, Cheng L, Wang L, Ge CC, et al. FeS nanoplates as a multifunctional nano-theranostic for magnetic resonance imaging guided photothermal therapy. Biomaterials 2015;38:1–9.

[509] Yu Z, Ma X, Yu B, Pan Y, Liu Z. Synthesis and characterization of ZnS:Mn/ZnS core/shell nanoparticles for tumor targeting and imaging in vivo. J Biomater Appl 2013;28:232–40.

[510] Zhang YX, Li B, Cao YJ, Qin JB, Peng ZY, Xiao ZY, et al. Na$_{0.3}$WO$_3$ nanorods: a multifunctional agent for in vivo dual-model imaging and photothermal therapy of cancer cells. Dalton Trans 2015;44:2771–9.

[511] Ciofani G, Danti S, D'Alessandro D, Moscato S, Petrini M, Menciassi A. Barium titanate nanoparticles: highly cytocompatible dispersions in glycol-chitosan and doxorubicin complexes for cancer therapy. Nanoscale Res Lett 2010;5:1093–101.

[512] Mayer L, Slablab A, Dantelle G, Jacques V, Lepagnol-Bestel AM, Perruchas S, et al. Single KTP nanocrystals as second-harmonic generation biolabels in cortical neurons. Nanoscale 2013;5:8466–71.

[513] Wang J, Lu Y, Peng F, Zhong Y, Zhou Y, Jiang X, et al. Photostable water-dispersible NIR-emitting CdTe/CdS/ZnS core-shell-shell quantum dots for high-resolution tumor targeting. Biomaterials 2013;34:9509–18.

[514] Zhang XY, Yin JL, Kang C, Li J, Zhu Y, Li WX, et al. Biodistribution and toxicity of nanodiamonds in mice after intratracheal instillation. Toxicol Lett 2010;198:237–43.

[515] Mohan N, Chen CS, Hsieh HH, Wu YC, Chang HC. In vivo imaging and toxicity assessments of fluorescent nanodiamonds in *Caenorhabditis elegans*. Nano Lett 2010;10:3692–9.

[516] Chakravarty P, Marches R, Zimmerman NS, Swafford AD, Bajaj P, Musselman IH, et al. Thermal ablation of tumor cells with antibody-functionalized single-walled carbon nanotubes. Proc Natl Acad Sci USA 2008;105:8697–702.

[517] Yang ST, Fernando KA, Liu JH, Wang J, Sun HF, Liu Y, et al. Covalently PEGylated carbon nanotubes with stealth character in vivo. Small 2008;4:940–4.

[518] Jia G, Wang H, Yan L, Wang X, Pei R, Yan T, et al. Cytotoxicity of carbon nanomaterials: single-wall nanotube, multi-wall nanotube, and fullerene. Environ Sci Technol 2005;39:1378–83.

[519] Zhang XD, Wang HX, Wang H, Zhang Q, Xie JF, Tian YP, et al. Single-layered graphitic-C$_3$N$_4$ quantum dots for two-photon fluorescence imaging of cellular nucleus. Adv Mater 2014;26:4438.

[520] Havrdova M, Hola K, Skopalik J, Tomankova K, Martin PA, Cepe K, et al. Toxicity of carbon dots – effect of surface functionalization on the cell viability, reactive oxygen species generation and cell cycle. Carbon 2016;99:238–48.

[521] Park SY, Lee HU, Lee YC, Choi S, Cho DH, Kim HS, et al. Eco-friendly carbon-nanodot-based fluorescent paints for advanced photocatalytic systems. Sci Rep-Uk 2015;5.

[522] Ray SC, Saha A, Jana NR, Sarkar R. Fluorescent carbon nanoparticles: synthesis, characterization, and bioimaging application. J Phys Chem C 2009;113:18546–51.

[523] Robinson JT, Tabakman SM, Liang Y, Wang H, Casalongue HS, Vinh D, et al. Ultrasmall reduced graphene oxide with high near-infrared absorbance for photothermal therapy. J Am Chem Soc 2011;133:6825–31.

[524] Lalwani G, Sundararaj JL, Schaefer K, Button T, Sitharaman B. Synthesis, characterization, in vitro phantom imaging, and cytotoxicity of a novel graphene-based multimodal magnetic resonance imaging-X-ray computed tomography contrast agent. J Mater Chem B 2014;2:3519–30.

[525] Tu CQ, Ma XC, Pantazis P, Kauzlarich SM, Louie AY. Paramagnetic, silicon quantum dots for magnetic resonance and two-photon imaging of macrophages. J Am Chem Soc 2010;132:2016–23.

[526] Tran CLea. A scoping study to identify hazard data needs for addressing the risks presented by nanoparticles and nanotubes. Institute of Occupational Medicine; 2005.

[527] Rollins K. Nanobiotechnology regulation: a proposal for self-regulation with limited oversight. NANOTECHNOLOGY L. & BUS.; 2009.

[528] Rauscher H, Sokull-Kluttgen B, Stamm H. The European Commission's recommendation on the definition of nanomaterial makes an impact. Nanotoxicology 2013;7:1195–7.

[529] Sutariya VBP, Pathak Y. Biointeractions of nanomaterials. CRC Press; 2014.

[530] Frangioni JV. In vivo near-infrared fluorescence imaging. Curr Opin Chem Biol 2003;7:626–34.

[531] Licha K. Contrast agents II: contrast agents for optical imaging. Top Curr Chem 2002;222:29.

[532] Harry L, Osterman AS-G. Near-infrared fluorescence imaging: seeing beyond the visible with IRDye® infrared dyes. LI-COR® Biosciences White Paper 2007;17.

[533] Adams KE, Ke S, Kwon S, Liang F, Fan Z, Lu Y, et al. Comparison of visible and near-infrared wavelength-excitable fluorescent dyes for molecular imaging of cancer. J Biomed Opt 2007;12.

[534] Zagorovsky K, Chan WCW. BIOIMAGING Illuminating the deep. Nat Mater 2013;12:285–7.

[535] Veiseh O, Gunn JW, Zhang MQ. Design and fabrication of magnetic nanoparticles for targeted drug delivery and imaging. Adv Drug Deliv Rev 2010;62:284–304.

[536] Edirwickrema A, Saltzman WM. Nanotherapy for cancer: targeting and multifunctionality in the future of cancer therapies. ACS Biomater Sci Eng 2015;1:64–78.

[537] Xiao JL, Lu DH, Lee CH. Guiding the migration of adherent cells by using optical micropatterns. Appl Phys Lett 2013;102.

[538] Kim S, Jeong S. Effects of temperature-dependent optical properties on the fluence rate and temperature of biological tissue during low-level laser therapy. Laser Med Sci 2014;29:637–44.

[539] Perez-Hernandez M, del Pino P, Mitchell SG, Moros M, Stepien G, Pelaz B, et al. Dissecting the molecular mechanism of apoptosis during photothermal therapy using gold nanoprisms. ACS Nano 2015;9:52–61.

[540] Chow RT, Johnson MI, Lopes-Martins RAB, Bjordal JM. Efficacy of low-level laser therapy in the management of neck pain: a systematic review and meta-analysis of randomised placebo or active-treatment controlled trials. Lancet 2009;374:1897–908.

[541] Wang M, Abbineni G, Clevenger A, Mao CB, Xu SK. Upconversion nanoparticles: synthesis, surface modification and biological applications. Nanomed – Nanotechnol Biol Med 2011;7:710–29.

[542] Cheng L, Wang C, Liu Z. Upconversion nanoparticles and their composite nanostructures for biomedical imaging and cancer therapy. Nanoscale 2013;5:23–37.

[543] Chen GY, Agren H, Ohulchanskyy TY, Prasad PN. Light upconverting core-shell nanostructures: nanophotonic control for emerging applications. Chem Soc Rev 2015;44:1680–713.

[544] Cheng LA, Yang K, Zhang SA, Shao MW, Lee ST, Liu ZA. Highly-sensitive multiplexed in vivo imaging using PEGylated upconversion nanoparticles. Nano Res 2010;3:722–32.

[545] Gu JM, Yan YL, Zhao YS, Yao JN. Controlled synthesis of bulk polymer nanocomposites with tunable second order nonlinear optical properties. Adv Mater 2012;24:2249–53.

[546] Rodriguez EM, Kumar KU, Speghini A, Piccinelli F, Nodari L, Cannas C, et al. Non-linear niobate nanocrystals for two-photon imaging. Opt Mater 2011;33:258–66.

[547] Kulyk B, Sahraoui B, Krupka O, Kapustianyk V, Rudyk V, Berdowska E, et al. Linear and nonlinear optical properties of ZnO/PMMA nanocomposite films. J Appl Phys 2009;106.

[548] Wang SJ, Huang P, Nie LM, Xing RJ, Liu DB, Wang Z, et al. Single continuous wave laser induced photodynamic/plasmonic photothermal therapy using photosensitizer-functionalized gold nanostars. Adv Mater 2013;25:3055–61.

[549] Hashmi JT, Huang YY, Osmani BZ, Sharma SK, Naeser MA, Hamblin MR. Role of low-level laser therapy in neurorehabilitation. Pm&R 2010;2: S292–305.

[550] Lin F, Josephs SF, Alexandrescu DT, Ramos F, Bogin V, Gammill V, et al. Lasers, stem cells, and COPD. J Transl Med 2010;8.

[551] Avci P, Gupta A, Sadasivam M, Vecchio D, Pam Z, Pam N, et al. Low-level laser (light) therapy (LLLT) in skin: stimulating, healing, restoring. Semin Cutan Med Surg 2013;32:41–52.

[552] Farivar S, Malekshahabi T, Shiari R. Biological effects of low level laser therapy. J Las Med Sci 2014;5:58–62.

[553] Cheng L, Wang C, Feng L, Yang K, Liu Z. Functional nanomaterials for phototherapies of cancer. Chem Rev 2014;114:10869–939.

[554] Qiao XF, Zhou JC, Xiao JW, Wang YF, Sun LD, Yan CH. Triple-functional core-shell structured upconversion luminescent nanoparticles covalently grafted with photosensitizer for luminescent, magnetic resonance imaging and photodynamic therapy in vitro. Nanoscale 2012;4:4611–23.

[555] Chatterjee DK, Fong LS, Zhang Y. Nanoparticles in photodynamic therapy: an emerging paradigm. Adv Drug Deliv Rev 2008;60:1627–37.

[556] Huang P, Lin J, Wang S, Zhou Z, Li Z, Wang Z, et al. Photosensitizer-conjugated silica-coated gold nanoclusters for fluorescence imaging-guided photodynamic therapy. Biomaterials 2013;34:4643–54.

[557] Huang P, Xu C, Lin J, Wang C, Wang X, Zhang C, et al. Folic acid-conjugated graphene oxide loaded with photosensitizers for targeting photodynamic therapy. Theranostics 2011;1:240–50.

[558] Yu J, Hsu CH, Huang CC, Chang PY. Development of therapeutic Au-methylene blue nanoparticles for targeted photodynamic therapy of cervical cancer cells. ACS Appl Mater Interfaces 2015;7:432–41.

[559] Wainwright M. Phenothiazinium photosensitisers: V. Photobactericidal activities of chromophore-methylated phenothiazinium salts. Dyes Pigm 2007;73:7–12.

[560] Feng W, Han CM, Li FY. Upconversion-nanophosphor-based functional nanocomposites. Adv Mater 2013;25:5287–303.

[561] Bhawalkar JD, Kumar ND, Zhao CF, Prasad PN. Two-photon photodynamic therapy. J Clin Laser Med Surg 1997;15:201–4.

[562] Roy I, Ohulchanskyy TY, Pudavar HE, Bergey EJ, Oseroff AR, Morgan J, et al. Ceramic-based nanoparticles entrapping water-insoluble photosensitizing anticancer drugs: a novel drug-carrier system for photodynamic therapy. J Am Chem Soc 2003;125:7860–5.

[563] Cui SS, Yin DY, Chen YQ, Di YF, Chen HY, Ma YX, et al. In vivo targeted deep-tissue photodynamic therapy based on near-infrared light triggered upconversion nanoconstruct. ACS Nano 2013;7:676–88.